UC Santa Barbara

UC Santa Barbara Electronic Theses and Dissertations

Title

Aggregation, Breakup, and Size-Dependent Transport of Cohesive Particles in Wall-Bounded Turbulence and its Implications for Population Balance Models

Permalink

https://escholarship.org/uc/item/0006g9g2

ISBN

9798171612061

Author

Leonelli, Alexandre

Publication Date

2026-09-11

Peer reviewed|Thesis/dissertation

eScholarship.org Powered by the California Digital Library
University of California

University of California

Santa Barbara

Aggregation, Breakup, and Size-Dependent Transport of Cohesive Particles in Wall-Bounded Turbulence and its Implications for Population Balance Models

A dissertation submitted in partial satisfaction

of the requirements for the degree

Doctor of Philosophy

in

Mechanical Engineering

by

Alexandre Dillon Leonelli

Committee in charge:

Professor Eckart Meiburg, Chair
Professor Alban Sauret
Professor Paolo Luzzatto-Fegiz
Professor Emilie Dressaire
Professor Arturo Keller

September 2026

The Dissertation of Alexandre Dillon Leonelli is approved.

Professor Alban Sauret

Professor Paolo Luzzatto-Fegiz

Professor Emilie Dressaire

Professor Arturo Keller

Professor Eckart Meiburg, Committee Chair

August 2026

Aggregation, Breakup, and Size-Dependent Transport of Cohesive Particles in Wall-Bounded Turbulence and its Implications for Population Balance Models

Copyright © 2026

by

Alexandre Dillon Leonelli

To my colleagues, friends, and family;
those I know and those I am yet to meet.
Per sapientiam et amorem, Pax.

Acknowledgements

I want to thank Dr. Ronald Chan and Prof. Filippo Coletti for many insightful discussions and my participation in the 2024 Stanford Center for Turbulence Research Summer Program at which a large portion of the theoretical backbone of this work was initiated. I would also like to acknowledge financial support from the Geological Survey of Israel, the Army Corps of Engineers through grant No. W912HZ22C0037, and the Army Research Office through grant No. W911NF-23-2-0046. This work used Anvil at Purdue University RCAC through allocation MCH260012 and CTS150053 from the Advanced Cyberinfrastructure Coordination Ecosystem: Services & Support (ACCESS) program, which is supported by U.S. National Science Foundation grants #2138259, #2138286, #2138307, #2137603, and #2138296.

While reflecting on the past six years, I keep returning to the same sentiment: I am deeply privileged to have had this time to ponder questions that many are not afforded the luxury of asking. For this, and for the joy and wonder it has brought me, I owe an immeasurable debt to the colleagues, friends, and family I acknowledge here.

First, to my singular advisor, Eckart Meiburg, thank you. Under your mentorship I grew twice over: first as a researcher, sharpened by your insight, and second as a person, shaped by your kindness, diplomacy, and joy. I am grateful for an advisor who placed so much weight on that balance of humanity and rigor. Because of it, I am leaving Santa Barbara with memories of red rocks framed by an even redder car, and with an excitement, kindled by you, to keep questioning and researching the things we've started exploring together. I've spent over 1/5 of my life under your guidance, and I intend to keep seeking it out.

I am also beholden to my dissertation committee: Alban Sauret, Paolo Luzzatto-

Fegiz, Emilie Dressaire, and Arturo Keller. Each of you shaped not only this work but my sense of what a researcher can be, and I can only hope to carry forward your generosity as a mentor myself.

I am, of course, indebted to my parents, Nathalie and David Leonelli, and my brother, Némo, whose love has been a constant source of stability and refuge. The same is true of my parents- and sister-in-law, Carlos, Kaori, and Kaila (and soon-to-be brother-in-law, Aiden).

To my lab group, Zack, Polina, Maxime, Jasper, Paul, and Haggai, and to those who passed through in visiting roles, Beni, Daan, Lukas, Cansu, Mohsen, and more: thank you for listening to my ramblings. Each of you fed my love of this scientific journey in ways I don't think you realize.

To Doug Jerolmack, Nathalie Vriend, and Vashan Wright, organizers of the 2026 KITP Soft Earth Geophysics program, and to everyone who took part: thank you for building a space where early-career researchers didn't just feel welcome, but needed. The vulnerability and empathy you brought defined that program, and it's ours now to carry forward.

I also owe thanks to Tim Robinson, coach of the UCSB fencing team. After fencing for UCSD as an undergraduate, I was thrilled to find I could keep going at UCSB — I knew I'd enjoy the bouting, but I didn't expect to make my best fencing memories here. And to Ian, Chris, and Yousuff, thank you, though I hope to never again lose my voice for an entire week.

Marcel, Anne-Marie, and Leia, thank you for being a second family. Your hospitality, generosity, and wisdom will live on in any home I go on to build.

I also have to acknowledge Sreeram and Ram, my scientific partners in crime through all of this. You've pushed and inspired me more than you know, and I can't wait to see you both next.

And there's a whole crowd of friends new and old that I've picked up along the way, through collaboration, running, cycling, who keep me grounded more than they know: Ravi, Nick, Miles, Carlos, Alice, Roie, Fabian, Bernhard, Alex M., Ali, Sudarshan, Vironica, Madison, Charlie, Shantal, Connor, Luis, Deok-Hoon, and Virgile. To anyone I missed, thank you too.

I also want to recognize the teachers I have had throughout my education who nurtured my curiosity and thrust me forward into the sciences with excitement and wonder: my elementary school science teacher, Nancy Swanberg; my high school physics and math teachers, Andrew Corman and James Farrar; and my lower-division undergraduate physics professor, Aneesh Manohar.

Finally, my wife, Miya, whose own brilliance is carrying her toward a PhD of her own. I can't fully express how integral you've been to this thesis, you are in every keystroke, every figure. I am forever proud to be your husband, and endlessly grateful for your love and support. Thank you.

Curriculum Vitæ

Alexandre Dillon Leonelli

Education

2026	Ph.D. in Mechanical Engineering (Expected), University of California, Santa Barbara.
2020	B.S. in Physics, University of California, San Diego.

Publications

Leonelli, A. D., Widmer, L. & Meiburg, E. (2026). "Aggregation, breakup, and size-dependent transport in a turbulent channel flow with cohesive particles," under review at J. Fluid Mech.,

Khodabakhshi, A., Konidena, S., Tapia, F. **Leonelli, A. D.** & Vowinckel, B. (2026). "Transition between the viscous and the inertial regime in sheared dense suspensions: the effect of wall boundaries," Acta Mech.

Sharma, R. S., **Leonelli, A. D.**, Zhao, K., Meiburg, E. & Sauret, A. (2026). "Gravity-Driven Flux of Particles through Apertures," Phys. Rev. Lett. 16(6), 068204.

Leonelli, A. D. & Meiburg, E. (2025). "On the effects of anisotropy on the flocculation of cohesive particles in turbulence," Acta Mech. 237, 1699–1713.

Rahimi-Larki M., **Leonelli, A. D.**, Behrad, E., Vowinckel, B., Vollmann, S., Harmuth, H. & Meiburg, E. (2025). "Flow-induced erosion process modeling: A review of influencing parameters and CFD-DEM methods," Powder Technol., 468, 0032-5910.

Proceedings and Reports

Leonelli, A. D. & Meiburg, E. (2026). "Turbulent Channel Flow with Cohesive Particles," in Proceedings of the 14th International Symposium on Turbulence and Shear Flow Phenomena. Heidelberg, Germany.

Leonelli A. D., Meiburg, E., Balachandar, S., Wang, J. & Johnson, P. (2024). "Gravity currents over mobile sediment beds," in Center for Turbulence Research: Proceedings of the Summer Program, pages 485-494. Stanford University.

Leonelli, A. D., Meiburg, E. & Bravo, L. (2022). "Direct Numerical Simulation of Particle Transport and Dispersion in Wall-Bounded Turbulent Flows," US Army Combat Capabilities Development Command, Army Research Laboratory. Defense Technical Information Center (DTIC). ARL-TR-9394.

Abstract

Aggregation, Breakup, and Size-Dependent Transport of Cohesive Particles in Wall-Bounded Turbulence and its Implications for Population Balance Models

by

Alexandre Dillon Leonelli

Cohesive granular materials suspended in turbulent flows undergo a complex process of aggregation, breakup, and restructuring, collectively known as *flocculation*, wherein turbulence plays a dual role: facilitating aggregate growth by enhancing collision rates, while simultaneously promoting breakup through increased hydrodynamic stresses [1]. The result of this competition is a dynamic population of aggregates whose size distribution directly controls particle transport and dispersion, making flocculation a central process across a wide range of environmental and engineering systems. Accurate prediction and evolution of the size distribution is therefore paramount.

The population balance equation (PBE) [2, 3] evolves the size distribution on the basis of probabilistic, rate-describing kernels that account for aggregation and breakup. These kernels are heavily parameterized and are often empirically calibrated or agnostic to local flow conditions. Improving the physical basis of these kernels by identifying and characterizing the mechanisms that govern aggregation and breakup in turbulent flows is therefore essential to developing predictive PBE models.

To this end, this dissertation presents a fundamental study on the transport of cohesive granular materials in wall-bounded turbulence, where the highly anisotropic and inhomogeneous turbulent flow leads to a rich array of spatially organized mechanisms. Six particle-resolved direct numerical simulations of turbulent channel flows laden with finite-sized cohesive particles at successively increasing cohesive strength are performed

and characterized. Aggregation and breakup are shown to be highly dependent on the wall-normal direction and local turbulent shear rate. The formation of increasingly large aggregates is shown to modulate the underlying turbulence and wall shear stress: smaller particles, which normally reside near the walls, are captured by larger aggregates, resulting in a drag reduction relative to the noncohesive case.

Finally, a novel PBE-based framework is used to analyze aggregate dynamics and trajectories through the joint space of size and wall-normal distance. Within this space, we identify regions of net aggregate production and removal. For example, due to breakup, smaller aggregates are preferentially created near the wall, where shear rates and turbulence intensities are elevated. This results in a net production of small aggregates near the wall that is balanced by advective transport. Expanding this to all sizes reveals a newly identified circulation: larger aggregates are overproduced in the channel center, migrate toward a wall, and break. The resulting smaller aggregates are carried back to the channel center, where they once again grow, and the cycle repeats.

Nomenclature

Acronyms and abbreviations

CFL	Courant–Friedrichs–Lewy
DEM	Discrete element method
DLVO	Derjaguin–Landau–Verwey–Overbeek
EL	Euler-Lagrange
HIT	Homogeneous isotropic turbulence
IB	Immersed boundary
IBM	Immersed boundary method
LES	Large-eddy simulation
LPT	Lagrangian particle tracking
MAC	Marker-and-cell
MRGE	Maxey–Riley–Gatignol equation
PARTIES	PARTicle laden flows via immersed boundarIES
PBE	Population balance equation
PR-DNS	Particle-resolved direct numerical simulation
RANS	Reynolds-averaged Navier-Stokes
RK	Runge-Kutta
vdW	van der Waals

Dimensionless numbers

$\mathcal{C}$	CFL number
Co	Cohesive number
$\hat{k}$	Dimensionless normal contact stiffness
Re	Reynolds number, distinct in section 2.3 and chapter 3 onward
Re_τ	Friction Reynolds number
$Re_{p,e}$	Effective particle Reynolds number
$Re_{p,i}$	Particle Reynolds number for particle i (a posteriori, from slip velocity)
ρ_s	Particle-to-fluid density ratio
St	Stokes number, distinct in section 2.3 and chapter 3 onward

St_{crit}	Critical collision Stokes number
St_{in}	Collision Stokes number
Θ	Ratio of collision to flow timescales

Notation

$\boldsymbol{\nabla}$	Gradient operator
$\|\cdot\|$	L2 norm
$\cdot^T$	Transpose
$\cdot^+$	Quantity made dimensionless by wall units (δ_ν, u_τ)
$\delta(\cdot)$	Dirac delta function
$\widetilde{\cdot}$	Plane-average operator
$\widetilde{\widetilde{\cdot}}$	Volume-average operator
$\overline{\cdot}$	Plane-and-time-average operator
$\overline{\overline{\cdot}}$	Volume-and-time-average operator
$\langle\cdot\rangle$	Time-average operator
$\mathring{\cdot}$	Ring accent denoting an estimated, rather than exact, mean quantity
$\mathrm{Var}(\cdot)$	Variance operator

Greek symbols

$\boldsymbol{\zeta}_{t,ij}$	Tangential displacement during contact between particles i and j
$\boldsymbol{\tau}$	Hydrodynamic stress tensor
$\boldsymbol{\omega}_i^P$	Angular velocity vector of particle i ($\omega_{x,i}^P, \omega_{y,i}^P, \omega_{z,i}^P$)
α	Free shape parameter of the beta distribution
α_c	Collision rate
β	Aggregation (coalescence) frequency
Γ_i	Surface of particle i
$\dot{\gamma}$	Shear rate
Δt	Time step
Δt_{CFL}	CFL-limited time step
Δt_f	Fluid solver time step
$\Delta_{t_{IO}}$	Snapshot output interval during the equilibrium period

$\Delta_{t_{IO,sub}}$	Snapshot output interval during the subsampling period
Δt_{k_n}	Collision-limited time step
Δt_p	Particle sub-stepping time step
Δx	Isotropic grid spacing
Δy	Wall-normal bin spacing
δ_ν	Wall unit (viscous length scale)
$\delta_{p,i}$	Boundary layer thickness of particle i
ϵ	Minimum particle overlap multiplier
ε	Turbulent dissipation rate
$\dot{\varepsilon}_\parallel$	Rate of strain along an aggregate's long axis
ζ_0	Scale of particle surface asperities
ζ_{ij}	Surface distance between particle i and j
ζ_{min}	Lubrication model regularization constant
$\zeta_j^A(t)$	Minimum particle–wall gap among the constituent particles of aggregate j
$\zeta_{min,j}$	Closest wall approach of aggregate j prior to its death
η	Kolmogorov length scale
η_e	Effective suspension shear viscosity
$\eta_{e,n}$	Effective suspension normal viscosity
η_f	Fluid dynamic viscosity
$\theta_{i,j}$	Alignment angle between aggregate j and coordinate axis i
θ_s	Polar angle in spherical coordinates
λ	Cohesive force length scale
μ_k	Kinetic friction coefficient
μ_s	Static friction coefficient
μ_t	Friction coefficient
ν	Kinematic viscosity
ξ_f	Fluid indicator function
ρ_f	Fluid density
$\rho_{p,i}$	Density of particle i (monodisperse $\rho_{p,i} = \rho_p$)
σ_p	Particle stress tensor

$\sigma_{p,xy}$	xy-component of the particle stress tensor
τ	Total shear stress
τ_ν	Viscous stress
τ_P	Particle-induced stress
τ_T	Turbulent (Reynolds) stress
τ_{T_f}	Fluid contribution to the combined-phase Reynolds shear stress
τ_{T_P}	Particle contribution to the combined-phase Reynolds shear stress
τ_w	Wall shear stress
ϕ	Local solid volume fraction
ϕ_0	Bulk volume fraction, distinct in section 2.3 and chapter 3 onward
ϕ_s	Azimuthal angle in spherical coordinates
$\phi_{startup}$	Startup-phase volume fraction
Φ_b	Breakup fraction
χ	Fractal prefactor
Ψ	Volume ratio of two coalescing aggregates, $D_1^3/(D_1^3 + D_2^3)$
ω_x^A	Angular velocity of an aggregate about the streamwise axis
ω_y^A	Angular velocity of an aggregate about the wall-normal axis
ω_z^A	Angular velocity of an aggregate about the spanwise axis
Ω	Computational domain

Roman symbols

$\mathbf{E}$	Diagonal of velocity gradient tensor
$\hat{\boldsymbol{e}}_i$	Domain coordinate basis vector, $i \in \{x, y, z\}$
$\boldsymbol{e}_{ij}^P$	Unit vector directed from the center of particle i to j
$\boldsymbol{e}_{iw}^P$	Unit vector directed from the center of particle i to the nearest point on wall w
$\boldsymbol{e}_j^A$	Unit principal eigenvector of the gyration tensor of aggregate j (orientation vector)
$\boldsymbol{e}_{t,ij}$	Direction of sliding contact force between particles i and j
$\boldsymbol{F}_{c,i}$	Net contact force acting on particle i
$\boldsymbol{F}_{coh,ij}$	Cohesive force acting on particle i by particle j
$\boldsymbol{F}_{\ell,ij}$	Lubrication force acting on particle i by particle j; subscript j is replaced by w

	to denote the analogous particle-wall force
$\boldsymbol{F}_{n,ij}$	Normal collision force on particle i by particle j; subscript j is replaced by w to denote the analogous particle-wall force
$\boldsymbol{F}_{s,ij}$	Tangential force during sliding contact
$\boldsymbol{F}_{t,ij}$	Tangential collision force on particle i by particle j; subscript j is replaced by w to denote the analogous particle-wall force
$\boldsymbol{f}_{IBM}$	Immersed boundary volume force
$\mathcal{G}_j$	Gyration tensor of aggregate j
$\boldsymbol{g}_{ij}$	Relative normal velocity between particles i and j
$\boldsymbol{g}_{t,ij}$	Tangential component of relative surface velocities of particles i and j
$\mathbf{I}$	Identity matrix
$\boldsymbol{n}_i^P$	Unit surface normal vector to particle i
$\boldsymbol{r}_i^P$	Displacement vector relative to the center of particle i
$\boldsymbol{r}_i^{PA}$	Position of particle i relative to the center of mass of its host aggregate
$\boldsymbol{r}_{iw}$	The displacement vector from the center of particle i to the nearest point on wall w
$\boldsymbol{T}_{c,i}$	Net contact torque acting on particle i
$\boldsymbol{u}$	Fluid velocity vector (u, v, w)
$\boldsymbol{u}_i^F$	Mean fluid velocity within a shell surrounding particle i
$\boldsymbol{u}_i^P$	Velocity vector of particle i (u_i^P, v_i^P, w_i^P)
$\Delta\boldsymbol{u}_i^{PF}$	Slip velocity between particle i and the fluid
$\boldsymbol{x}_i^P$	Center of particle i (x_i^P, y_i^P, w_i^P)
$\boldsymbol{x}_{iw}$	The nearest point on wall w to particle i
$\boldsymbol{x}_j^A$	Center of mass of aggregate j
$\mathcal{A}_j$	Primary particle set comprising aggregate j
$\mathcal{A}_n(t)$	Primary particle set belonging to aggregates of size n
$\mathcal{C}_j$	Set of child aggregates of j
$\mathcal{P}_k$	Set of parent aggregates of k
$\mathcal{V}_i(y_j, t)$	Volume of particle i within wall-normal bin j
A	Power-law fit prefactor
A_+	Aggregation source term

A_-	Aggregation sink term
A_H	Hamaker constant
$B(\alpha, \alpha)$	Beta function
B_+	Breakup source term
B_-	Breakup sink term
b	Integral-scale aggregate growth rate
b_n	Normal collision model damping coefficient
b_t	Tangential collision model damping coefficient
c_{95}	Prefactor for a 95% confidence interval
$C(s)$	Global autocorrelation function of the aggregate number density fluctuations
C_1	Prefactor in the log-log regression of $K_1(y)$ against $G(y)$
C_2	Prefactor in the log-log regression of $K_2(y)$ against $G(y)$
D	Diameter of an sphere with equivalent volume to the solid volume of an aggregate
D_1	Diameter of the first of two coalescing aggregates
D_2	Diameter of the second of two coalescing aggregates
D_c	Child aggregate diameter
$D_{c,L}$	Diameter of the larger fragment in a breakup event
D_e	Placeholder symbol for a characteristic aggregate diameter
D_F	Feret diameter
D_g	Diameter of gyration
D_i	Effective diameter of aggregate i
D_p	Parent aggregate diameter
$\hat{D}$	Dimensionless aggregate size, D/d
d_{50}	Mean particle diameter (monodisperse $d_{50} = d$)
d_i	Diameter of particle i (monodisperse $d_i = d$)
d_{ij}^*	Effective diameter during collision
e	Restitution coefficient
F_y	Aggregate yield strength
f	Aggregate number density

G	Turbulent (Kolmogorov) shear rate
g_b	Breakup rate
H	Numerical rheometer effective gap width
h	Channel half-height
$I_{p,i}$	Moment of inertia of particle i
k_A	Winterwerp aggregation fitting parameter
k_B	Winterwerp breakup fitting parameter
k_n	Normal collision model stiffness coefficient
$k_{n,crit}$	Critical normal collision model stiffness coefficient
$k_{n,grav}$	Normal collision model stiffness coefficient required to support particle dry weight
k_p	Particle-phase turbulent kinetic energy
k_t	Tangential collision model stiffness coefficient
K_1	Shear-rate-scaled Winterwerp aggregation rate constant
K_2	Shear-rate-scaled Winterwerp breakup rate constant
L_x	Domain size in streamwise direction, distinct in section 2.3 and chapter 3 onward
L_y	Domain size in spanwise direction, distinct in section 2.3 and chapter 3 onward
L_z	Domain size in wall-normal direction, distinct in section 2.3 and chapter 3 onward
ℓ_x	Domain half-length in the streamwise direction
m_i^A	Mass of aggregate i
$m_{eff,ij}$	Effective mass of colliding particles i and j ($m_{eff,iw} = m_i$)
$m_{p,i}$	Mass of particle i
N	Number of particles
N_a	Total number of aggregates
N_{agg}	Number of aggregation events
N_{break}	Number of breakup events
N_{eff}	Effective number of independent samples
N_{eq}	Equilibrium number of aggregates
N_x	Number of grid points in the streamwise direction
N_y	Number of grid points in the wall-normal direction

N_z	Number of grid points in the spanwise direction
n	Number of primary particles in an aggregate
n_{bin}	Number of wall-normal bins
n_c	Number of PBE size classes
n_f	Fractal dimension
n_j	Number of particles in aggregate j
p	Dynamic pressure
p_1	Empirical shear-rate exponent for $K_1(y)$
p_2	Empirical shear-rate exponent for $K_2(y)$
p_W	Winterwerp breakup strength exponent
q_a	Aggregation efficiency
q_b	Fragment size distribution
q_W	Winterwerp breakup shear-rate exponent
Q	Combined net population balance equation source term, $\sum_i S_i$
R	Shell radius used in the slip-velocity integral
R_{uu}	Streamwise autocorrelation function of streamwise velocity fluctuations
R_{vv}	Streamwise autocorrelation function of wall-normal velocity fluctuations
R_{ww}	Streamwise autocorrelation function of spanwise velocity fluctuations
r_i	Radius of particle i
$r_{\parallel,ij}$	Axial position of particle i projected onto the orientation axis of aggregate j
S_i	Generic population balance equation source or sink term
SE	Standard error
s	Time lag e.g. in global autocorrelation function
T	General averaging time interval
T_a	Net transport due to aggregation
T_b	Net transport due to breakup
T_{eq}	Sampling period
T_{sub}	Sub-sampling period
t	Time
t_*	Normal collision model time constant

t_c	Time of collision
$t_{d,j}$	Time of death of aggregate j
t_{end}	Final simulation snapshot time
t_{eq}	Aggregate population equilibration time
t_f	Characteristic flow timescale
t_0	First zero-crossing time of the autocorrelation function
t_{int}	Integral correlation time
t_{sub}	Start time of the subsampling period
t_{win}	Lookback time window for identifying an aggregate's closest wall approach
U	Bulk velocity
u_c'	Streamwise velocity fluctuation of the combined phase
u_{in}	Incoming relative speed before collision
$u_{in,crit}$	Critical incoming collision speed
u_{out}	Outgoing relative speed after collision
u_p	Plane-averaged particle-phase streamwise velocity
$u_{\parallel,ij}$	Axial velocity of particle i projected onto the orientation axis of aggregate j
u_τ	Friction velocity
u_w	Numerical rheometer plate speed
$V(n, y_j, t)$	Total particle volume in wall-normal bin j contributed by aggregates of size n
V_p	Volume of a primary particle
$V_{p,i}$	Volume of particle i
V_y	Volume of a wall-normal bin
v_c'	Wall-normal velocity fluctuation of the combined phase
v_D	Continuous growth or shrinkage rate of aggregates in size space
x	Streamwise coordinate
y	Wall-normal coordinate
y_j	Wall-normal bin center
$y_{l,i}$	Lower wall-normal bin bound relative to particle i's center
$y_{u,i}$	Upper wall-normal bin bound relative to particle i's center
z	Spanwise coordinate

List of Tables

3.1 Summary of simulation parameters, timing, sampling periods, and friction Reynolds number. The time for the aggregate population to equilibrate is reported as, t_{eq}. T_{sub} is the subs-sampling period within which aggregation and breakup statistics are reported in chapters 6 and 7, and falls within the broader sampling period T_{eq}, which is defined along with t_{eq} in chapter 5. The time periods are made dimensionless by the large eddy turnover time u_τ/h. For the single phase case, SP, time used to compute statistics after discarding transients, as described in section 3.3 is reported as T_{eq}. Finally, the friction Reynolds number, Re_τ, computed over T_{eq} is reported. Case C2 was not sub-sampled and therefore does not appear in section 6.3 and chapter 7. 28

5.1 Power law fits of the variation of the model parameters K_1 and K_2 from the flocculation model, equation 5.8 with the cohesive number Co. The K_1 and K_2 for each characteristic diameter and the above fits are displayed in figure 5.4. 59

B.1 Aggregation and breakup event detections. Missed events are either non-binary or complex as defined in section B. 108

C.1 Timing statistics results and error prefactors. 112

List of Figures

2.1 Minimum surface distance between two particles, $\min \zeta_{ij}/d_{50}$, for a series of independent simulations of a sheared suspension at (a) CFL number $\mathcal{C} = 0.8$ across a range of Stokes numbers, St, and (b) $St = 0.5$ across a range of CFL numbers, $\mathcal{C}$. 23

3.1 Schematic of the simulation domain. Slices from case $Co = 1$ are shown sequentially along the channel for increasing times, with aggregates colored by the number of constituent particles. 26

3.2 (a) Stress balance for the single-phase precursor flow, showing profiles of the viscous (τ_ν), turbulent (τ_T), and total (τ) stresses in inner units, over the wall-normal coordinate y, made dimensionless with the half channel height h. (b) Streamwise autocorrelation functions of the streamwise (R_{uu}), wall-normal (R_{vv}), and spanwise (R_{ww}) velocity fluctuations, where ℓ_x/h denotes the streamwise separation relative to the half channel height h. The horizontal gray line marks zero. 33

3.3 Comparison of (a) the mean streamwise fluid velocity, $\overline{u}^+$ and (b) velocity fluctuations, $\overline{u'u'}^+$; -·-·-, $\overline{v'v'}^+$; ——, and $\overline{w'w'}^+$; - - -, from the single-phase (SP) and non-cohesive ($Co = 0$) cases from this study, and the channel flow DNS of $Re_\tau = 182.088$ by Lee & Moser [4] (LM2015). 34

4.1 Schematic depicting the roles of the aggregation and breakup source and sink terms in equation (4.8). The horizontal axis shows the space of aggregate sizes with an arbitrary class n partitioned by two gray horizontal lines on either side. Arrows representing aggregation and breakup events point from parent to child aggregate(s) and enter/exit the size n partition. 40

4.2 (a) A local segment of the family tree from case $Co = 0.48$, centered on a single aggregate of interest, here assigned aggregate ID 0. The vertical axis shows aggregate ID; the horizontal axis reports elapsed simulation time. An aggregate's time of birth is marked by a box inscribed with the number of primary particles it contains, and a black horizontal line spans its lifetime, terminating in a black dot marking its time of death. Vertical lines connect the time of death of a parent aggregate to the time of birth of its child or children. A red vertical line denotes an aggregation event, connecting the deaths of two parent aggregates to the birth of the resulting aggregation product. A blue vertical line denotes a breakup event, originating from the single black dot marking the parent aggregate's death and connecting to two boxes marking the birth of the resulting child aggregates, each inscribed with its size. Panels (b–e) show snapshots of aggregate 0 and its children, aggregates 1 and 2, corresponding to the segment of the family tree in panel (a). Before breakup (panels (b) and (c)), primary particles are colored gray; after breakup, aggregate 1 is colored orange and aggregate 2 is colored blue. Trailing lines show the preceding $0.2h/U$ time units of each particle's trajectory. Panels (b–e) are centered on the center of mass of the aggregate or aggregate pair; since aggregates travel across the periodic boundary in the streamwise direction, the x-position shown may decrease between sequential panels. 48

5.1 (a) Total number of aggregates N_a over time t for each Co. The exponential fit, equation (5.2), is shown as dashed lines. The light gray dash-dotted line shows the total number of primary particles $N = 3841$. The time to reach equilibrium t_{eq} is marked by diamonds and is additionally annotated for $Co = 0.48$ by a vertical dash-dotted line with the same color. N_{eq} is similarly annotated by a horizontal dashed line. (b) Number of aggregates of sizes $n = \{1, 2, 3\}$ and $n > 3$ over time for case $Co = 0.48$. The time periods displayed in both figures do not display the full runtime, which is reported in table 3.1. Furthermore, time t is made dimensionless with the mean streamwise velocity, U, and half channel height, h, in both panels. 54

5.2 The mean Feret diameter, $\langle D_F \rangle_n$, for each aggregate population of n primary particles, plotted against n. The power law, equation (5.7), is fit to all data with $Co > 0$, yielding $\chi = 0.4$ and $n_f = 2.14$, shown as a black line. 57

5.3 Evolution of mean aggregate size over time as evaluated by the (a) Feret diameter, $\widetilde{\widetilde{D_F}}/d$, (b) diameter of gyration, $\widetilde{\widetilde{D_g}}/d$, (c) diameter of a sphere of equivalent volume to the aggregate $\widetilde{\widetilde{D}}/d$. The fits from equation (5.8) are shown as dashed lines with fitting parameters reported in figure 5.4. . 58

5.4 Power law dependencies of the fitting parameters K_1 and K_2 from the flocculation model, equation 5.8. Column titles indicate which spatial scale is used to define the aggregate diameter with D_F the Feret diameter, D_g the diameter of gyration, and D the sphere equivalent diameter. A solid line through the data points displays the result of a linear regression, with the slope m annotated. Detailed fit parameters are reported in table 5.1. 60

5.5 (a) Time evolution of the mean Feret diameter, $\widetilde{D_F/d}$, in 8 bins ($n_{bin} = 32$ averaged over the symmetry plane) in the wall-normal direction for case $Co = 0.48$. The wall-normal position of each bin is denoted by its color with the corresponding color bar ranging from the wall at $y/h = 0$ to the channel center at $y/h = 1$. The best fits of equation (5.8) for each bin are shown as dashed lines. (b) The fitted $K_1(y)$ (circles) and $K_2(y)$ (diamonds) plotted over the half channel height. The markers are filled to match (a) while the bins are demarcated by light gray vertical lines. . . . 61

5.6 Wall-normal profile of the Kolmogorov shear rate $G = \sqrt{\varepsilon/\nu}$ in inner units for each Co and the single phase case SP. The mean profile is computed over the equilibrium period T_{eq} defined in chapter 6 and recorded in table 3.1. 62

5.7 Empirically recovered shear-rate exponents p_1 (a) and p_2 (b), from regressing $K_1(y)$ and $K_2(y)$ in equation (5.8) against the local shear rate, plotted against the cohesive number Co for each aggregate size metric (D_F, D_g, D). Horizontal black lines mark the scaling predicted by Winterwerp [5]: $p_1 = 1$ for the aggregation term (a) and $p_2 = 1.5$ for the breakup term (b). 63

6.1 Number of aggregates N_a in the domain over time t made dimensionless with the mean streamwise velocity U and half channel height h. The full run times are displayed for each Co. The onset the equilibrium period, t_{eq} (equation 5.3), is shown with diamond markers while the beginning of the particle subsampling period is marked with circles. The two periods, T_{eq} and T_{sub}, equilibrium and subsampling respectively, are annotated for $Co = 0.48$. The exponential fits used to determine t_{eq}(equation 5.2 are shown as dashed lines while a gray dash-dotted line shows the total number of primary particles, $N = 3841$. Error bars denote a 95% confidence interval and are evaluated using the methodology described in appendix C. 66

6.2 (a) Mass-weighted aggregate number density $\overline{\overline{nf}}$ as a function of size n for each cohesive strength Co (markers with dashed lines). Error bars denote 95% confidence intervals as defined in appendix C. Log-normal fits for $n > 3$ are shown as solid lines for $Co \geq 0.48$. (b) Plane-and-time averaged aggregate diameter $\overline{D}/d$ over the half channel for each Co. 67

6.3 (a) Fluid $\overline{u}^+$ (solid) and particle $\overline{u_p}^+$ (dashed) mean streamwise velocity profiles in inner units for each Co. (b) Fluid $\overline{k}^+$ (solid) and particle $\overline{k_p}^+$ (dashed) turbulent kinetic energy profiles in inner units for all Co. The single-phase case is included in each panel as a black dash-dotted line while a vertical grey dashed line denotes a particle diameter d^+. Profiles for $\overline{k_p}^+$ are shown with reduced opacity for $y^+ < d^+/2$, where the near-wall singularity in volume fraction makes the plotted (higher-order) statistic increasingly sensitive to sampling noise. 69
6.4 Velocity fluctuations and Reynolds shear stress profiles over the inner-scaled wall-normal distance y^+, for the fluid phase (solid) and the particles (dashed), across cohesive number Co: (a) streamwise, (b) wall-normal, and (c) spanwise velocity fluctuations and (d) Reynolds shear stress. The single phase (SP) statistics are included as a black dash-dotted line. Velocities are normalized by the friction velocity. As in figure 6.3, particle quantities are denoted by a subscript $_p$. 71
6.5 Slice of the instantaneous streamwise velocity fluctuation field taken on the xy-plane. The snapshot is focused on an elongated aggregate which is made black using the fluid indicator function for that slice. The aggregate resides within a region of low-speed flow ($u' < 0$), which it appears to perturb, as evidenced by the red outline ($u' > 0$) directly adjacent to the particles. 73
6.6 (a) Measured friction Reynolds number Re_τ over the cohesive number Co. (b) Wall-normal profile of the volume fraction $\overline{\phi}$ relative to the bulk volume fraction $\phi_0 = 0.015$ for each Co case. A gray dashed horizontal line denotes ϕ_0 while a vertical red dashed line shows $y = d$. The wall-normal coordinate y is made dimensionless using the half channel height h. . . . 74
6.7 Shear stress balance for the cohesive particle laden cases, $Co = [0, 1.5]$, showing wall-normal profiles of the viscous stress (τ_ν), Reynolds shear stress τ_{T_f}, particle Reynolds shear stress τ_{T_P}, and particle induced stress τ_P. The main plot shows the range $\tau = [0, 0.05]$, where τ_P and τ_{T_P} are shown on a red background. The red background highlights the same region in the inset, which shows the full range of total stress $\tau = \tau_w(1-y/h)$ and includes τ_ν and τ_T. 75
6.8 (a) Breakup rate, $\overline{\overline{g_b}}$, versus normalized aggregate size D/d. (b) Rescaled by Co to demonstrate collapse. (c) Compensated by $D^{-2}Co$ to highlight the D^2 scaling. Power law fits $y = AD^2$ are shown as solid lines in each panel. Error bars denote a 95% confidence interval (c.f. figure 6.2 caption). 78

6.9 Probability density function (PDF) of (a) child-to-parent fragment volume ratios, D_c^3/D_p^3, for each $Co > 0$ for breakup and (b) the ratio of parent to child volume Ψ across for aggregation events. For breakup only events where $D_p > 3$ are considered. Similarly, for aggregation, only events where $(D_1^3 + D_2^3)^{1/3} > 3$ are considered. Equation (6.3) is fit to the data for all Co and shown as a black lines in (a) and (b). (c) Ratio of mass of largest fragment to parent aggregate mass $D_{c,L}^3/D_p^3$ for breakup events as a function of parent size D/d. Error bars denote a 95% confidence interval (c.f. figure 6.2 caption). 80

6.10 Aggregation kernel estimator $\overline{\overline{\beta}}^{\circ}$ shown as a matrix over the space of the two parent aggregate sizes D_1/d and D_2/d for (a) $Co = 0.24$(b) $Co = 0.48$, (c) $Co = 1.0$ and (d) $Co = 1.5$. Only bins with more than 10 aggregation events are considered. 81

7.1 Volume- and time-averaged aggregation and breakup source terms, $\overline{\overline{S_i}}$ (a-d) and net aggregation and breakup source terms $\overline{\overline{T_a}}$ and $\overline{\overline{T_b}}$ (e-h). Each column shows data for a single, nonzero cohesive strength. The $\overline{\overline{S_i}}$ are defined in chapter 4 while $\overline{\overline{T_a}}$ and $\overline{\overline{T_b}}$ are given by equations (7.1) and (7.2) respectively. Sizes $n > 1$ where $\overline{\overline{T_a}} > \overline{\overline{T_b}}$ are highlighted with a red background whereas those with $\overline{\overline{T_b}} > \overline{\overline{T_a}}$ have blue backgrounds. 84

7.2 Phase diagram showing the regions in the space of cohesive strength Co and aggregate size D/d where aggregation acts as a source and breakup a sink, $\overline{\overline{T_a}} > 0 > \overline{\overline{T_b}}$, in red and regions where breakup acts as a source $\overline{\overline{T_b}} > 0 > \overline{\overline{T_a}}$ in blue. The form and separation between the regions is drawn through the region bounds measured from the data presented in figure 7.1. The upper and lower bounds of the regions from the data are also marked with black and white circular markers respectively. The maximum aggregate size, shown by black diamonds marks the edge of the regions, with a solid line drawn through the measured data. 86

7.3 The net source due to aggregation and breakup, $\overline{Q}$, aggregation flux $\overline{T_a}$, breakup flux T_b, and advective flux $\partial_y(\overline{nv_n f})$, for three size classes: $n = 1$, $n \in \{2, 3\}$, and $3 < n < 20$ (columns) for $Co = 0.48$ plotted over the half channel height, $y/h \in [0, 1]$. The upper row (a-c) shows the full data range while the bottom row focuses on $\overline{Q}$ and $\partial_y(\overline{nv_n f})$(d-f). A 95% confidence interval is shown by the shaded region surrounding each curve. The gray vertical dashed line corresponds to $y = d$. 88

7.4 The net source due to aggregation and breakup, $\overline{Q}$, aggregation $\overline{T_a}$, breakup $\overline{T_b}$, and advective flux $\partial_y(\overline{nv_n f})$ for three size classes: $n = 1$, $n \in \{2, 3\}$, and $3 < n < 20$ (columns) for $Co > 0$ (rows) plotted over the half channel height, $y/h \in [0, 1]$. As in figure 7.3 (d-f) the axes limits are chosen to focus $\overline{Q}$; a full figure is given in appendix D. A 95% confidence interval is shown by the shaded region surrounding each curve. The gray vertical dashed line corresponds to $y = d$. 90

7.5 Wall-normal advective transport of aggregates, $\partial_y(\overline{nv_n f})$ in (n, y) space for each $Co > 0$ (a-d). Dashed lines are drawn onto the plot to aid in distinguishing between regions of $\partial_y(\overline{nv_n f}) > 0$ (red) and $\partial_y(\overline{nv_n f}) < 0$ (blue). Panel (c) has additional annotation that is used in the text to describe the cyclic transfer of mass through regions 1-4. Symbols with vertical arrows show the divergence of $\overline{nv_n f}$ to compliment the red and blue coloring. 91

7.6 Proportion of aggregates that break over the total number of aggregation and breakup events assigned to each mechanism Φ_b plotted over cohesive strength Co; particle-wall collisions, particle-wall lubrication, and shear-induced breakup. Error bars denote a 95% confidence interval. A schematic showing the definition of the regions relative to the grid spacing is shown as an inset where ζ_{iw} is the distance between the surfaces of particle i and wall w. Note that the particle is drawn smaller relative to the grid spacing than in reality. 94

7.7 Wall-normal profiles of: (a) Orientation angle of the aggregate longest axis with respect to the domain frame of reference, equation 7.8, (b) the angular velocity of aggregates about the spanwise axis, z, (c) mean rate of strain along the aggregate long axis. Each figure only considers aggregates with $n > 2$ and wall-normal bins with $\phi > 10^{-3}$ to avoid singularities in particle phase conditioned statistics. 97

A.1 Probability density distributions of particle Reynolds number Re_p measured over all aggregates in the sampling period T_{eq} for each Co. 107

A.2 Graphical summary of the procedure to compute the particle-fluid slip velocity. 107

C.1 Global autocorrelation as defined by equation (C.2) for all Co. The correlation time, t_{int}, is plotted as a vertical dashed line of matching color for each case. 111

D.1 The net source due to aggregation and breakup, $\overline{Q}$, aggregation $\overline{T_a}$, breakup $\overline{T_b}$, and advective flux $\partial_y(\overline{nv_n f})$ for three size classes: $n = 1$, $n \in \{2, 3\}$, and $3 < n < 20$ (columns) for $Co > 0$ (rows) plotted over the half channel height, $y/h \in [0, 1]$. A 95% confidence interval is shown by the shaded region surrounding each curve. The gray vertical dashed line corresponds to $y = d$. 114

F.1 Breakup fraction Φ_b as a function of cutoff time t_{win}. The selected $t_{win} = h/U$ used in section 7.3 is shown as a vertical red line. 116

Contents

Curriculum Vitae viii

Abstract ix

Nomenclature xi

List of Tables xxi

List of Figures xxii

1 Introduction 1
- 1.1 Motivation . . . 1
- 1.2 Background . . . 2
  - 1.2.1 Sources of cohesion . . . 2
  - 1.2.2 Modeling aggregate transport . . . 3
  - 1.2.3 Cohesive particles in turbulence . . . 5
- 1.3 Objectives and outline . . . 9
- 1.4 Accomplishments . . . 10
- 1.5 Permissions and Attributions . . . 11

2 Numerical methodology 13
- 2.1 Flow solver . . . 13
- 2.2 Close-range interaction forces . . . 16
- 2.3 Collision model without gravity . . . 19
  - 2.3.1 Shear rate scaled stiffness . . . 23

3 Simulations of a turbulent channel laden with cohesive particles 25
- 3.1 Physical configuration . . . 25
- 3.2 Averaging operations . . . 28
- 3.3 Single-phase precursor flow . . . 30
  - 3.3.1 Startup procedure . . . 30
  - 3.3.2 Single-phase validation . . . 31

3.4 Non-cohesive particle-laden validation . . . 33

4 The population balance equation 35
4.1 Formalism . . . 35
4.1.1 The aggregate number density . . . 35
4.1.2 The population balance equation . . . 37
4.1.3 Net transport . . . 39
4.2 PBE averaging procedures and assumptions . . . 39
4.2.1 Plane-and-time averaging . . . 39
4.2.2 Volume-and-time averaged PBE . . . 43
4.3 Aggregate identification . . . 43
4.4 Family tree construction and event classification . . . 45
4.5 Finite-sized particles . . . 47
4.6 Summary . . . 49

5 Aggregate growth and transient statistics 51
5.1 Transient and equilibrium identification . . . 53
5.2 Aggregate size and shape . . . 55
5.3 Aggregate growth . . . 56
5.4 Wall-normal variation . . . 59
5.5 Summary . . . 63

6 Equilibrium statistics 65
6.1 Aggregate number density . . . 67
6.2 Flow modulation . . . 69
6.2.1 Total stress balance . . . 74
6.3 PBE kernels . . . 76
6.4 Summary . . . 81

7 PBE balance 83
7.1 Global PBE balance . . . 83
7.2 Local wall-normal balance . . . 86
7.3 Wall interactions and aggregate fate . . . 93
7.4 Aggregate orientation and axial straining . . . 95
7.5 Summary . . . 99

8 Concluding remarks 100
8.1 Summary . . . 100
8.2 Outlook . . . 103
8.2.1 PR-DNS and Euler-Lagrange simulations . . . 103
8.2.2 Beyond PBE models . . . 104

A Slip velocity 106

B Family tree **108**

C Correlation time and error estimation **109**
C.1 Global autocorrelation and correlation time 110
C.2 Number of samples and error estimation 111

D PBE fluxes, expanded **113**

E Aggregate orientation **115**

F Breakup mechanism windowing sensitivity **116**

Bibliography **117**

Chapter 1

Introduction

1.1 Motivation

Cohesive particles suspended in turbulent flows undergo a complex process of aggregation, breakup, and restructuring, collectively known as *flocculation*, wherein turbulence plays a dual role: facilitating aggregate growth by enhancing collision rates, while simultaneously promoting breakup through increased hydrodynamic stresses [6, 1, 7]. The result of this competition is a dynamic population of aggregates whose size distribution directly controls particle transport and dispersion, making flocculation a central process across a wide range of environmental and engineering systems.

In the ocean, flocculation drives the formation of marine snow, a key mechanism in carbon export and marine ecology [8]. In fluvial and coastal systems, the evolution of aggregate size distributions regulates settling velocities and, in turn, soil erosion and deposition [9, 10]. Aggregates in these environments often form around nutrients and pollutants [11, 12], including microplastics [13], and wildfire contaminants [14]. This mechanism is exploited in engineered systems to remove toxins and metals in water purification processes [15, 16]. In aerospace engineering, the ingestion of aggregated dust

and ash accelerates turbine blade erosion [17]. In pharmaceutical manufacturing, control and efficient design of the widely adopted spray-drying process, where high temperature turbulent flows generated by large machinery are used to break up aggregated powders, remains an open challenge [18, 19]. Dry powder inhalers, devices that require the user to inhale and generate a turbulent flow to break up aggregated powders, are a common method of drug delivery, wherein managing dosage is a persistent design challenge [20, 21, 22, 23, 24]. In each of these examples, the dynamic interplay between aggregation facilitated by turbulent mixing, breakup induced by hydrodynamic stresses, and the evolving morphology of flocs or aggregates plays a central role. Ultimately, accurate modeling and parameterization of the transport of cohesive materials remains an enduring challenge in hydrological modeling, process design, and risk mitigation [25].

1.2 Background

1.2.1 Sources of cohesion

Due to the breadth of applications, aggregation and breakup of cohesive particles span a wide range of material and flow parameters. Fundamental to the problem is the presence of an inter-particle attractive force, here generally termed the *cohesive* force. Particle cohesion can arise from a broad array of mechanisms depending on the surrounding medium and particle composition. At short range, van der Waals (vdW) forces act between any two particles in close proximity, with their importance growing as particle size decreases and the ratio of particle surface area to volume increases [26, 27]. In humid environments, liquid capillary bridges provide an additional source of cohesion [28, 29], while biological growth on particle surfaces (biofouling) [30] can bind particles well beyond the range of vdW forces alone. Cohesion has also been generalized to describe systems

entangled in such a way that the assembly of otherwise non-interacting constituents can sustain tension. Termed geometric cohesion, this behavior is relevant to the entanglement of microplastic fibers, which form effective aggregates similar to those produced by vdW and capillary forces [31, 32]. These mechanisms often act together. In a volcanic eruption, for example, fine ash particles bind through vdW and electrostatic attraction, while capillary bridges form where liquid water or ice is present in the eruption plume; the resulting aggregates range from sub-millimeter to centimeter scale [33]. Marine snow aggregates arise from biologically mediated cohesion and span microns to millimeters in size, occasionally reaching centimeters [8]. Concerningly, these aggregates also interact with geometrically or biologically bound microplastics, leading to their deposition on the sea floor [13]. A comparable size spectrum is documented for cohesive sediment flocs in coastal and estuarine waters, where primary mud and clay particles of order microns combine into micro- and macroflocs spanning micron- to millimeter-scales [34].

The formation of these aggregates is governed by the competition between the cohesive forces holding an aggregate together and the hydrodynamic stresses acting to pull it apart. While simply stated, the broad range of scales, environments, and mechanisms sampled above renders the modeling of cohesive material transport an enduring challenge. Reduced order models address this complexity by collapsing it into a small number of empirical parameters, whose validity across flow conditions and material systems remains an open question and a continuing area of improvement.

1.2.2 Modeling aggregate transport

Current models for cohesive particle transport broadly fall into three categories, trading decreasing computational cost for increased reliance on parameterization: particle-scale methods, where individual primary particles are tracked [35, 36, 37, 38, 39, 10, 40,

41, 42, and references therein], population balance equation (PBE) models, where the size distribution is partitioned into discrete classes that can exchange mass [43, 44, 45, 46, 47, 48, 49, 50, 51, 52, 53, 54, and references therein], and single class models, where a characteristic size is evolved [5, 9, 55, 56, and references therin]. Particle-scale methods are entirely computationally prohibitive at application scales, while single-class models fail to capture critical dynamics such as differential settling [57].

PBE-based methods find some success. Originally adapted from the works of v. Smoluchowski [2, 3] and Levich [58], PBE models evolve the aggregate size distribution by considering a representative set of size classes that are coupled through probabilistic, rate-describing aggregation and breakup kernels. The accuracy of PBE models, therefore, rests entirely on the number of classes considered and the validity of kernel closure models. In practice, however, aggregate size distributions in large-scale target systems can span several orders of magnitude [59], forcing resolution and predictive accuracy to be traded for computational tractability. Only $n_c \approx 20$ size classes are typically employed in Reynolds-averaged Navier-Stokes (RANS)- and large-eddy simulation (LES)-based flow solvers [60, 61], well short of the $n_c \approx 80$ classes suggested to reasonably reproduce aggregate size distribution statistics measured in turbulent mixing tanks [62, 53]. Even when sufficiently resolved, PBE models typically rely on kernel parameterizations that are oversimplified, agnostic to local flow conditions, or both (e.g. aggregates are prescribed to break into two equal fragments [53], a simplification with no clear physical basis). Comparable challenges persist in PBE frameworks for droplet-laden [63, and references therein] and bubbly flows [64, 65, and references therein]. Gaining physical insight into the flocculation process and improving these parameterizations therefore remains a central goal of experimental and numerical work, including the present study.

1.2.3 Cohesive particles in turbulence

Experimental studies have provided key insights into floc growth, size distributions, and morphology in turbulent flows [66, 67, 68, 69, 70]. However, direct observation of aggregation and breakup events requires high-speed imaging and well controlled environments, making such experiments costly and often prohibitive. Notably, Saha et al. [71] captured Lagrangian statistics of breakup in quasi-homogeneous isotropic turbulence (HIT), while Hoffman & Eaton [72] successfully observed individual aggregation and breakup events in a humid turbulent flow laden with glass particles and computed a "sticking efficiency". Still, most experimental investigations are limited to studying individual aggregates in simplified shearing or straining flows [73, 74, 75, 76, 77]. Despite these efforts, measuring hydrodynamic coupling remains difficult due to confounding processes such as settling, which can be suppressed through microgravity experiments, such as those conducted aboard the International Space Station by Kleischmann et al. [78], a nontrivial undertaking in its own right. Furthermore, systematic variation of cohesive forces is currently impractical and an area of ongoing research [79]. As a result, these limitations have motivated a growing body of numerical work on the subject.

Recent numerical studies of cohesive particle-laden turbulence largely employ Euler-Lagrange (EL) frameworks and use either a Lagrangian particle tracking (LPT) approach that represents aggregates as "superparticles" or the discrete element method (DEM) to track individual primary particles. LPT methods typically model aggregation using a probabilistic "sticking efficiency" or energy- or momentum-based thresholds, while breakup is triggered when local stresses exceed a critical value. In contrast, DEM-based EL frameworks incorporate a parameterized cohesive force into the particle momentum equations. In both methods, drag forces are typically computed using the Maxey–Riley–Gatignol equation (MRGE) describing the motion of a small sphere in nonuniform flow

[80]. Critically, the MRGE is formulated for individual, non-interacting particles, which becomes problematic since cohesion results in persistent clustering and high local volume fractions. Although drag corrections accounting for shielding and multi-body effects have been proposed, these remain topics of intensive research and debate [25]. With increased computational expense, Particle-Resolved Direct Numerical Simulation (PR-DNS) frameworks avoid these issues by resolving the flow around individual particles and effectively integrating the hydrodynamic stresses over the particle surfaces [81]. Historically, PR-DNS has been limited to small domains, few primary particles, or low turbulence intensities; however, recent advances in computational capabilities have made PR-DNS increasingly applicable to the study of particle-laden turbulence [82, 83].

With access to detailed data on both flow fields and flocculation events, EL simulations have yielded valuable insight into how, e.g., turbulence intensity, shear rate, cohesive strength, particle size, and volume fraction influence flocculation in HIT (see [75, 40, 84, 25] and references therein) and, to a lesser extent, wall-bounded flow [35, 85, 36, 38, 37, 39, 86].

In a wall-bounded setting, Babler et al. [87] used one-way coupled LPT-DNS to examine the breakup of individually released aggregates. They identified two distinct mechanisms: weaker aggregates broke due to stresses induced by local turbulent fluctuations, whereas stronger aggregates had to migrate closer to a wall before being broken by stresses induced by mean shear. Marchioli & Soldati [88] extended this work by showing that neglecting aggregate response time leads to over prediction of breakup under rapid stress fluctuations. With a similar numerical approach, Breuer & Almohammed [89] investigated a turbulent channel laden with aggregating, but non-breaking, particles and found that aggregation rates peak near the wall, where collision rates are highest. Additional studies employ two-way coupled LPT-DNS or LES to examine both aggregation and breakup in turbulent channel flows. Almohammed & Breuer [36] demonstrated that

flocculation is highly sensitive to the choice of drag model and showed that the inclusion of Saffman lift resulted in an order of magnitude decrease in aggregate count. This was found to be due to the redistribution of particles resulting in lower peak concentrations and collision rates. Consistent with Babler et al. [87], Njobuenwu & Fairweather [38] observed that stronger aggregates had to travel closer towards a wall to break, whereas breakup of weaker flocs occurred more uniformly across the channel.

Complementary CFD-DEM based studies have explored flocculation in wall-bounded turbulence while modeling the primary particles constituting aggregates and employing drag closures to capture hydrodynamics. Afkhami et al. [35] investigated the initial period of aggregate growth and found that aggregation is enhanced in two regions: near the channel wall, due to higher particle concentrations driven by turbophoresis, and in highly turbulent regions, due to higher collision rates. In follow up work, they showed that increasing Reynolds number promotes aggregation when cohesive forces are strong but suppresses it under weak cohesion due to overly energetic collisions [85]. Hærvig et al. [37] explored the role of particle density in a turbulent pipe flow and observed maximum floc size at intermediate Stokes numbers, while Mortimer et al. [86] investigated the role of particle size and showed that at fixed volume fraction, larger particles aggregate more slowly, but exhibit similar dynamics at fixed particle count.

Few studies examine how flocculation feeds back onto the flow itself. An exception is the work of Schutte et al. [39], who found that small agglomerates attenuate turbulence resulting in a drag reduction in both turbulent channel and pipe flows. However, when aggregates size exceeds a critical threshold, drag was found to increase due to an increase in effective viscosity brought on by increased correlation length of the flow.

More recently, modeling efforts have begun to consider flocculation in the bottom boundary layer, where mean shear and coherent structures typical of wall-bounded flows interact with elevated sediment concentrations in complex ways [52, 53]. These studies

highlight the need for improved understanding of flocculation in highly anisotropic flow fields and near-wall regions.

Taken together, this body of work has established that flocculation in wall-bounded turbulence is broadly shaped by the interplay of aggregation and breakup with the wall-normal coordinate: aggregation is enhanced by elevated near-wall collision rates, and breakup is driven by the stresses an aggregate encounters as it migrates through the flow, with the mean shear and turbulence intensity both varying strongly with wall-normal position. Individual studies have shown that stronger aggregates must travel closer to the wall to break [87, 38], that for some regimes of particle and aggregate size, near-wall turbophoresis promotes aggregation [35], and that the resulting flocs can, in turn, modify the near-wall turbulence and drag [39]. These findings, however, should be interpreted with some caution: the dispersive behavior of suspended particulates is highly sensitive to size and density, so the specific outcomes reported in any individual study likely represent one point within a broader spectrum of possible behaviors [83].

Furthermore, with few exceptions [40, 90], most numerical studies report on an initial, aggregation-dominated transient rather than a statistically stationary population. Whether the same spatial organization and rates of aggregation and breakup persist once a dynamic equilibrium between the two is reached remains, to the best of the author's knowledge, unaddressed. More fundamentally, no study has yet examined whether aggregation and breakup themselves balance locally across the wall-normal direction, as opposed to only in a bulk, domain-averaged sense. Since aggregation and breakup are each known to be spatially non-uniform, and since aggregates are advected between regions of differing turbulence intensity and shear over their lifetime, there is no a priori reason to expect the two processes to balance at every wall-normal location individually, even under statistically stationary conditions. Resolving these questions requires simultaneous, spatially resolved access to aggregation, breakup, and transport over a sufficiently

long statistically stationary period, and is the central aim of the present study.

1.3 Objectives and outline

The overarching objective of this dissertation is to characterize the aggregation and breakup of cohesive particles immersed in a turbulent wall-bounded flow, where the effects of the inhomogeneous and anisotropic flow field on aggregation and breakup remain underexplored. To this end, we conduct six simulations of a turbulent channel flow laden with cohesive particles in which the cohesive force strength is varied systematically across cases. The numerical methodology is described in chapter 2, where a correction to the established flow solver is discussed in the context of a collaborative work on the rheology of dense particulate suspensions. The physical configuration and numerical parameters for the channel flow are presented in chapter 3, along with validation for both a single-phase, unladen flow and a particle-laden, non-cohesive flow. A novel plane-averaged PBE formulation for finite-sized particles is developed in chapter 4 alongside descriptions of the aggregate tracking and event identification algorithms later employed to measure aggregation and breakup rates.

The simulations first advance through an aggregation-dominated transient, over which population-level statistics are evaluated against the flocculation model of Winterwerp [5] in chapter 5. The model, originally developed for HIT conditions, is shown to perform adequately when applied with the wall-normal-varying shear rate. Following this transient, a statistically stationary equilibrium period sets in. Eulerian flow statistics are evaluated over this period for both the fluid and solid phases in chapter 6, revealing that the formation of larger aggregates at higher cohesive strength moderately modulates the underlying turbulence and yields a minor reduction in drag relative to the non-cohesive case. Aggregation and breakup statistics are also reported and shown to scale with

cohesive strength and aggregate size.

Finally, the plane-averaged PBE framework is exploited to measure rates of aggregate production and breakup across the space of wall-normal direction and aggregate size. In the bulk-averaged PBE, aggregation and breakup must trivially balance at each size. This balance is shown to break down once the wall-normal dependence is retained revealing regions of net aggregate production and removal in the joins space of size and wall-normal distance. In particular, we find that due to breakup, smaller aggregates are preferentially created near the wall, where shear rates and turbulence intensities are elevated. This results in a net production of small aggregates near the wall that is balanced by advective transport. Indeed, the PBE is shown to close locally in the wall-normal direction once this term is included. Extending this analysis across all sizes reveals a circulation through the joint size-wall-normal space: larger aggregates are overproduced in the channel center, migrate toward a wall, and break, after which the resulting smaller aggregates replenish the center, where they grow once more.

Concluding remarks and an outlook follow in chapter 8.

1.4 Accomplishments

The key contributions of this work are listed below:

- Fully resolved PR-DNS simulations of turbulent channel flow laden with cohesive particles are performed with varying cohesive strengths yielding a broad spectrum of aggregate size distributions. Notably, the simulations reach an equilibrium wherein aggregation and breakup balance, inviting statistical analysis.

- A novel plane-averaged PBE framework is developed to account for finite sized particles and aggregates in chapter 4. Aggregate tracking and event identification

algorithms are built to support this.

- The flocculation model of Winterwerp [5] is shown to adequately capture aggregate growth though the initial transient, with aggregation and breakup rate kernels found to be successfully parameterized by the local turbulence shear rate. This is presented in chapter 5.

- One point turbulent statistics are reported for both the fluid and solid phase in chapter 6 wherein the presence of large aggregates at higher cohesive strength is shown to modulate the underlying turbulent flow field.

- Regions of net aggregate production and depletion are identified in the joint space of wall-normal distance and aggregate size. These regions are found to be sustained by a newly-identified statistical circulation of aggregates through this space. This culminates with the conceptual picture that statistically, small aggregates travel to the channel center, where they coalesce to form larger aggregates, that must again approach the wall in order to break.

1.5 Permissions and Attributions

The content of chapter 5 is adapted from work conducted under the supervision of Prof. Eckart Meiburg and previously published in Acta Mechanica [41]. It is *reproduced with permission from Springer Nature.*

The content of sections 2.1, 2.2, 8.1, and chapter 7 is adapted from work conducted under the supervision of Prof. Eckart Meiburg, in collaboration with Prof. Filippo Coletti at ETH Zurich and his MS student Lukas Widmer, who was co-supervised by myself and Prof. Meiburg at UC Santa Barbara for six months. This work has been submitted for

publication in the Journal of Fluid Mechanics [42]; upon publication, this chapter will be *reprinted with permission of Cambridge University Press.*

The contents of chapters 6 and 7 are also adapted from work conducted under the supervision of Prof. Eckart Meiburg, published in the proceedings of the 14th International Symposium on Turbulence and Shear Flow Phenomena (TSFP14) [91]. Per TSFP policy: *The copyright of TSFP full manuscripts remains with the authors, who are free to submit their work for publication in an archival journal, citing the TSFP full manuscript as preliminary results. Archival journals may also invite selected authors of TSFP full manuscripts to submit their work for publication in special issues.*

The adaptation and reproduction of each of these works is also recorded as a footnote at the beginning of the relevant chapters.

Chapter 2

Numerical methodology[1]

2.1 Flow solver

To investigate the aggregation, breakup, and transport of cohesive particles in wall-bounded turbulence, a simulation campaign of a turbulent channel flow laden with cohesive particles is conducted using the PARTIES (PARTicle laden flows via immersed boundarIES) flow solver developed in the Meiburg Lab at UC Santa Barbara by Biegert et al. [92, 93]. The immersed boundary method (IBM)-based PR-DNS solver uses a marker-and-cell (MAC) grid where fluid velocities are stored at the cell faces while pressure is stored at the cell center [94]. Particles are overlaid on this grid, their surfaces each defined by a spherical shell of Lagrangian marker points that move as a rigid body, tracking translational and rotational motion. Each marker point has a volume of influence, specified by the kernel defined as equation 3.8 in Biegert [93], within which flow velocities are interpolated to the marker point. The velocity difference between the lo-

[1]This chapter contains previously published work, adapted here with minor modifications from the following reference: A. D. Leonelli, L. Widmer, and E. Meiburg, *Aggregation, breakup, and size-dependent transport in a turbulent channel flow with cohesive particles*, 2026. Under review at *J. Fluid Mech.* at the time of dissertation submission.

cal particle solid-body motion at each Lagrangian marker point and the now-collocated fluid velocity is evaluated and used to compute the immersed boundary (IB) force, with the aim of enforcing the no-slip condition. The IB force is then added to the particle momentum equation while its reaction force is conservatively spread back onto the MAC grid by the same interpolation kernel. Importantly, the IBM belongs to a broader class of so-called fictitious domain methods, in which the flow field inside the dispersed phase is a numerical artifact rather than a physically meaningful quantity. This becomes problematic when particles are tightly packed, such as in an aggregate or particle bed. When in close proximity, the volume of influence surrounding a Lagrangian marker point may extend into the interior of an adjacent particle, sampling the artificial flow field within. To mitigate this, marker points whose volume of influence extends into an adjacent particle are excluded from both the computation and spreading of the IB force. It is also worth noting that the lubrication and collision models defined later are calibrated with this in mind, and that including all marker points when particles are in close proximity leads to time step-dependent IB forces [95]. Altogether, the method can be considered as an direct numerical simulation (DNS) flow solver coupled to a DEM code via the IBM.

The flow solver yields the solution to the continuity equation,

$$\boldsymbol{\nabla} \cdot \boldsymbol{u} = 0, \tag{2.1}$$

and momentum equation,

$$\frac{\partial \boldsymbol{u}}{\partial t} + \boldsymbol{\nabla} \cdot (\boldsymbol{u}\boldsymbol{u}) = -\frac{1}{\rho_f}\boldsymbol{\nabla} p + \nu \boldsymbol{\nabla}^2 \boldsymbol{u} + \boldsymbol{f}_{IBM} \tag{2.2}$$

for an incompressible Newtonian fluid with density ρ_f and kinematic viscosity ν. The fluid velocity at a point $\boldsymbol{x} = (x, y, z)$ and time t is denoted by $\boldsymbol{u}(\boldsymbol{x}, t) = (u, v, w)$,

while p denotes the pressure, and $\boldsymbol{f}_{IBM}$ is the numerical IB volume force responsible for coupling the fluid and particles. Note that gravity is neglected in the present study so that suspended particles do not settle. Equations (2.1) and (2.2) are solved on the staggered MAC grid where a second order central finite difference scheme is used to compute the spatial derivatives while temporal integration follows the hybrid Runge-Kutta (RK)/Crank-Nicolson scheme of Rai & Moin [96]. Within this treatment, the convective terms are integrated explicitly using a RK scheme to third-order accuracy in time, while the viscous terms are integrated implicitly using a Crank-Nicolson scheme to second-order accuracy, with the resulting linear system solved via the conjugate gradient method, yielding an overall second-order accuracy in time. Equation (2.1) is then enforced by solving a Poisson equation for a pseudo-pressure used to project the velocity field obtained from the advective and viscous updates onto a divergence-free space. This is done efficiently by using the fast Fourier transform along periodic directions or the cosine transform for wall-bounded directions.

The particle linear momentum equation,

$$m_{p,i}\frac{\mathrm{d}\boldsymbol{u}_i^P}{\mathrm{d}t} = \oint_{\Gamma_i} \boldsymbol{\tau}\cdot\boldsymbol{n}_i^P \mathrm{d}A + \boldsymbol{F}_{c,i}, \tag{2.3}$$

and angular momentum equation,

$$I_{p,i}\frac{\mathrm{d}\boldsymbol{\omega}_i^P}{\mathrm{d}t} = \oint_{\Gamma_i} \boldsymbol{r}_i^P \times \left(\boldsymbol{\tau}\cdot\boldsymbol{n}_i^P\right) \mathrm{d}A + \boldsymbol{T}_{c,i}, \tag{2.4}$$

are solved concurrently. Here, $\boldsymbol{u}_i^P(t) = (u_i^P, v_i^P, w_i^P)$ and $\boldsymbol{\omega}_i^P(t) = (\omega_{x,i}^P, \omega_{y,i}^P, \omega_{z,i}^P)$ are the linear and angular velocities of particle i, Γ_i its surface, $\boldsymbol{r}_i^P = \boldsymbol{x} - \boldsymbol{x}_i^P$ is the displacement vector from its center, $\boldsymbol{x}_i^P(t) = (x_i^P, y_i^P, z_i^P)$, and $\boldsymbol{n}_i^P$ is the unit surface normal vector. The mass and moment of inertia of particle i are denoted as $m_{p,i} = \rho_{p,i}V_{p,i}$

and $I_{p,i} = \pi\rho_{p,i}\, d_i^5 \,/\, 60$, respectively, where d_i, $\rho_{p,i}$, and $V_{p,i} = \pi d_i^3/6$, are its diameter, density, and volume. The hydrodynamic stress tensor $\boldsymbol{\tau} = -p\boldsymbol{I} + 2\rho_f\nu\boldsymbol{E}$ with $\boldsymbol{E} = \left(\boldsymbol{\nabla u} + \boldsymbol{\nabla u}^T\right)/2$ is, in effect, integrated over Γ_i via the IBM, while the contact forces, $\boldsymbol{F}_{c,i}$, and torques, $\boldsymbol{T}_{c,i}$, act when surfaces are sufficiently close. The ordinary differential equations (2.3) and (2.4) are solved using the same explicit three-step RK scheme as the advective terms in equation (2.2), but with each fluid time step subdivided into 15 particle substeps, over which the RK integration of equations (2.3) and (2.4) is advanced. This finer sub-stepping is necessary to adequately resolve the short-range lubrication forces in time [92]. The contact forces, including the lubrication model, are discussed next.

2.2 Close-range interaction forces

Included in $\boldsymbol{F}_{c,i}$ are the cohesive force, $\boldsymbol{F}_{coh,ij}$, the lubrication force, $\boldsymbol{F}_{\ell,ij}$, and the normal $\boldsymbol{F}_{n,ij}$ and tangential $\boldsymbol{F}_{t,ij}$ collision forces. The net contact force acting on particle i, accumulated over all interacting partners j and walls w is,

$$\boldsymbol{F}_{c,i} = \sum_w \left(\boldsymbol{F}_{\ell,iw} + \boldsymbol{F}_{n,iw} + \boldsymbol{F}_{t,iw}\right) + \sum_{j,j\neq i} \left(\boldsymbol{F}_{\ell,ij} + \boldsymbol{F}_{n,ij} + \boldsymbol{F}_{t,ij} + \boldsymbol{F}_{coh,ij}\right), \tag{2.5}$$

with the associated net torque $\boldsymbol{T}_{c,i}$,

$$\boldsymbol{T}_{c,i} = \sum_w \frac{d_i}{2}\boldsymbol{e}_{iw}^P \times \boldsymbol{F}_{t,iw} + \sum_{j,j\neq i} \frac{d_i}{2}\boldsymbol{e}_{ij}^P \times \boldsymbol{F}_{t,ij}. \tag{2.6}$$

Here, $\boldsymbol{e}_{ij}^P = \boldsymbol{r}_{ij}^P/\|\boldsymbol{r}_{ij}^P\|$ (with $\boldsymbol{r}_{ij}^P = \boldsymbol{x}_j^P - \boldsymbol{x}_i^P$) is the unit vector directed from the center of particle i to particle j, and $\boldsymbol{e}_{iw}^P = \boldsymbol{r}_{iw}^P/\|\boldsymbol{r}_{iw}^P\|$ (with $\boldsymbol{r}_{iw}^P = \boldsymbol{x}_{iw} - \boldsymbol{x}_i^P$) is similarly the unit vector directed from the center of particle i to $\boldsymbol{x}_{iw}$, the point on wall w closest to

the center of particle i. Since the walls in this work are always flat, $\boldsymbol{x}_{iw}$ reduces to the orthogonal projection of $\boldsymbol{x}_i^P$ onto wall w.

Contact occurs when the surface distance between particle i and j, $\zeta_{ij} = \|\boldsymbol{r}_{ij}^P\| - (d_i + d_j)/2 \leq 0$, in which case the nonlinear spring-dashpot model for the normal direction,

$$\boldsymbol{F}_{n,ij} = -k_n |\zeta_{ij}|^{3/2} \boldsymbol{e}_{ij}^P - b_n \boldsymbol{g}_{ij} \tag{2.7}$$

acts to repel the particles, where $\boldsymbol{g}_{ij} = \left[(\boldsymbol{u}_i^P - \boldsymbol{u}_j^P) \cdot \boldsymbol{e}_{ij}^P\right] \boldsymbol{e}_{ij}^P$ is the relative normal velocity between the two particles. The stiffness and damping coefficients, k_n and b_n, are adaptively selected for every collision to achieve a prescribed restitution coefficient, $e = -u_{out}/u_{in}$, the ratio of outgoing to incoming normal relative speeds immediately before and after impact. The tangential forces during contact are formulated using a linear spring-dashpot model subject to a Coulomb friction limit,

$$\boldsymbol{F}_{t,ij} = \min\left(\|\boldsymbol{F}_{s,ij}\|, \|\mu_t \boldsymbol{F}_{n,ij}\|\right) \boldsymbol{e}_{t,ij}, \tag{2.8}$$

where

$$\boldsymbol{F}_{s,ij} = -k_t \boldsymbol{\zeta}_{t,ij} - b_t \boldsymbol{g}_{t,ij}, \tag{2.9}$$

is the tangential spring-dashpot force. Here, μ_t is the friction coefficient, $\boldsymbol{g}_{t,ij}$ is the tangential component of the relative surface velocities, $\boldsymbol{e}_{t,ij} = \boldsymbol{F}_{s,ij}/\|\boldsymbol{F}_{s,ij}\|$, and $\boldsymbol{\zeta}_{t,ij}$ is the tangential displacement computed from the accumulated relative tangential motion between the contacting surfaces (see Biegert et al. [92, 93] for detailed formulations). Similar to the normal collision model, k_t and b_t are adaptively computed for each collision following Biegert et al. [92, 93]. The friction coefficient μ_t is determined by the contact state. For a stationary (rolling or sticking) contact point, particles resist tangential motion up to a threshold set by the static friction coefficient μ_s; once the tangential

force exceeds this threshold, the contact transitions to sliding and μ_t is set to the kinetic friction coefficient, $\mu_k < \mu_s$, until the tangential force falls below the static threshold once more.

When the separation between two surfaces becomes less than the width of two grid cells, $\zeta_{ij} < 2\Delta x$, the squeezing flow between the two surfaces can no longer be resolved. In consequence, the close-range hydrodynamic force does not diverge as expected. The unresolved lubrication force is modeled by adapting the analytical solutions of Cox & Brenner [97] for a sphere approaching a no-slip wall, and for two spheres approaching one another (equivalently formulated as a single sphere approaching a free-slip wall). Both solutions assume Stokes flow conditions with their adaptations given by,

$$\boldsymbol{F}_{\ell,ij} = \begin{cases} -\dfrac{3\pi\rho_f \nu {d_{ij}^*}^2}{8\max(\zeta_{ij}, \zeta_{min})}\boldsymbol{g}_{ij} & 0 < \zeta_{ij} \leq 2\Delta x, \\ 0 & \text{otherwise}, \end{cases} \tag{2.10}$$

where $d_{ij}^* = d_i d_j/(d_i + d_j)$ is the effective diameter accounting for polydisperse particles, and $\zeta_{min} = 1.5 \times 10^{-3} d_{50}$ is a regularizing constant, calibrated by Biegert et al. [92], which can be interpreted as the scale of surface defects, defined here relative to the mean particle diameter d_{50}. For particle-wall collisions, $d_j \to \infty$ giving $d_{ij}^* \to d_i$. In the tangential direction, the IBM accurately captures the lubrication force arising from the side-by-side approach of two particles or tangentially moving surfaces [98], so no tangential lubrication model is necessary.

Finally, and most central for this work, the cohesive force, $\boldsymbol{F}_{coh,ij}$ is modeled using the formulation of Vowinckel et al. [10],

$$\boldsymbol{F}_{coh,ij} = \begin{cases} -\dfrac{A_H d_{ij}^*}{2\zeta_0 \lambda^3}\left(\zeta_{ij}^2 - \zeta_{ij}\lambda\right)\boldsymbol{e}_{ij}^P, & 0 < \zeta_{ij} \leq \lambda, \\ 0, & \text{otherwise}, \end{cases} \tag{2.11}$$

which provides a computationally efficient approximation of the short-range attractive forces predicted by the Derjaguin–Landau–Verwey–Overbeek (DLVO) theory of vdW interactions. Here, ζ_0 represents the scale of microscopic surface asperities, distinct from the regularizing length scale ζ_{min} introduced for the lubrication model. The parameter λ defines the finite range over which the cohesive force is distributed, and must be set comparable to the other length scales in the problem to not impose computational constraints. Following Vowinckel et al. [10], who show that pairwise interactions are relatively insensitive to λ, it is taken as $\lambda = d_{50}/20$. The Hamaker constant, A_H, characterizes the net short-range adhesion between particles, encapsulating the combined influence of particle and fluid material properties. Interpreted here as an effective value, it may therefore also represent additional adhesive mechanisms beyond vdW interactions alone, such as polymer bridging or biofilm-mediated cohesion. Notably, $\boldsymbol{F}_{coh,ij}$ acts only between particles, never between a particle and wall, consistent with equation 2.5 and true for every case in this work where cohesion is active.

2.3 Collision model without gravity

This section documents a numerical issue identified in the PARTIES solver over the course of the collaborative work presented in Khodabakhshi et al. [99], wherein we numerically replicate the rheological experiments of Tapia et al. [100] to investigate the role of long-range hydrodynamic forces and boundary conditions in setting the effective suspension viscosity. When a dense particulate suspension (bulk volume fraction $0.5 \lesssim \phi_0 \lesssim 0.63$) undergoes increasingly rapid deformation, it transitions from the so-called "viscous regime," on which particle interactions are dominated by close-range lubrication forces, to the so-called "inertial" or "Bagnoldian" regime, in which the effective shear and normal viscosities, η_e and $\eta_{e,n}$, are observed to scale with the square

of the deformation rate, $\dot{\gamma}^2$, in agreement with Bagnold's 1954 observations and theory for the collision-dominated kinematics of dry granular materials [101]. This transition is characterized by the Stokes number $St = \rho_p d_{50}^2 \dot{\gamma}/\eta_f$, where η_f is the fluid dynamic viscosity, with the transition reportedly taking place at $St \approx 10$ [100].

The "numerical rheometer" consists of a domain of size $L_x \times L_y \times L_z = 11d_{50} \times 7d_{50} \times 10d_{50}$, filled with a dense suspension ($\phi_0 \in \{0.52, 0.545\}$) of neutrally buoyant ($\rho_s = \rho_p/\rho_f = 1$), nearly monodisperse, spherical particles of diameter $d_{50} \pm 0.019d_{50}$ immersed in a Newtonian fluid with dynamic viscosity η_f. The domain is periodic in the streamwise, x, and spanwise, z, directions, while the no-slip condition is enforced at $y = 0$ and $y = 7d_{50}$. Rather than allowing the suspension to interact directly with smooth walls, which results in significant slip between wall and suspended particles, a layer of particles of diameter d_{50} is placed directly adjacent to each wall, at $y = 0.5d_{50}$ and $y = L_y - 0.5d_{50}$, and moves with the wall velocity, producing an effective center-to-center gap of $H = L_y - d_{50}$. The upper particle layer is driven with streamwise velocity u_w and the lower layer with $-u_w$, so that a target shear rate $\dot{\gamma} = 2u_w/H$ is achieved. Across all cases, $\dot{\gamma}$ is varied to span the full viscous to inertial range of $St \in [0.5, 100]$.

We must revisit the collision model, and in particular the normal collision stiffness k_n, which, as described in section 2.2, is adaptively selected for each collision. The overarching goal of the model is to accurately reproduce collision kinematics while minimizing overlap between surfaces (hence the "soft-sphere" name). Note that the particles do not deform, so the model should not be considered a proxy for simulating soft materials such as hydrogels [102]. To prevent large overlap, PARTIES enforces a maximum relative overlap distance, $\min \zeta_{ij} > -\epsilon d_{50}$, with $\epsilon = 5 \times 10^{-4}$, through the following procedure.

A collision is initiated when the surface distance between two particles, ζ_{ij} (or ζ_{iw} in the case of a particle and wall), becomes negative. The closing speed between the two surfaces is then computed at the moment of initial contact, t_c, as $u_{in} = \|\boldsymbol{g}_{ij}(t_c)\|$,

which defines an effective collisional Stokes number, $St_{in} = \rho_p u_{in} d_{50}/\eta_f$. Biegert et al. [92, 93], following Kempe & Fröhlich [103], found that agreement with the experiments of Gondret et al. [104] improved when hydrodynamic and buoyancy forces are omitted from the particle momentum equations for collisions with Stokes numbers above a critical value, $St_{crit} = 5$. For collisions with $St_{in} > St_{crit}$, the stiffness is given by

$$k_n = \frac{m_{eff,ij}}{\sqrt{u_{in} t_*^5}}, \tag{2.12}$$

where $m_{eff,ij} = m_{p,i} m_{p,j}/(m_{p,i} + m_{p,j})$ is the effective mass, which accounts for differences between colliding particles, and t_* is a collision time constant defined in Biegert et al. [92]. For later reference, note that t_* is proportional to the solver time step Δt, $t_* \propto \Delta t$. Of particular relevance here, $k_n \to \infty$ as $u_{in} \to 0$. To prevent overly stiff particles, and the associated unnecessary constraint on the simulation time step, k_n is instead evaluated at $u_{in} = u_{in,crit}$ in equation (2.12) for collisions with $St_{in} < St_{crit}$, where $u_{in,crit} = 9 St_{crit} \eta_f/(\rho_p d_{50})$. This substitution, however, becomes problematic for simulations at lower Reynolds number ($Re = \rho_f \dot{\gamma} d_{50}^2/\eta_f = St/\rho_s$), where η_f, and therefore $u_{in,crit}$, is large: the resulting k_n becomes small, permitting excessive overlap. Biegert et al. [92] rectified this by instead evaluating

$$k_n = \max(k_{n,crit}, k_{n,grav}), \tag{2.13}$$

where $k_{n,crit}$ is equation (2.12) evaluated at $u_{in,crit}$, and

$$k_{n,grav} = \max\left[m_{p,i} g (\epsilon d_i/2)^{-3/2}, m_{p,j} g (\epsilon d_j/2)^{-3/2}\right] \tag{2.14}$$

is the stiffness required to support the dry weight of the heaviest particle. Crucially, in the absence of gravity, $k_{n,grav} \to 0$, so enduring collisions are governed solely by the fixed

floor $k_{n,crit}$, which, as already mentioned, can be too low for simulations with low Re, as there is no mechanism for k_n to adapt to forces imposed by an external shear rate. As a result, particle contacts in a sheared, gravity-free suspension can become substantially softer than intended, permitting overlaps well in excess of the target $-\epsilon d_{50}$. This effect is shown in figure 2.1(a), where the minimum surface distance between two suspended particles, $\min \zeta_{ij}$, is shown normalized by the particle diameter across the full range of St we consider in Khodabakhshi et al. [99]. At low St, the minimum overlap recorded over a simulation is found to be $\min \zeta_{ij} = -0.24 d_{50}$, where a negative sign denotes that the particles are intersecting. As St is increased, collisions increasingly satisfy $St_{in} > St_{crit}$, and the minimum overlap recovers to approximately $\min \zeta_{ij} = -0.05 d_{50}$, which is still much larger than the overlap $k_{n,grav}$ is designed to enforce.

Compounding this issue is that t_* enters the characteristic collision time through k_n and $k_{n,crit}$, which in turn set the time step Δt_{k_n} required to adequately resolve the collision, with $\Delta t_{k_n} \propto k_n^{-1}$. The simulation time step is itself adaptively selected as $\Delta t = \min(\Delta t_{k_n}, \Delta t_{CFL})$, where Δt_{CFL} is the time step requirement for the flow solver set by the Courant–Friedrichs–Lewy (CFL) condition. This coupling introduces a feedback mechanism: for configurations in which most collisions satisfy $St_{in} < St_{crit}$, $k_{n,crit}$ evaluated at the subsequent time step depends on its own present value, which is already small. As the time step grows, t_* grows correspondingly, further decreasing $k_{n,crit}$ for the next collision. The minimum overlap in a simulation is again computed, this time for a fixed $St = 0.5$ but at various CFL numbers, $\mathcal{C} \in [0.05, 0.8]$, so the time step dependence can be evaluated. As expected, and shown in figure 2.1(b), $\min \zeta_{ij}$ monotonically decreases from approximately -0.02 for $\mathcal{C} = 0.05$ to -0.24 for $\mathcal{C} = 0.8$. This trend reflects the increase in Δt with $\mathcal{C}$ leading to a reduction in $k_{n,crit}$, with effects compounded by the feedback mechanism described above.

Under gravity, this feedback is not a concern, since Δt_{k_n} is limited by $k_{n,grav}$. How-

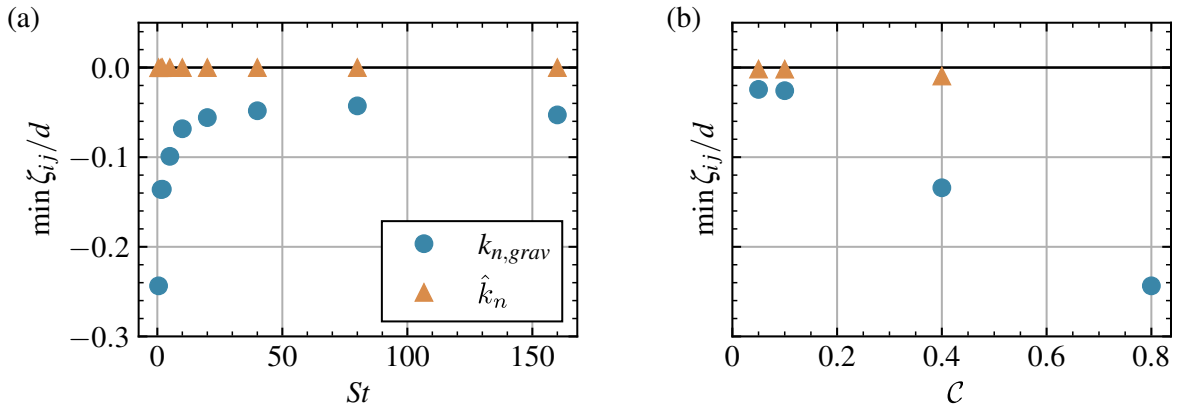


Figure 2.1: Minimum surface distance between two particles, $\min \zeta_{ij}/d_{50}$, for a series of independent simulations of a sheared suspension at (a) CFL number $\mathcal{C} = 0.8$ across a range of Stokes numbers, St, and (b) $St = 0.5$ across a range of CFL numbers, $\mathcal{C}$.

ever, one advantage of the numerical rheometer is that particle settling can be removed by neglecting gravity, allowing suspensions of non-neutrally buoyant particles to be considered without concern for sedimentation. To retain this capability while avoiding the feedback described above, a new threshold is required to clamp $k_{n,crit}$.

2.3.1 Shear rate scaled stiffness

In order to keep particle overlap small ($\min \zeta_{ij} > -\epsilon d_{50} = -5 \times 10^{-4} d_{50}$) during collision, the collision time scale t_c must be small relative to the characteristic time scale of the imposed flow, $t_f = \dot{\gamma}^{-1}$, i.e., the dimensionless ratio $\Theta = t_c/t_f$ must remain small. The collision time scale is given by the model of Kempe & Fröhlich [105] as

$$t_c = 2.439 \left(\frac{m}{k_n}\right)^{2/5} u_{in}^{-1/5}. \tag{2.15}$$

Taking $m \sim \rho_p d_{50}^3$ and $u_{in} \sim \dot{\gamma} d_{50}$, where ρ_p and d_{50} are the particle density and diameter, equation (2.15) gives

$$\Theta \sim \dot{\gamma} \left(\frac{\rho_p d_{50}^3}{k_n}\right)^{2/5} (\dot{\gamma} d_{50})^{-1/5}. \tag{2.16}$$

Introducing the dimensionless stiffness, $\hat{k} = k_n / \left(\rho_f \dot{\gamma}^2 d_{50}^{5/2}\right)$, this reduces to

$$\Theta = \left(\frac{\rho_s}{\hat{k}}\right)^{2/5}, \tag{2.17}$$

which, since $\rho_s = 1$, simplifies to $\Theta = \hat{k}^{-2/5}$. The value of Θ required for particles to behave as effectively hard spheres is generally determined empirically, with reported values in the literature typically in the range $\Theta \approx 10^{-3}$–10^{-4} [106].

We adopt a shear-rate-scaled stiffness, in which k_n is set directly by the imposed shear rate $\dot{\gamma}$ so that Θ remains below a fixed threshold. To reduce computational cost, k_n may be scaled on a case-by-case basis rather than fixed at a single value calibrated to the largest shear rate expected across an entire parametric sweep. The latter, more conservative choice necessarily requires a smaller time step, including in cases where the shear rate is much lower and a smaller k_n would otherwise have sufficed.

Following this convention, we select k_n so that $\Theta = 2.6 \times 10^{-4}$ in Khodabakhshi et al. [99]. The increased stiffness comes at the cost of a correspondingly small time step. Despite this computational cost, the approach enabled the numerical reproduction of the experiments of Tapia et al. [100], yielding insight into the suspension microstructure and enabling a detailed analysis demonstrating that the wall geometry sets the strength of crystallization and, consequently, the effective shear and normal viscosities.

Importantly, the simulations that are the main focus of this work, a turbulent channel laden with cohesive particles, employ this newly implemented constant stiffness; however, due to the relatively lower shear rate, a lower value of k_n may be taken, allowing for a larger and less computationally demanding time step.

Chapter 3

Simulations of a turbulent channel laden with cohesive particles[1]

3.1 Physical configuration

A channel of dimensions $(L_x, L_y, L_z) = (6h, 2h, 3h)$, half-height h, is filled with a Newtonian fluid laden with $N = 3841$ (volume fraction $\phi_0 = N\pi d^3/(6L_xL_yL_z) = 0.015$) cohesive particles, cf. figure 3.1. The particles are monodisperse with a diameter of $d = 2h/31$ and neutrally buoyant, with a particle to fluid density ratio of $\rho_s = 1$, and corresponding Stokes numbers of,

$$St = \frac{\rho_s Re_{p,e}^2}{18} = 7.5. \tag{3.1}$$

[1]This chapter contains previously published work, adapted here with minor modifications from the following references: A. Leonelli and E. Meiburg, *On the effects of anisotropy on the flocculation of cohesive particles in turbulence*, *Acta Mech.* 237 (2026), no. 4, 1699–1713. & A. D. Leonelli, L. Widmer, and E. Meiburg, *Aggregation, breakup, and size-dependent transport in a turbulent channel flow with cohesive particles*, 2026. under review at *J. Fluid Mech.* at the time of dissertation submission.

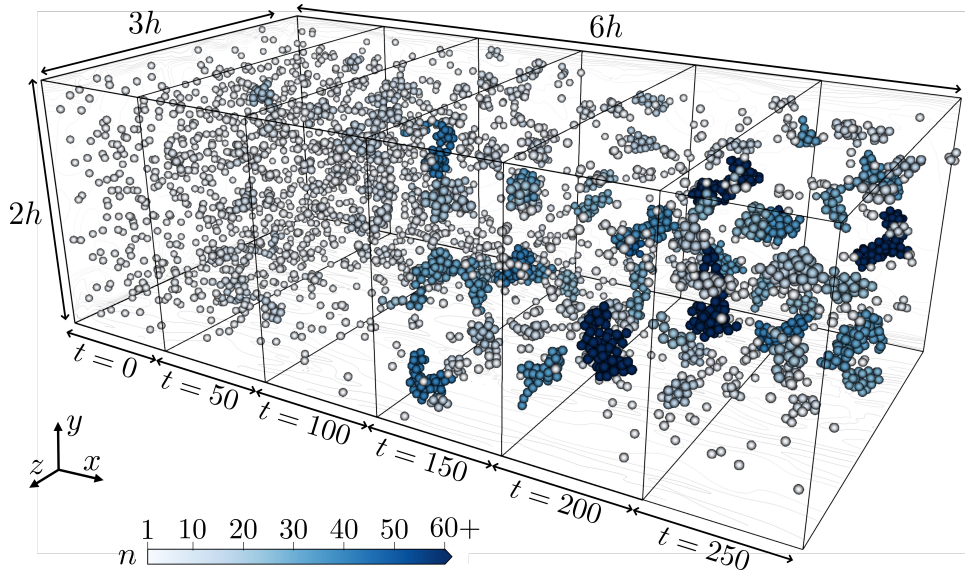


Figure 3.1: Schematic of the simulation domain. Slices from case $Co = 1$ are shown sequentially along the channel for increasing times, with aggregates colored by the number of constituent particles.

Here $Re_{p,e} = u_\tau d/\nu_f = d^+ = 11.6$ is the effective particle Reynolds number which is formulated with the friction velocity $u_\tau = \sqrt{\tau_w/\rho_f}$ and wall shear stress τ_w, made a priori assuming a friction Reynolds number $Re_\tau = u_\tau h/\nu = 180$. Quantities made dimensionless with u_τ and the wall-unit $\delta_\nu = \nu/u_\tau$ are denoted with a superscript $+$ hereafter. The streamwise (x) and spanwise (z) directions are periodic while no-slip walls are imposed at $y = 0$ and $y = 2h$. An adaptive pressure gradient maintains a constant bulk velocity U and Reynolds number $Re = Uh/\nu = 2800$, which corresponds to the well-studied friction Reynolds number of $Re_\tau = 180$ [107]. The domain is discretized using a cubic mesh with grid spacing $\Delta x = h/186$ ($N_x \times N_y \times N_z = 1116 \times 372 \times 558$) so that the characteristic length scale at the wall, δ_ν, is sufficiently resolved: $\delta_\nu/\Delta x = 0.9678$. The particle boundary layers are also resolved, even those at the extreme ends of aggregates. To verify this we follow the procedure detailed in appendix A to compute the effective slip velocity between particle i and the fluid, $\Delta \boldsymbol{u}_i^{PF}$, and subsequently the *a posteriori* particle Reynolds number, $Re_{p,i} = \|\Delta \boldsymbol{u}_i^{PF}\| d/\nu$. Over all cases, $\max_i Re_{p,i} \leq 48.58$, so the

minimum particle boundary layer is estimated to be $\min_i \delta_{p,i} \approx d/\sqrt{\max_i Re_{p,i}} = 1.65\delta_\nu$ and is therefore resolved. Furthermore, the particle resolution of $d/\Delta x = 12$ matches past IBM based PR-DNS studies in turbulent channel flow at a minimum of $Re_\tau = 180$ [108, and references therein]. It should also be noted that the ratio of particle diameter to Kolmogorov length scale, η, is large in this work, with $d/\eta \approx 6.78$ at $y = 0.06h$ and $d/\eta \approx 3.15$ at the centerline on average. While η is appropriately resolved, the implications of the particle size are discussed later. Lastly, validation for a single-phase and cohesionless suspension is discussed in sections 3.3 and 3.4 respectively, with detailed validation of the hydrodynamics and collision schemes against experimental observations reported by Biegert et al. [92], to excellent agreement. Further convergence analysis and comparison to empirical and theoretical settling velocities for single- and multi-sphere aggregates at particle Reynolds numbers up to $Re_p = 100$ were performed by Vowinckel et al. [10] and Maches et al. [109].

The cohesive force, equation (2.11), is characterized by the cohesive number,

$$Co = \frac{\max\|\boldsymbol{F}_{coh,ij}\|}{\rho_f U^2 d^2} \tag{3.2}$$

which quantifies the ratio of maximum cohesive force to a characteristic particle inertial force. In order to observe measurable aggregation for the present particle size and Re we select $Co = \{0, 0.24, 0.48, 1.0, 1.5\}$. As mentioned in chapter 2, given the limitations on particle size in PR-DNS, the Hamaker constant should be interpreted as an effective constant; taking the properties of water, $\nu = 1.002 \times 10^{-6}\,\mathrm{m}^2/\mathrm{s}$ and $\rho_f = 1000\,\mathrm{kg/m}^3$, and a surface asperity scale of $\zeta_0 = 0.2\,\mathrm{nm}$ [110], yields $A_H = \mathcal{O}(10^{-16}\text{-}10^{-15})\,\mathrm{J}$, whereas $A_H = \mathcal{O}(10^{-20}\text{-}10^{-18})\,\mathrm{J}$ for materials such as quartz in water [111, 112].

Particles are initially distributed randomly, without overlap, throughout a fully developed single-phase channel flow, with each particle assigned the mean linear and angular

Name	Co	$t_{eq}u_\tau/h$	$T_{eq}u_\tau/h$	$T_{sub}u_\tau/h$	Re_τ
C0	0	0.1	48.1	3.0	190.3
C1	0.12	7.9	66.9	12.4	189.5
C2	0.24	9.2	50.0	—	190.1
C3	0.48	15.5	71.3	32.5	189.5
C4	1.00	23.2	33.4	16.6	186.5
C5	1.50	26.3	28.9	15.7	184.2
SP	—	—	35.0	—	178.9

Table 3.1: Summary of simulation parameters, timing, sampling periods, and friction Reynolds number. The time for the aggregate population to equilibrate is reported as, t_{eq}. T_{sub} is the subs-sampling period within which aggregation and breakup statistics are reported in chapters 6 and 7, and falls within the broader sampling period T_{eq}, which is defined along with t_{eq} in chapter 5. The time periods are made dimensionless by the large eddy turnover time u_τ/h. For the single phase case, SP, time used to compute statistics after discarding transients, as described in section 3.3 is reported as T_{eq}. Finally, the friction Reynolds number, Re_τ, computed over T_{eq} is reported. Case C2 was not sub-sampled and therefore does not appear in section 6.3 and chapter 7.

velocities of the replaced fluid. At time $t = 0$ the particles are released and the simulations are marched forward, allowing particles to aggregate, fragment, and redistribute in the turbulent flow. The fluid is advanced using a time step Δt_f that is continuously adapted so that the Courant number, $\mathcal{C}$, satisfies the Courant–Friedrichs–Lewy condition, $\mathcal{C} \leq 0.5$. Particle kinematics are evaluated using a sub-stepping routine with time step $\Delta t_p = \Delta t_f/15$. In the spatiotemporal schematic of figure 3.1, the domain is partitioned into six temporal segments along the streamwise direction to illustrate aggregate growth. A summary of the numerical parameters, as well as timing data and the friction Reynolds number for each case are reported in table 3.1.

3.2 Averaging operations

Throughout this work, several averaging operations are frequently used. For convenience and clarity, they are defined here rather than in place.

Given the domain Ω, averaging an observable $f(\mathbf{x}, t)$ over parallel wall-normal planes yields the plane-average operation, denoted in this work by a single tilde, $\widetilde{\cdot}$,

$$\widetilde{f}(y,t) = \frac{1}{L_x L_z} \int_0^{L_z} \int_0^{L_x} f(\mathbf{x}, t) \mathrm{d}x \mathrm{d}z. \tag{3.3}$$

Further averaging $\widetilde{f}(y,t)$ over the wall-normal coordinate yields the volume averaged quantity, denoted by a double tilde, $\widetilde{\widetilde{\cdot}}$,

$$\widetilde{\widetilde{f}}(t) = \frac{1}{L_y} \int_0^{L_y} \widetilde{f}(y,t) \mathrm{d}y. \tag{3.4}$$

A temporal average over a time interval T is defined as,

$$\langle f \rangle(\mathbf{x}) = \frac{1}{T} \int_t^{t+T} f(\mathbf{x}, t) \, \mathrm{d}t, \tag{3.5}$$

and is denoted using angled brackets, $\langle \cdot \rangle$.

Applying this time averaging to equations (3.3) and (3.4) thus yields the plane-and-time averaged and volume-and-time averaged values,

$$\overline{f}(y) = \frac{1}{T} \int_t^{t+T} \widetilde{f}(y,t) \mathrm{d}t \tag{3.6}$$

and

$$\overline{\overline{f}} = \frac{1}{T} \int_t^{t+T} \widetilde{\widetilde{f}}(t) \mathrm{d}t. \tag{3.7}$$

Here, a single bar $\overline{\cdot}$ indicates the plane-and-time-averaging operation while a double bar, $\overline{\overline{\cdot}}$ indicates a volume-and-time averaged quantity.

It also follows that the fluctuations of a quantity $f'(\mathbf{x}, t)$, denoted by an apostrophe, follow as,

$$f'(\mathbf{x}, t) = f(\mathbf{x}, t) - \langle f \rangle(\mathbf{x}), \tag{3.8}$$

and can be further subjected to the averaging operations defined above.

3.3 Single-phase precursor flow

3.3.1 Startup procedure

As mentioned in section 3.1, particles are dispersed into a fully developed single-phase turbulent channel flow. The steps used to generate this precursor simulation are detailed below.

1. A channel laden with spheres of diameter $d/h = 9$ is initialized with a laminar Poiseuille flow profile with bulk velocity U, at $Re = 2800$. Particles are made large and set to a high volume fraction, $\phi_{startup} = 0.1$, so that the resulting perturbations to the flow occur at scales much larger than the expected Kolmogorov scale; this choice also keeps the total particle count low, $N = 2506$, aiding computational efficiency. For the same reason, a coarser grid spacing of $\Delta x = 2h/288$ is employed. Note that at this spacing, the wall unit for the target $Re_\tau = 180$ is not fully resolved: $\Delta x^+ = 1.25$. The simulation is advanced for $3.2\, h/u_\tau$, where h/u_τ is the large-eddy turnover time.

2. A single-phase flow is created by removing the particles from the computational domain and advancing the simulation until the mean total shear stress profile is linear and statistical stationarity is reached, over approximately $22.5\, h/u_\tau$.

3. The fluid and pressure fields are interpolated onto a refined grid with spacing $\Delta x = 2h/372$, which sufficiently resolves the wall unit, $\Delta x^+ = 0.97$. The simulation is advanced until the shear stress profile is again linear, an additional $45\, h/u_\tau$. This period includes the sampling window for the single-phase case, for which the first

$10\,h/u_\tau$ are discarded.

4. The final output of the single-phase simulation above is then used to initialize the cohesive-particle simulations used in this study.

3.3.2 Single-phase validation

To assess the statistical stationarity of the flow, the wall-normal shear stress balance is evaluated and presented in figure 3.2(a). Since the flow is driven solely by the streamwise pressure gradient, the mean total shear stress must follow the profile $\overline{\tau}(y) = \tau_w(1 - y/h)$ [113]. Evaluating the mean wall-normal profiles of the two contributions to $\overline{\tau}$, the viscous stress, $\overline{\tau_\nu} = \nu\,\mathrm{d}\overline{u}/\mathrm{d}y$, and the turbulent stress, $\overline{\tau_T} = -\overline{u'v'}$, and summing them therefore yields an analytically verifiable metric for stationarity. The profiles in figure 3.2 confirm this balance, indicating that the flow is fully developed and the sampling window is sufficient. Here, as with all profiles presented in this work, unless explicitly plotted over the entire channel, quantities are plane- and time-averaged and further averaged across the symmetry plane at the channel center. The viscous stress peaks at the wall, where $\overline{\tau_\nu}(y = 0) = \tau_w$, and decays rapidly away from it, reaching zero at the channel center where the streamwise velocity profile is maximal, as expected. The turbulent stress vanishes at the wall, exhibits a peak at intermediate y, and likewise decays to zero at the channel center. The total stress, $\overline{\tau} = \overline{\tau_\nu} + \overline{\tau_T}$, is a straight line equal to the wall shear stress at $y = 0$ and decaying to zero at the channel center, as required for fully developed channel flow.

The dimensions of the domain must also be large enough so that the largest turbulent structures are not artificially constrained by the periodic boundary conditions. This is assessed via the streamwise autocorrelation functions, R_{uu}, R_{vv}, and R_{ww}, of the velocity

fluctuations, shown in figure 3.2(b), defined for the streamwise fluctuation as

$$R_{uu}(r) = \overline{\overline{u'(x)\,u'(x+r)}} \,/\, \overline{\overline{u'^2}}, \tag{3.9}$$

where r denotes the streamwise separation. R_{vv} and R_{ww} defined analogously in terms of v' and w'. For a domain of sufficient size, the autocorrelations must decay to zero before the half-length of the domain, $\ell_x = L_x/2$, indicating that the largest turbulent structures are not correlated with their own periodic images. As shown in the figure, the spanwise and wall-normal functions decay to approximately zero within a fraction of the domain half-length, however the streamwise fluctuations only decay to $R_{uu} \approx 0.16$ suggesting that the domain length is insufficient to contain the largest turbulent scales. Fortunately, the effects of domain size on turbulent channel flow are well-studied with the present channel size sufficient to accurately capture one-point statistics for both single phase [114] and particle-laden [115] channel flows. The domain size is selected over practical considerations as the cohesive particle-laden simulations have long aggregation-dominated initial transients, presented in chapter 5. Furthermore, the present domain size matches a history of PR-DNS of turbulent channel flow [116, 117] making comparison straightforward.

To further verify the flow, the mean streamwise velocity profile, $\overline{u}^+$, and the velocity fluctuations, $\overline{u'u'}^+$, $\overline{v'v'}^+$, and $\overline{w'w'}^+$, from the single-phase precursor simulation (SP) are compared in figure 3.3 against the DNS of Lee & Moser [4] at $Re_\tau = 182.088$ (LM2015). Here, $\overline{\cdot}$ denotes a plane- and time-average, and a superscript + denotes a quantity made dimensionless with δ_ν and u_τ. The present precursor reaches $Re_\tau = 179.82$, in close agreement with LM2015, and the SP profiles show excellent overall agreement across the near-wall, buffer, and log-law regions. Small discrepancies are observed near $y^+ = 10$, likely due to the second-order accuracy of the present solver as opposed to the seventh-

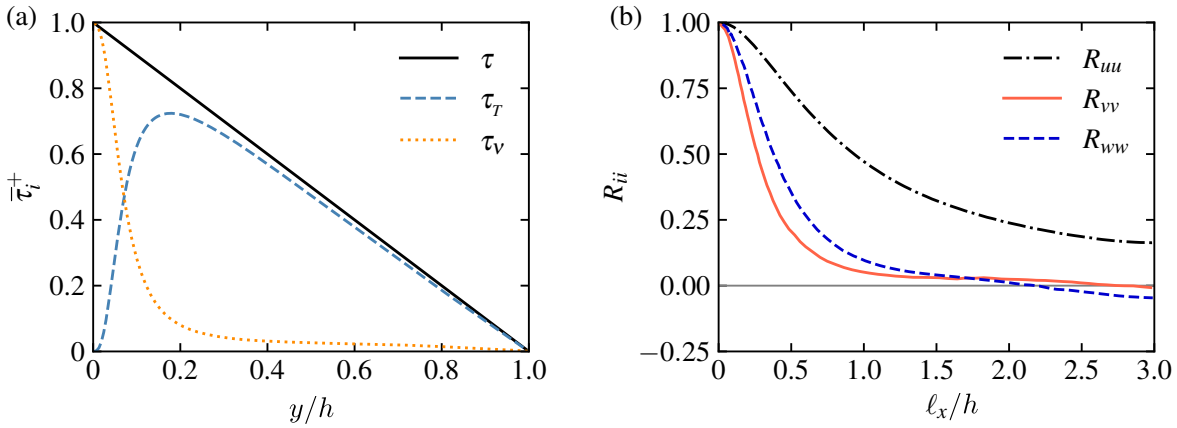


Figure 3.2: (a) Stress balance for the single-phase precursor flow, showing profiles of the viscous (τ_ν), turbulent (τ_T), and total (τ) stresses in inner units, over the wall-normal coordinate y, made dimensionless with the half channel height h. (b) Streamwise autocorrelation functions of the streamwise (R_{uu}), wall-normal (R_{vv}), and spanwise (R_{ww}) velocity fluctuations, where ℓ_x/h denotes the streamwise separation relative to the half channel height h. The horizontal gray line marks zero.

order method employed by Lee & Moser [4]. Furthermore, Co is kept low enough so that aggregates remain smaller than the half-channel height in any single spatial dimension, avoiding the formation of infinite chains of particles across the periodic directions and self-interacting wakes. We remark that, given the second-order accuracy of the IBM coupling in the particle-laden cases, the use of a higher-order solver does not yield meaningful benefit.

3.4 Non-cohesive particle-laden validation

Although no data exists that exactly matches the present configuration, we ensure that the non-cohesive case matches deviations from single-phase flow reported in parametrically nearby cases. Picano et al. [116] investigated turbulence modulation in suspensions of spherical particles of with diameter $2h/16$, density ratio $\rho_s = 1$, at volume fractions $\{0.05, 0.1, 0.2\}$. For 0.05 they report a reduction in streamwise fluctuations and

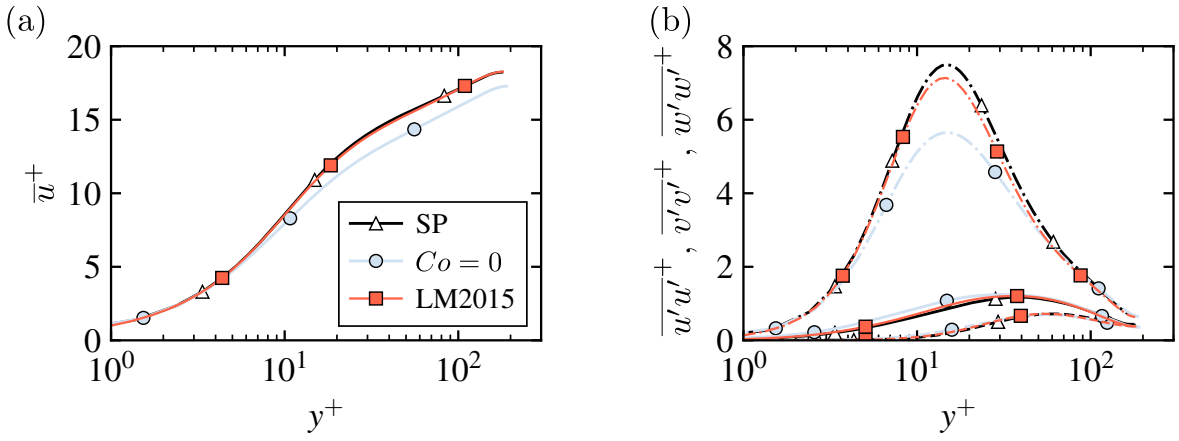


Figure 3.3: Comparison of (a) the mean streamwise fluid velocity, $\overline{u}^+$ and (b) velocity fluctuations, $\overline{u'u'}^+$; -·-·-, $\overline{v'v'}^+$; ——, and $\overline{w'w'}^+$; - - -, from the single-phase (SP) and non-cohesive ($Co = 0$) cases from this study, and the channel flow DNS of $Re_\tau = 182.088$ by Lee & Moser [4] (LM2015).

increase in wall-normal and spanwise fluctuations, as also seen here in figure 3.3. They also report a similar increase in Re_τ, which they attribute to the formation of a layer of particles at the wall that maintain increased slip velocities due to their finite size. This counteracts the expected decrease in Re_τ due to reduced turbulence activity. The measured $Re_\tau = 190.05$ for the $Co = 0$ case can also be compared to the scaling law of Costa et al. [118], which estimates a friction Reynolds number taking into account the particle layer at the wall. The error between the estimated friction Reynolds number from the scaling law, $Re_{\tau,e}$ and the present DNS is, $1 - Re_\tau/Re_{\tau,e} = 0.037$, which falls within the 4% confidence interval suggested in their work.

Chapter 4

The population balance equation[1]

4.1 Formalism

4.1.1 The aggregate number density

An aggregate of size n is defined as a cluster of n particles which are linked through a chain of neighbors separated by a surface distance less than λ, and thus subject to cohesive forces. The number of aggregates of size n, at location $\boldsymbol{x}$, at time t per unit volume is given by the aggregate number density,

$$f(n, \boldsymbol{x}, t) = \sum_{i=1}^{N_a(t)} \delta\left(\boldsymbol{x} - \boldsymbol{x}_i^A(t)\right) \delta\left(n - n_i(t)\right), \tag{4.1}$$

where $\boldsymbol{x}_i^A(t) = (x_i^A, y_i^A, z_i^A)$ and n_i are the center of mass and number of primary particles of aggregate i, $\delta(\cdot)$ is the Dirac delta function, and $N_a(t)$ is the total number of aggregates in the domain at time t. We take n as the phase-space variable since it is conserved along

[1]This chapter contains previously published work, adapted here with minor modifications from the following references: A. D. Leonelli, L. Widmer, and E. Meiburg, *Aggregation, breakup, and size-dependent transport in a turbulent channel flow with cohesive particles*, 2026. Under review at *J. Fluid Mech.* at the time of dissertation submission.

with the aggregate mass $m_i^A = n_i \rho_f V_p$, where $V_p = \pi d^3/6$ is the volume of a single primary particle (assuming a monodisperse primary particle distribution). Since n is a dimensionless integer, f carries units of (length)$^{-3}$.

In chapters 6 and 7, f is formulated in terms of the effective aggregate diameter $D = n^{1/3} d$, which is the diameter of a sphere with equal volume to the primary particles constituting an aggregate. With this substitution equation (4.1) reads

$$f(D, \boldsymbol{x}, t) = \sum_{i=1}^{N_a(t)} \delta\left(\boldsymbol{x} - \boldsymbol{x}_i^A(t)\right) \delta\left(D - D_i(t)\right), \tag{4.2}$$

which instead carries units of (length)$^{-4}$, with $f(n, \boldsymbol{x}, t)\,\mathrm{d}n = f(D, \boldsymbol{x}, t)\,\mathrm{d}D$. Equations (4.1) and (4.2) are therefore related by the Jacobian, $\mathrm{d}n/\mathrm{d}D = 3D^2/d^3$,

$$f(D, \boldsymbol{x}, t) = f(n, \boldsymbol{x}, t)\,\frac{3D^2}{d^3}. \tag{4.3}$$

The instantaneous number density f should not be evaluated pointwise, but rather only after integrating over a finite region, where it returns the aggregate count. Taking this integration over the full domain Ω and summing over all n therefore gives,

$$N_a(t) = \int_\Omega \sum_n f(n, \boldsymbol{x}, t)\,\mathrm{d}V, \tag{4.4}$$

or, in the case of equation (4.2),

$$N_a(t) = \int_\Omega \int f(D, \boldsymbol{x}, t)\,\mathrm{d}D\,\mathrm{d}V. \tag{4.5}$$

It is not until averaging that (4.1) yields a smooth, finite probability density. The remainder of this section is formulated for equation (4.1), with the understanding that an analogous formulation in terms of (4.2) follows straightforwardly by replacing sums over

n with integrals over D, as in equations 4.4 and 4.5.

Lastly, the total number of primary particles N can similarly be recovered by taking the first moment with respect to n of f,

$$N = \int_\Omega \sum_n n f(n, \boldsymbol{x}, t)\, dV \tag{4.6}$$

which is constant in time by conservation of mass,

$$\frac{\mathrm{d}N}{\mathrm{d}t} = 0. \tag{4.7}$$

4.1.2 The population balance equation

The evolution of f is described by the PBE, which in its most general form reads,

$$\frac{\partial (nf)}{\partial t} + \underbrace{\nabla \cdot (n \boldsymbol{u}_n f)}_{\boldsymbol{x}\text{-advection}} + \underbrace{\frac{\partial \left(n v_D f\right)}{\partial n}}_{n\text{-advection}} = \underbrace{A_+ + A_-}_{\text{aggregation}} + \underbrace{B_+ + B_-}_{\text{breakup}}, \tag{4.8}$$

where $\boldsymbol{u}_n(n, \boldsymbol{x}, t) = (u_n, v_n, w_n)$ is the mean velocity of aggregates of size n in physical space and the n weighting allows for explicit mass conservation. Similarly, $v_D(n, \boldsymbol{x}, t)$ describes the continuous growth or shrinkage of aggregates in size space. In this work, all aggregation and breakup events are discrete and assumed to be instantaneous so $v_D = \mathrm{d}n/\mathrm{d}t \equiv 0$. The right side collects source and sink terms $S_i \in \{A_+, A_-, B_+, B_-\}$ that capture these discrete aggregation and breakup events, which are assumed binary (two aggregating into one, or one fragmenting into two). Nonbinary events are rare and discussed in appendix B. For brevity, explicit dependence on $(\boldsymbol{x}, t)$ is omitted hereafter, and all PBE quantities are understood to carry it unless stated otherwise, e.g. $S_i(n) = S_i(n,\ \boldsymbol{x},\ t)$.

The aggregation source A_+ accounts for the formation of size-n aggregates by the

coalescence of smaller aggregates size m and $n-m$,

$$A_+(n) = \frac{n}{2}\sum_{m=1}^{n-1} f(m)\, f(n-m)\, \beta(m, n-m). \tag{4.9}$$

where $\beta(m, n-m)$ is the aggregation (or coalescence) frequency and the $1/2$ rectifies double-counting. In some PBE formulations, β is further partitioned into a product of the collision rate $\alpha_c(m, n-m)$ and aggregation efficiency $q_a(m, n-m)$, $\beta = \alpha_c q_a$; however, since all collisions are resolved in this work, a minimum aggregate lifetime would have to be selected to measure q_a, so it is instead assumed to be unity, $q_a = 1$. Therefore, β is equivalent to the collision kernel. Equation (4.9) is also often written as a double sum over aggregate pairs m_1 and m_2, where mass conservation, $n = m_1 + m_2$, is enforced by a delta function, $\delta(m_1 + m_2 - n)$.

The complementary aggregation sink A_- removes size-n aggregates lost to coalescence with any size-m partner,

$$A_-(n) = -n\, f(n) \sum_{m=1}^{\infty} f(m)\, \beta(n, m), \tag{4.10}$$

where the sum spans all sizes since any aggregation event involving the size-n class depletes it. The breakup source term B_+ gives the production of size-n fragments from the breakup of larger parent aggregates,

$$B_+(n) = n \sum_{m=n+1}^{\infty} f(m) g_b(m) q_b(m, n), \tag{4.11}$$

where $g_b(m)$ is the breakup rate of size-m parent aggregates and $q_b(m, n)$ is the fragment size distribution. Finally, the sink B_- captures the loss of size-n aggregates due to breakup,

$$B_-(n) = -n f(n) g_b(n). \tag{4.12}$$

4.1.3 Net transport

The net transport in and out of size n due to aggregation and breakup can be summarized as

$$T_a(n) = A_+(n) + A_-(n), \tag{4.13}$$

and

$$T_b(n) = B_+(n) + B_-(n), \tag{4.14}$$

respectively. With this formulation, $T_a(n) > 0$ indicates that more aggregate mass is being brought into size n by aggregation of smaller aggregates than is being removed by further aggregation into larger sizes, with the converse holding for $T_a(n) < 0$. Similarly, $T_b(n) > 0$ indicates that more size-n aggregates are being generated by the breakup of larger aggregates than are removed by further breakup into smaller sizes, with the converse holding for $T_b(n) < 0$. Note that the direction of the mass flux through n space is opposite in sign for $T_a(n) > 0$ and $T_b(n) > 0$ with the former indicating an upscale transfer of mass and the latter a downscale flux. Since aggregation and breakup do not create or destroy aggregate mass, but rather redistribute it across size-space, $T_a(n)$ and $T_b(n)$ must each satisfy

$$\sum_n T_a(n) = \sum_n T_b(n) = 0. \tag{4.15}$$

With these discussions summarized in figure 4.1.

4.2 PBE averaging procedures and assumptions

4.2.1 Plane-and-time averaging

For channel flow, f is statistically homogeneous in the periodic streamwise and spanwise directions, reducing the spatial dependence of its average over x and z to the wall-

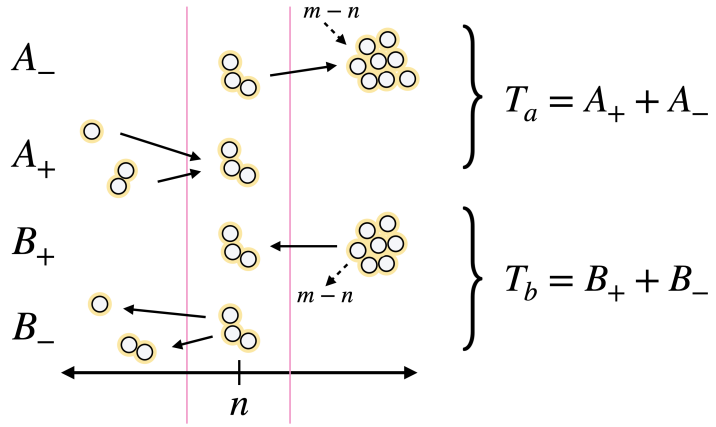


Figure 4.1: Schematic depicting the roles of the aggregation and breakup source and sink terms in equation (4.8). The horizontal axis shows the space of aggregate sizes with an arbitrary class n partitioned by two gray horizontal lines on either side. Arrows representing aggregation and breakup events point from parent to child aggregate(s) and enter/exit the size n partition.

normal coordinate y alone. Time averaging over the statistically stationary period T then yields the plane-and-time averaged number density, $\overline{f}(n, y)$. Applying the plane-and-time averaging operation to equation (4.8) yields the plane-and-time averaged PBE,

$$\frac{\partial}{\partial y}\left[\overline{nv_n f}\right](n, y) = \overline{A_+}(n, y) + \overline{A_-}(n, y) + \overline{B_+}(n, y) + \overline{B_-}(n, y). \tag{4.16}$$

Notably, the advective term permits the $\overline{S_i}$ to be locally imbalanced in y, allowing for spatially inhomogeneous net aggregation and breakup during equilibrium, a key insight that will be discussed later in chapter 7.

Equation (4.16) is expressed in terms of the individual, time- and spatially-varying kernels, β, g_b, and q_b. Importantly, the rate-describing terms, g_b and β, are not observable, since they represent the propensity of an aggregate to break or coalesce with a partner, rather than a countable quantity. They must instead be inferred from breakup and aggregation events accumulated over the sampling period, which raises discussion on what such inference can and can not recover under plane-and-time averaging.

Taking the simplest case of the plane-and-time averaged sink due to breakup, $\overline{B_-}$, and decomposing f and g_b into mean and fluctuating components, $f = \overline{f} + f'$ and $g_b = \overline{g_b} + g_b'$ the average sink term reads

$$\overline{B}_-(n,y) = -n\overline{f g_b}(n,y) = -n\overline{f}(n,y)\overline{g_b}(n,y) - n\overline{f' g_b'}(n,y), \tag{4.17}$$

where the cross correlation $\overline{f' g_b'}$ captures any statistical dependence between the local aggregate population and the local breakup rate, at fixed n and y. Importantly, when trying to infer the breakup rate,

$$\overline{g_b} = \frac{\overline{f g_b}}{\overline{f}} - \frac{\overline{f' g_b'}}{\overline{f}}. \tag{4.18}$$

Since g_b is never directly observable, $\overline{f' g_b'}$ can not be evaluated and $\overline{g_b}$ can not be strictly recovered from the averaged source and sink terms alone. It is nonetheless instructive to report the estimator,

$$\overset{\circ}{\overline{g_b}} = \frac{\overline{f g_b}}{\overline{f}}, \tag{4.19}$$

where the ring denotes and estimated, rather than exact, mean quantity. The breakup sink can then be rewritten in the same form as it appears in PBE models,

$$\overline{B_-}(n,y) = \overline{f}(n,y)\overset{\circ}{\overline{g_b}}(n,y) \tag{4.20}$$

Specifically for the breakup rate, the following assumptions argue that it is likely close to the true mean:

1. Due to the low volume fraction of primary particles, breakup is governed either by hydrodynamic stresses acting on an individual aggregate or by direct collision with the channel walls, rather than by interaction with, or the local concentration of,

neighboring aggregates.

2. Since $\overline{f}(n,y)$ and $\overline{g_b}(n,y)$ are themselves functions of y, any systematic wall-normal trend shared by the aggregate population and the breakup rate, for instance both increasing toward the wall, is captured directly by these mean profiles rather than by the fluctuations f' and g_b'. A residual correlation between f' and g_b' at fixed y would therefore require a mechanism operating within a wall-normal plane, for which no clear candidate is evident.

The same argument can be made for the breakup source,

$$\begin{aligned}\overline{B_+}(n,y) &= n\sum_{m=n+1}^{\infty}\overline{f(m,\mathbf{x},t)g_b(m,\mathbf{x},t)q_b(m,n,\mathbf{x},t)} \\ &\approx n\sum_{m=n+1}^{\infty}\overline{f}(m,y)\overline{\mathring{g}_b}(m,y)\overline{q_b}(m,n,y),\end{aligned} \tag{4.21}$$

where unlike g_b, q_b can be directly measured by tracking aggregate size across breakup and coalescence events.

Aggregation events pose a challenge since, unlike breakup, it requires two bodies to interact, and so the aggregation kernel $\beta(m,n-m)$ is directly dependent on the concentrations of size m and $n-m$ aggregates. Decomposing the aggregation sink,

$$\begin{aligned}\overline{A_-}(n,y) = -n\sum_{m=1}^{\infty}\Big[&\overline{f}(n,y)\overline{f}(m,y)\overline{\beta}(n,m,y) \\ &+\overline{f}(n,y)\,\overline{f'(m)\beta'(n,m)}+\overline{f}(m,y)\,\overline{f'(n)\beta'(n,m)} \\ &+\overline{\beta}(n,m,y)\,\overline{f'(n)f'(m)}+\overline{f'(n)f'(m)\beta'(n,m)}\Big].\end{aligned} \tag{4.22}$$

where clearly $f'(n)$ and $f'(m)$ are correlated since they can directly exchange mass

through aggregation and breakup events. So while an estimator,

$$\overline{\mathring{\beta}}(m, n-m, y) = \frac{\overline{f(m)f(n-m)\beta(m, n-m, y)}}{\overline{f(n)f(m)}} \tag{4.23}$$

can be computed, it remains confounded by these correlations. Such estimators are nonetheless commonly reported in the literature, and are reported here as well for the sake of comparison — with the caveat, not always made explicit elsewhere, that they should not be interpreted as unbiased measurements of the underlying kernel.

4.2.2 Volume-and-time averaged PBE

Integrating $\overline{f}(n, y)$ over the channel height yields the volume-and-time averaged number density, $\overline{\overline{f}}(n)$. Applied to (4.8), and enforcing that aggregates can not travel through the boundaries eliminates the advective term, leaving the volume-and-time averaged (or bulk-averaged) PBE,

$$0 = \overline{\overline{A_+}}(n) + \overline{\overline{A_-}}(n) + \overline{\overline{B_+}}(n) + \overline{\overline{B_-}}(n), \tag{4.24}$$

stating that aggregation and breakup must balance over the entire domain at every n.

4.3 Aggregate identification

Aggregates are identified at each stored snapshot by constructing an adjacency matrix over the particle population, in which entry (i, j) indicates whether particles i and j are adjacent. Two particles are considered adjacent if their surface-to-surface distance does

not exceed the cohesive force range λ,

$$\|\boldsymbol{x}_i^P - \boldsymbol{x}_j^P\| \leq r_i + r_j + \lambda, \tag{4.25}$$

where r_i and r_j are the particle radii. An aggregate is then defined as a maximal set of particles that are mutually reachable through chains of pairwise adjacency: that is, for any two particles in the set, the adjacency matrix admits a path of adjacent pairs connecting them.

The adjacency graph is constructed using a k-d tree [119, 120], which recursively partitions the particle population so that the detection of neighbors can be resolved in $O(\log N)$ operations across nearby partitions rather than by an exhaustive $O(N)$ search over all other particles. Querying the k-d tree for all N particles therefore yields all adjacent pairs in $O(N \log N)$ operations, as opposed to the $O(N^2)$ pairwise evaluation of Euclidean distance over the full particle set. This efficiency becomes significant given the domain contains several thousand particles per snapshot, and aggregates must be evaluated over tens of thousands of snapshots. Care is taken to account for aggregates that span over the periodic boundaries by creating image particles before building the k-d tree for that snapshot.

Given the resulting adjacency lists, connected groups are identified using an iterative depth-first search starting from an arbitrary particle then moving on to its neighbors, and their neighbors in turn. At each step the particle ids are added to the current group until no further unvisited neighbors remain, at which point the group constitutes one aggregate and the search proceeds from the next unvisited particle. This process is repeated until every particle has been assigned to an aggregate, yielding the aggregate size n_i, aggregate identity (ID), and ID of each constituent particle, which are used next to construct the aggregate family tree.

4.4 Family tree construction and event classification

Since aggregate identification (section 4.3) is performed independently at each snapshot, the aggregate ID assigned to a given cluster of particles is arbitrary and bears no relationship to the ID assigned to the same cluster, or its descendants, at any other snapshot. A contiguous identity must therefore be reconstructed *a posteriori*, by tracking particle-aggregate membership between each pair of consecutive snapshots, t and $t + \Delta t$.

Let aggregate j at time t be comprised of the primary particle set $\mathcal{A}_j$, and aggregate k at time $t + \Delta t$ be comprised of the primary particle set $\mathcal{A}_k$. The set of *child* aggregates of j,

$$\mathcal{C}_j = \{m : \mathcal{A}_j \cap \mathcal{A}_m \neq \emptyset\}, \tag{4.26}$$

collects every aggregate m at $t + \Delta t$ that shares at least one particle with j. Conversely, the set of *parent* aggregates of k,

$$\mathcal{P}_k = \{l : \mathcal{A}_l \cap \mathcal{A}_k \neq \emptyset\}, \tag{4.27}$$

collects every aggregate l at t that shares at least one particle with k. Continuity is established between aggregate j and aggregate k when $\mathcal{C}_j = \{k\}$ and $\mathcal{P}_k = \{j\}$: that is, j has only one child, k, and k has only one parent, j. In this case, the same set of primary particles simply persists as one aggregate, is reassigned a single contiguous ID, and no event is recorded.

When j has more than one child, $|\mathcal{C}_j| > 1$, its constituent particles are distributed among two or more aggregates at $t + \Delta t$, constituting a breakup event; j is recorded as a parent of each aggregate in $\mathcal{C}_j$, and each of those aggregates as a child of j. Symmetrically, when k has more than one parent, $|\mathcal{P}_k| > 1$, aggregate k is recorded as a child of each aggregate in $\mathcal{P}_k$, constituting an aggregation event. Due to the discrete spacing of

snapshots, both conditions may occur together for the same pair, i.e. $|\mathcal{C}_j| > 1$ for some j and $|\mathcal{P}_k| > 1$ for some $k \in \mathcal{C}_j$, the constituent particles of two or more aggregates are intermingled among two or more resulting aggregates, constituting a polyadic event.

Furthermore, because primary particle dynamics are physically continuous, breakup always occurs in series up to the finite resolution, here set by the spacing between snapshots. We therefore further partition aggregation and breakup events as binary or non-binary according to the resulting sizes of $\mathcal{C}_j$ and $\mathcal{P}_k$. Due to the high temporal resolution of snapshots, polyadic and non-binary events are rare, constituting less than 1% of all events detected across all cases. In this work, only binary events are considered, and polyadic and non-binary events are treated as erroneous. The classification rules for each event follow below.

Four outcomes are possible when constructing continuity between t and $t + \Delta t$:

- **No change**: $\mathcal{C}_j = \{k\}$ and $\mathcal{P}_k = \{j\}$; the same set of primary particles persists as one aggregate.
- **Aggregation event**: $|\mathcal{P}_k| > 1$; an aggregate at $t + \Delta t$ is comprised of the particles of two (binary) or more (non-binary) aggregates from t.
- **Breakup event**: $|\mathcal{C}_j| > 1$; the primary particles, and only the primary particles, of a single aggregate at t constitute two (binary) or more (non-binary) aggregates at $t + \Delta t$.
- **Polyadic event**: $|\mathcal{C}_j| > 1$ and $|\mathcal{P}_k| > 1$ for some $k \in \mathcal{C}_j$; the primary particles of two or more aggregates at t are intermingled and comprise two or more aggregates at $t + \Delta t$.

A local segment of the family tree, spanning a small number of generations around a single aggregate of interest, is shown for case $Co = 0.48$ in figure 4.2, along with a

visualization of a breakup event from that segment.

4.5 Finite-sized particles

In this work, particles and aggregates are finite-sized, so the point-wise evaluation of equation (4.16) is not possible. Instead, the solid phase volume is partitioned in the wall-normal direction using a grid with spacing $\Delta y = d/2$ and cell centers $y_j = \Delta y(j + 1/2)$ for $j \in \{0, 1, \ldots, 2h/\Delta y - 1 = 61\}$. For a particle i centered at wall-normal coordinate $y_i^P(t)$, the portion of its volume lying within subdomain j is obtained by integrating the spherical volume between the two bounding planes $y_j \pm \Delta y/2$. In the frame centered on the particle,

$$\mathcal{V}_i(y_j, t) = \int_{y_{l,i}}^{y_{u,i}} \pi \left(\frac{d^2}{4} - y^2 \right) \mathrm{d}y = \pi \left(\frac{d^2}{4}(y_{u,i} - y_{l,i}) - \frac{y_{u,i}^3 - y_{l,i}^3}{3} \right), \tag{4.28}$$

where

$$y_{u,i} = \min(y_j - y_i^P(t) + \Delta y/2, \quad d/2), \tag{4.29}$$

$$y_{l,i} = \max(y_j - y_i^P(t) - \Delta y/2, \; -d/2) \tag{4.30}$$

are the subdomain bounds in the wall-normal direction expressed relative to the particle center. The total particle volume in bin j contributed by aggregates of size n is then

$$V(n, y_j, t) = \sum_{i \in \mathcal{A}_n(t)} \mathcal{V}_i(y_j, t), \tag{4.31}$$

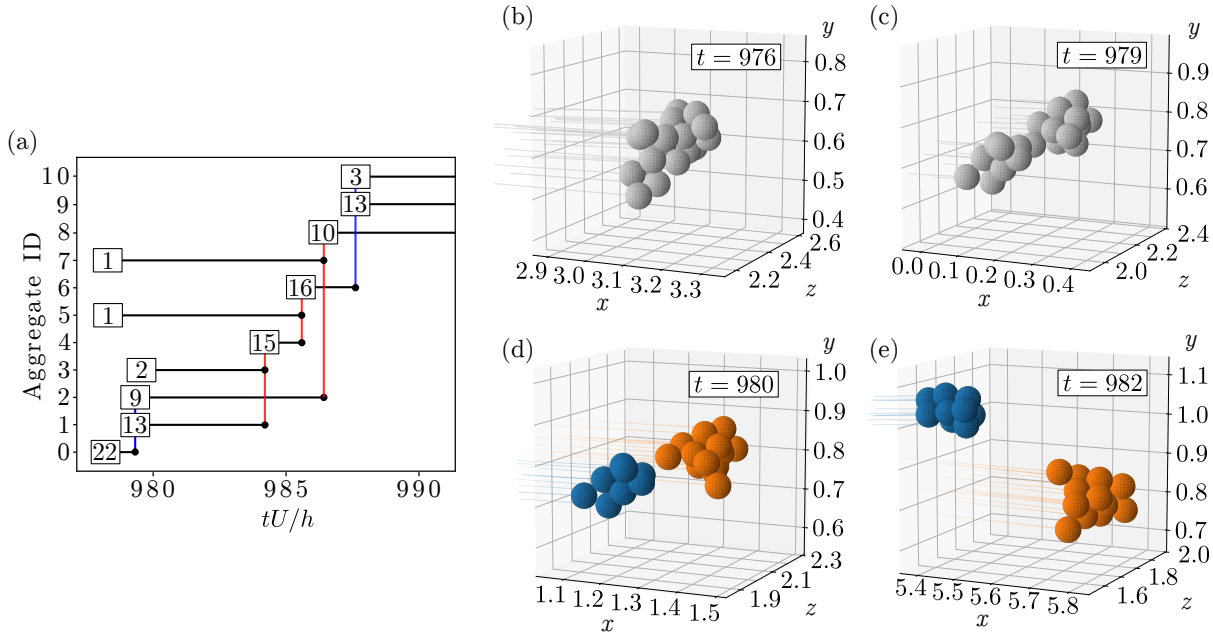


Figure 4.2: (a) A local segment of the family tree from case $Co = 0.48$, centered on a single aggregate of interest, here assigned aggregate ID 0. The vertical axis shows aggregate ID; the horizontal axis reports elapsed simulation time. An aggregate's time of birth is marked by a box inscribed with the number of primary particles it contains, and a black horizontal line spans its lifetime, terminating in a black dot marking its time of death. Vertical lines connect the time of death of a parent aggregate to the time of birth of its child or children. A red vertical line denotes an aggregation event, connecting the deaths of two parent aggregates to the birth of the resulting aggregation product. A blue vertical line denotes a breakup event, originating from the single black dot marking the parent aggregate's death and connecting to two boxes marking the birth of the resulting child aggregates, each inscribed with its size. Panels (b–e) show snapshots of aggregate 0 and its children, aggregates 1 and 2, corresponding to the segment of the family tree in panel (a). Before breakup (panels (b) and (c)), primary particles are colored gray; after breakup, aggregate 1 is colored orange and aggregate 2 is colored blue. Trailing lines show the preceding $0.2h/U$ time units of each particle's trajectory. Panels (b–e) are centered on the center of mass of the aggregate or aggregate pair; since aggregates travel across the periodic boundary in the streamwise direction, the x-position shown may decrease between sequential panels.

where $\mathcal{A}_n(t)$ is the set of primary particles belonging to aggregates of size n. The discrete, plane-averaged number density follows directly as

$$\widetilde{f}(n, y_j, t) = \frac{V(n, y_j, t)}{V_p V_y}, \tag{4.32}$$

where $V_y = L_x L_z \Delta y$ and $\widetilde{\cdot}$. Averaging (4.32) over the sampling window yields $\overline{f}(n, y_j)$, the discrete analog of the number density in (4.16).

Aggregation and breakup events are distributed across the wall-normal direction using the same weighting. The primary particles comprising the parent aggregate (for breakup) or the child aggregate (for aggregation) are located at the moment of the event and their volume is spread across the wall-normal bins using equation (4.28). This ensures $\overline{A_\pm}(n, y)$ and $\overline{B_\pm}(n, y)$ carry the same finite-size treatment as $\overline{f}(n, y)$.

The volume-averaged number density, $\widetilde{\widetilde{f}}(n, t)$, requires no distribution step, since it does not have spatial dependence and only requires counting the number of size-n aggregates,

$$\widetilde{\widetilde{f}}(n, t) = \frac{1}{L_x L_y L_z} \sum_{i=1}^{N_a(t)} \delta(n - n_i(t)). \tag{4.33}$$

4.6 Summary

This chapter presents a toolbox for the computation of population balance equation statistics in cohesive particle laden flow simulations. Aggregate identification is achieved by constructing a k-d so that cluster identification scales as $O(N \log N)$, enabling the identification of aggregates over large numbers of particles, or in this case a large number of samples. The aggregate number density is readily computed from the identified aggregates, however aggregation and breakup require continuity to be established between snapshots. To this end aggregation and breakup events are identified according to the

rules presented in section 4.4 which are briefly summarized below for the constituents of some aggregate identified at time t:

- **Aggregation:** The constituents are joined by new particles at $t + \Delta t$ that composed one (binary) or more (nonbinary) aggregates at t.

- **Breakup:** The constituents exclusively compose two (binary) or more (nonbinary) aggregates at $t + \Delta t$.

- **Polyadic:** The constituents compose multiple aggregates and are joined by other particles at $t + \Delta t$.

In this work, only binary events are considered, while nonbinary and polyadic events, which constitute less than 1% of events for all cases, are considered erroneous. The main thrust of this work is to evaluate the PBE kernels in the wall-normal direction. To this end a plane-and-time averaged PBE formulation is introduced in section 4.2.1 wherein aggregation and breakup may be balanced by a wall-normal advective flux of aggregates. Importantly, it is also shown that aggregation and breakup rates can not be directly evaluated due to cross correlations between the aggregate number density and the rates. This is shown to be especially problematic for the coalescence kernel that is dependent on collision rates between aggregate pairs. Finally, due to the finite size of the particles and aggregates, a coarse-graining procedure is applied to evaluate the PBE kernels resolved in the wall-normal direction. Rather than assign a breakup event to a single wall-normal location based on the aggregate center the aggregate mass is proportionally spread over the bins so that mass is transferred locally in the wall-normal direction across the size phase space variable.

Chapter 5

Aggregate growth and transient statistics[1]

The focus of this chapter is to characterize the rate of aggregate growth and its wall-normal dependence during the transient before the aggregate population equilibrates. Here, we are motivated by single-class flocculation models that track the rate of change of a characteristic scale such as the mean aggregate diameter. The foundational model proposed by Winterwerp [5] predicts the evolution of the mean aggregate diameter, here denoted with the placeholder symbol D_e,

$$\frac{\mathrm{d}D_e}{\mathrm{d}t} = \frac{k_A}{n_f}\frac{d^{n_f-3}}{\rho_p} G D_e^{4-n_f} - \frac{k_B}{n_f}\left(\frac{D_e - d}{d}\right)^{p_W} G^{q_W+1} D_e^{2q_W+1}, \tag{5.1}$$

where G is the turbulent shear rate, ρ_p and d are the primary particle density and diameter, n_f is the fractal dimension, which serves as a measure of compactness and

[1]This chapter contains previously published work, adapted here with minor modifications from the following references: A. Leonelli and E. Meiburg, *On the effects of anisotropy on the flocculation of cohesive particles in turbulence*, *Acta Mech.* 237 (2026), no. 4, 1699–1713. & A. D. Leonelli, L. Widmer, and E. Meiburg, *Aggregation, breakup, and size-dependent transport in a turbulent channel flow with cohesive particles*, 2026. Under review at *J. Fluid Mech.* at the time of dissertation submission.

is discussed further in section 5.2, and p_W and q_W are empirical exponents governing the strength- and shear-rate dependence of the breakup term. The model employs two fitting parameters, k_A (units (mass$\cdot$length^{-3})) and k_B (units (length$^{-2q_W}\cdot$time^{q_W})), which weight the first and second terms, accounting for aggregation and breakup, respectively. Note that some parameters present in the original formulation such as the sediment concentration and aggregate yield-strength have been absorbed into k_A and k_B, since the parameter space considered in this study is limited to one volume fraction, uniform population of primary particles, and a single fluid of constant properties. As with the multi-class PBE model developed in chapter 4, this model relies on closure parameters, here k_A and k_B, to describe the rate of change of aggregate size, and parameterizing these or similar constants has motivated a large body of experimental and numerical work [121, 122, 46, 48, 43, 123, 47, 124, 40].

Directly measuring aggregation and breakup rates experimentally requires substantial investment in high-speed imaging and well-controlled environments which are often prohibitive; Hoffman & Eaton [72] remain a notable exception, reporting collision, aggregation, and breakup rates for glass particles suspended in a humid turbulent flow. Numerically, Zhao et al. [40] directly measured $\mathrm{d}D_e/\mathrm{d}t$ in HIT and reported its dependence on cohesive strength, particle Stokes number, and shear rate. As surveyed in chapter 1, comparatively few studies address flocculation in wall-bounded flows, and, to the best of the authors' knowledge, none quantify the timescales of aggregate growth or the effect of an anisotropic shear rate on the growth rate directly. To this end, this chapter first characterizes the relaxation of the global aggregate population in section 5.3 before exploring the role of the wall-normal coordinate and variation in shear rate in section 5.4. Before this, however, several metrics for characterizing aggregate size and shape are introduced in section 5.2 next.

5.1 Transient and equilibrium identification

Simulations first advance through a period of net aggregate growth before reaching the statistically stationary state analyzed in chapters 6 and 7. The evolution of the total number of aggregates, $N_a(t)$, over time is shown in figure 5.1(a) for all Co cases. Given the initial random dispersal of primary particles, the aggregate count equals the primary particle count at release, $N_a(t=0) = N$. For $Co > 0$, N_a decreases as larger aggregates form; we refer to this aggregation-dominated transient as the *growth period*. Eventually aggregation and breakup balance, and the system enters the *equilibrium period*, in which statistics such as N_a fluctuate about a statistically steady value. The number of aggregates of sizes $n = \{1, 2, 3\}$ and $n > 3$ are shown for case $Co = 0.48$ in figure 5.1(b). The $n = 2$ class is first to rise before falling as the formation of larger aggregates depletes it; the $n = 3$ class follows a similar, more delayed response, and larger classes form with further delay still, seeded by the initial $n = 2$ and $n = 3$ aggregates. Correspondingly, the $n = 1$ class decays as the primary particle population redistributes into larger aggregates.

Similar to previously studied cases of sub-Kolmogorov scale particles suspended in HIT [40] and channel flow [36], this relaxation is well-captured by the exponential fit

$$N_a(t) = (N - N_{eq})\, e^{-bt} + N_{eq}, \tag{5.2}$$

where the equilibrium number of aggregates, N_{eq}, and the integral-scale growth rate, b, are fitting parameters. Similar bulk relaxation has been observed in simplified cellular flow models and HIT [124, 40, 125, 126] and, although not always explicitly characterized, in turbulent channel flows [35, 36, 38, 85, 86]. As expected, higher cohesive strength results in lower N_{eq}, since larger aggregates deplete the smaller sizes. The relaxation and resultant fits are shown in figure 5.1.

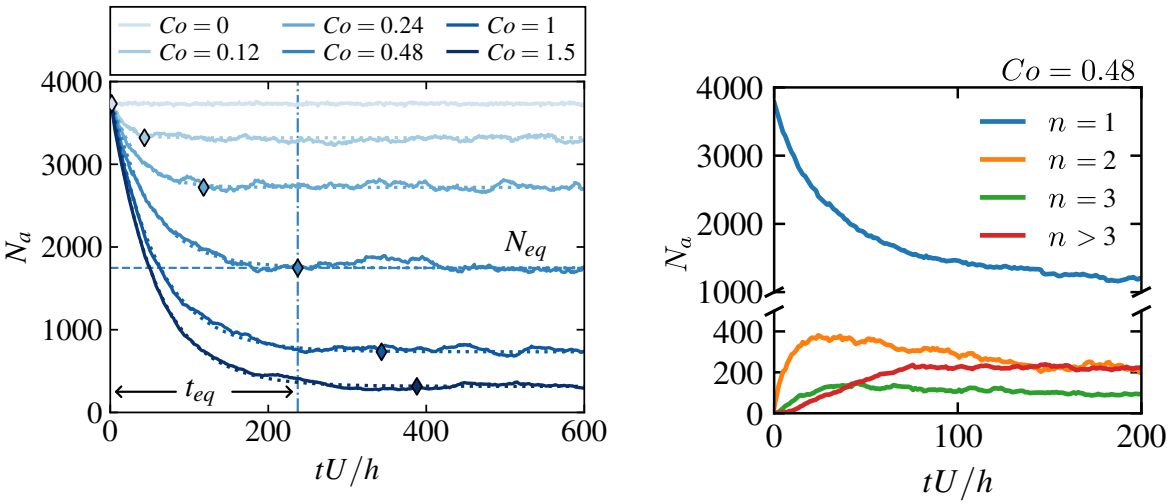


Figure 5.1: (a) Total number of aggregates N_a over time t for each Co. The exponential fit, equation (5.2), is shown as dashed lines. The light gray dash-dotted line shows the total number of primary particles $N = 3841$. The time to reach equilibrium t_{eq} is marked by diamonds and is additionally annotated for $Co = 0.48$ by a vertical dash-dotted line with the same color. N_{eq} is similarly annotated by a horizontal dashed line. (b) Number of aggregates of sizes $n = \{1, 2, 3\}$ and $n > 3$ over time for case $Co = 0.48$. The time periods displayed in both figures do not display the full runtime, which is reported in table 3.1. Furthermore, time t is made dimensionless with the mean streamwise velocity, U, and half channel height, h, in both panels.

This chapter is primarily concerned with the growth period and the relaxation towards equilibrium. To ensure the growth period is fully captured, we define the time to equilibrium, t_{eq}, as the time at which the fit of equation (5.2) decays to within 1% of N_{eq},

$$t_{eq} = -\frac{1}{b} \ln \left(\frac{0.01}{N/N_{eq} - 1} \right), \tag{5.3}$$

with the equilibrium period defined as $T_{eq} = [t_{eq}, t_{end}]$, where t_{end} is the final snapshot. The resultant t_{eq} for each case are reported in table 3.1 and appear as diamond markers in figure 5.1(a).

5.2 Aggregate size and shape

Equation (5.1) models the evolution of some characteristic aggregate size D_e. The size, shape, and compactness of aggregates are critical characteristics targeted for modeling, given their direct influence on aggregate dispersion, coalescence, breakup, and settling. Already in use is the number of constituent primary particles n. Perhaps just as straightforward is the diameter of a sphere with equivalent volume, $D = n^{1/3}$ which will be heavily employed later in chapters 6 and 7. Spatial extent can be estimated using the Feret diameter,

$$D_F = 2 \max \left\| \boldsymbol{x}_i^P - \boldsymbol{x}_j^A \right\| + d, \quad 1 \leq i \leq n, \tag{5.4}$$

which prescribes a spatial scale to the aggregate by taking the maximum distance between the center of a constituent particle, $\boldsymbol{x}_i^P$, and the aggregate center of mass, $\boldsymbol{x}_j^A$. Note that D_F is distinct from the volume-equivalent diameter, $D = n^{1/3}d$, introduced in chapter 4: D depends only on n, while D_F additionally reflects the aggregate's spatial extent and shape. In complement, the diameter of gyration, D_g, provides information on the aggregate shape and mass distribution,

$$D_g = \begin{cases} 2\sqrt{\dfrac{1}{n}\sum_{i=0}^{n} \left\| \boldsymbol{x}_i^P - \boldsymbol{x}_j^A \right\|^2}, & n > 2, \\ \sqrt{1.6}\, d, & n = 2, \\ d, & n = 1. \end{cases} \tag{5.5}$$

While insightful, D_F and D_g are not unique: an elongated aggregate of few particles can share the same D_F or D_g as a compact, many-particle aggregate.

The fractal dimension, n_f, characterizes this notion of compactness through the re-

lation,

$$D_e = n^{1/n_f} d, \tag{5.6}$$

where D_e is used as a placeholder for some characteristic aggregate diameter. For elongated particles, the spatial scale and number of constituent particles increases nearly proportionally, so $n_f \to 1$, while for more compact, sphere-like, assemblies $n_f \to 3$. To determine n_f from the present dataset the mean Feret diameter for each size n aggregate identivied over the equilibrium period, $\overline{\overline{D_F(n)}}$ is plotted against n for all Co in figure 5.2. The fractal dimension is then computed as the fitting parameter for the power law,

$$\frac{D_F(n)}{d} = \left(\frac{n}{\chi}\right)^{1/n_f}, \qquad \text{for } n > 2, \tag{5.7}$$

where χ is a secondary fitting parameter termed the "fractal prefactor". The best fit of equation (5.7) pooling all $Co > 0$ cases, shown with a black line in figure 5.2, yields $\chi = 0.4$ and $n_f = 2.14$; with the data and fit appearing largely insensitive to Co, indicating that aggregate compactness is not strongly dependent on cohesive strength within the present parameter range. The measured $n_f = 2.14$ also lends confidence to the suggested $n_f = 2$ by Winterwerp for equation 5.1

5.3 Aggregate growth

The growth of aggregates is directly reflected in the evolution of the size metrics defined in section 5.2: as shown in figure 5.3 where the mean (a) Feret diameter, (b) gyration diameter, and equivalent sphere diameter are averaged over the domain and reported over time. Each effective size increases in a similar fashion, with the time series shortened relative to the full runtime to place the transient period in focus.

Writing $\hat{D} = D/d$ so that $\hat{D}(0) = 1$ corresponds to a single primary particle, the

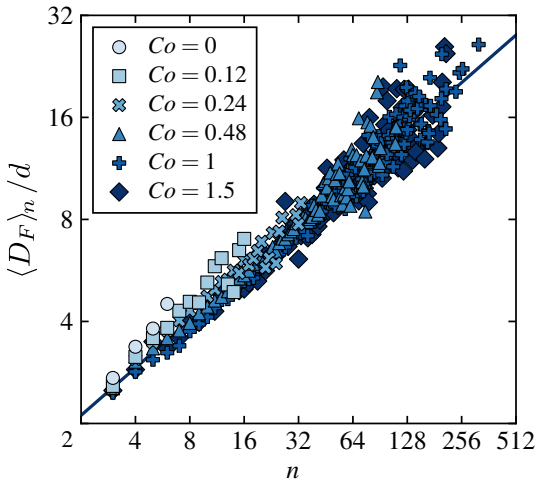


Figure 5.2: The mean Feret diameter, $\langle D_F \rangle_n$, for each aggregate population of n primary particles, plotted against n. The power law, equation (5.7), is fit to all data with $Co > 0$, yielding $\chi = 0.4$ and $n_f = 2.14$, shown as a black line.

Winterwerp model, equation (5.1), becomes

$$\frac{\mathrm{d}\hat{D}}{\mathrm{d}t} = K_1 \hat{D}^2 - K_2 \hat{D}^2 (\hat{D} - 1), \tag{5.8}$$

with $K_1 = dk_A \phi_0 \rho_p G$ and $K_2 = d^2 k_B G^{3/2}$ absorbing values that are constant between each Co case, i.e. the turbulent shear rate is assumed to not be greatly affected between runs.

Fitting K_1 and K_2 to the trajectories in figure 5.3 and plotting equation (5.8) as dashed lines shows reasonable agreement, though the rate of aggregate growth is initially under-predicted, then over-predicted upon approach to its equilibrium value, with the discrepancy most pronounced for the highest Co. The resultant K_1 and K_2 from each fit are plotted in figure 5.4 along with regressions across Co performed in log-log space to yield the power-laws reported in table 5.1. Notably, the parameter calibrating the aggregation rate, K_1, appears relatively independent of Co, while K_2, which mediates the breakup rate, is nearly inversely proportional to Co. This is physically reasonable

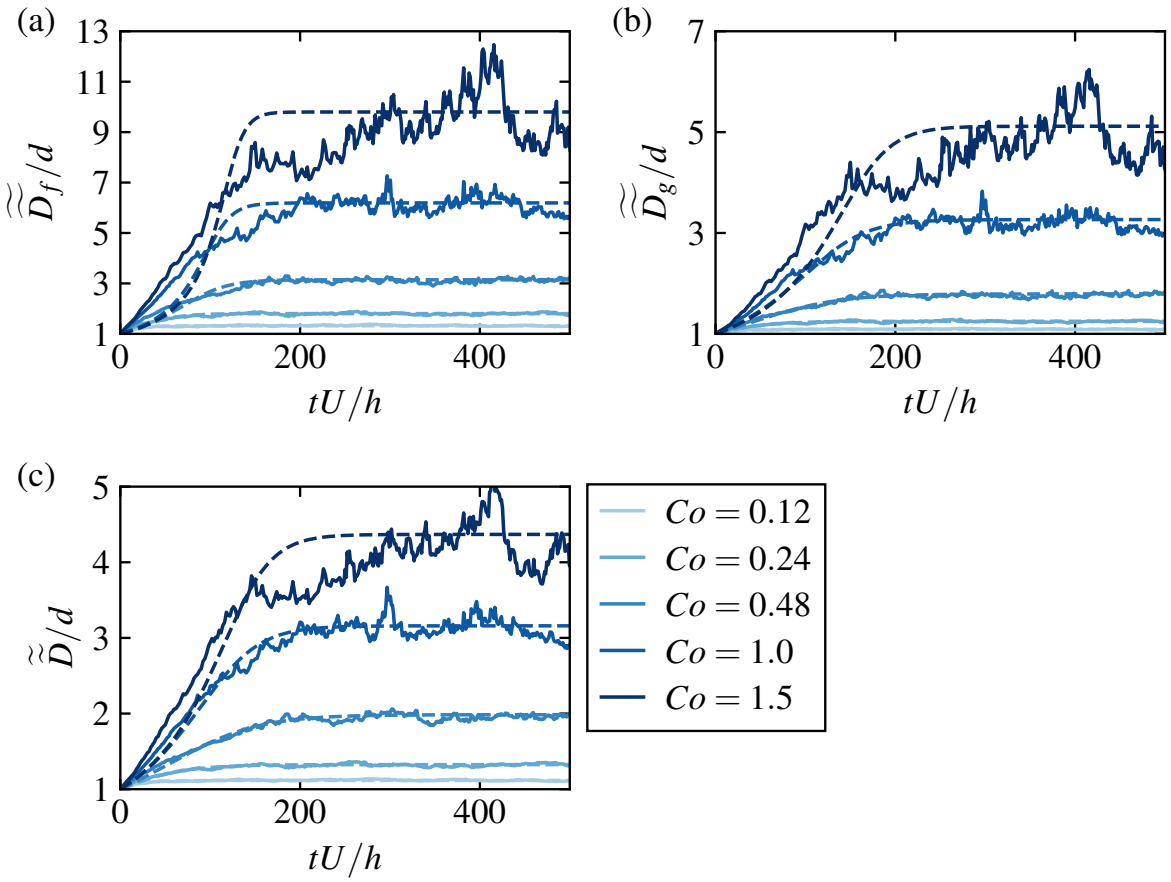


Figure 5.3: Evolution of mean aggregate size over time as evaluated by the (a) Feret diameter, $\widetilde{\widetilde{D_F}}/d$, (b) diameter of gyration, $\widetilde{\widetilde{D_g}}/d$, (c) diameter of a sphere of equivalent volume to the aggregate $\widetilde{\widetilde{D}}/d$. The fits from equation (5.8) are shown as dashed lines with fitting parameters reported in figure 5.4.

Metric	Power-law fit	Fig. 5.4 subfigure
D_F	$K_1 \propto Co^{-0.1622}$	(a)
D_g	$K_1 \propto Co^{0.1886}$	(b)
D	$K_1 \propto Co^{0.1812}$	(c)
D_F	$K_2 \propto Co^{-1.4739}$	(d)
D_g	$K_2 \propto Co^{-1.13365}$	(e)
D	$K_2 \propto Co^{-1.1571}$	(f)

Table 5.1: Power law fits of the variation of the model parameters K_1 and K_2 from the flocculation model, equation 5.8 with the cohesive number Co. The K_1 and K_2 for each characteristic diameter and the above fits are displayed in figure 5.4.

considering the rate of aggregation is more heavily mediated by collision rates, where the cohesive strength governs collision outcome, whereas the cohesive strength has a more direct influence on breakup. This is also encouraging, since K_2 encompasses the aggregate yield strength from the original Winterwerp model, which enters the full model with a suggested power of $F_y^{-0.5}$, though the relationship between the macroscopic notion of yield strength and the microscopic cohesive force mediated by Co is physically motivated but quantitatively unclear, and remains a topic of significant current research effort [127].

5.4 Wall-normal variation

In the previous section we considered the growth of aggregates to be uniform over the entire domain, however, the channel flow is highly anisotropic with both turbulent intensity and mean shear rate varying significantly with wall-normal distance. This is shown directly by partitioning the channel into 32 wall-normal subdomains, tracking $\widetilde{D_F}$, $\widetilde{D_g}$ and $\widetilde{D}$ within each (where a single tilde now denotes a plane-average), and fitting K_1 and K_2 to each trajectory yielding the per-bin $K_1(y)$ and $K_2(y)$. These steps are exemplified in figure 5.5 where (a) shows the growth of the mean Feret diameter within

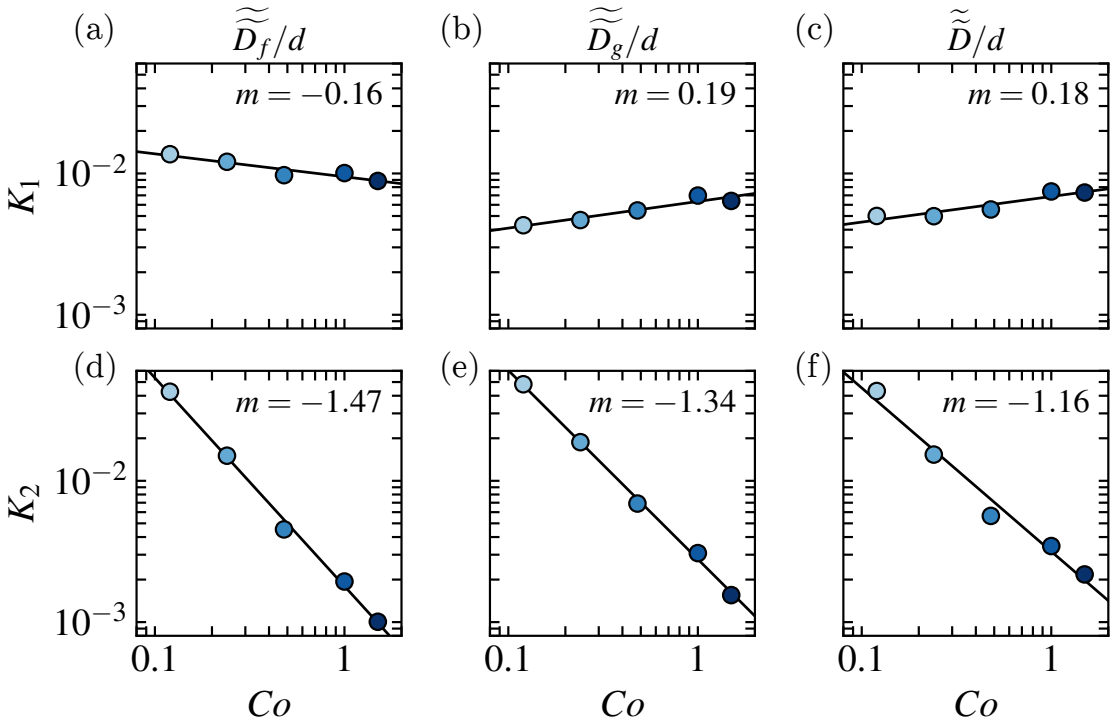


Figure 5.4: Power law dependencies of the fitting parameters K_1 and K_2 from the flocculation model, equation 5.8. Column titles indicate which spatial scale is used to define the aggregate diameter with D_F the Feret diameter, D_g the diameter of gyration, and D the sphere equivalent diameter. A solid line through the data points displays the result of a linear regression, with the slope m annotated. Detailed fit parameters are reported in table 5.1.

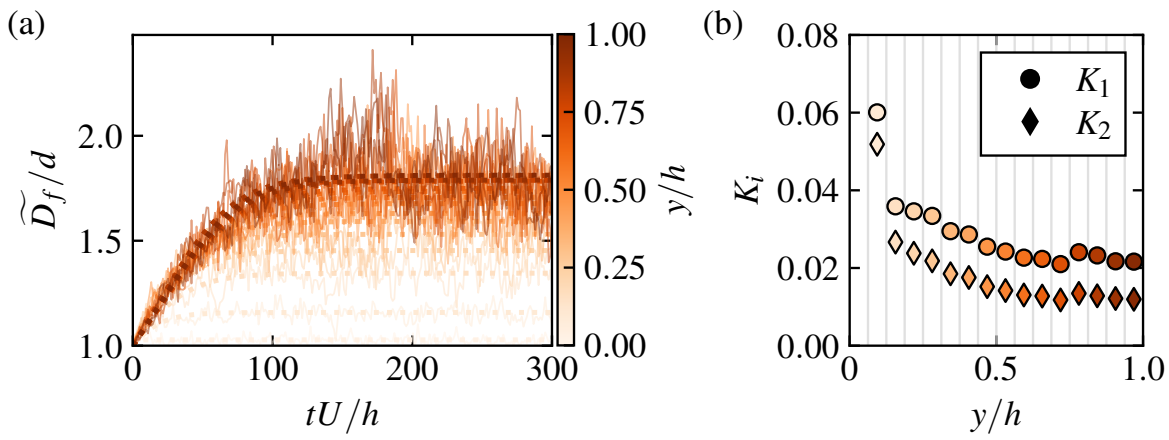


Figure 5.5: (a) Time evolution of the mean Feret diameter, $\widetilde{D_F}/d$, in 8 bins ($n_{bin} = 32$ averaged over the symmetry plane) in the wall-normal direction for case $Co = 0.48$. The wall-normal position of each bin is denoted by its color with the corresponding color bar ranging from the wall at $y/h = 0$ to the channel center at $y/h = 1$. The best fits of equation (5.8) for each bin are shown as dashed lines. (b) The fitted $K_1(y)$ (circles) and $K_2(y)$ (diamonds) plotted over the half channel height. The markers are filled to match (a) while the bins are demarcated by light gray vertical lines.

each wall-normal bin and (b) displays the resulting $K_1(y)$ and $K_2(y)$ for $Co = 0.48$.

Winterwerp's derivation of equation (5.1) predicts a specific shear-rate scaling for the two rate constants, $K_1 \propto G$ and $K_2 \propto G^{1.5}$. While originally derived for an isotropic shear rate, here we question if K_1 and K_2 similarly scale with the shear rate given its variation in the wall-normal direction $G(y)$ (c.f. figure 5.6). We take $G(y) = \sqrt{\varepsilon(y)/\nu}$, the local Kolmogorov shear rate computed from the dissipation ε, as the shear rate profile and interpolate it onto the same 16 half-channel bin centers used to fit $K_1(y)$ and $K_2(y)$. Rather than impose Winterwerp's predicted exponents outright, we regress the independently-fit $K_1(y_i)$, $K_2(y_i)$ against the local $G(y_i)$ in log-log space,

$$\log K_1(y_i) = p_1 \log G(y_i) + \log C_1, \tag{5.9}$$

$$\log K_2(y_i) = p_2 \log G(y_i) + \log C_2, \tag{5.10}$$

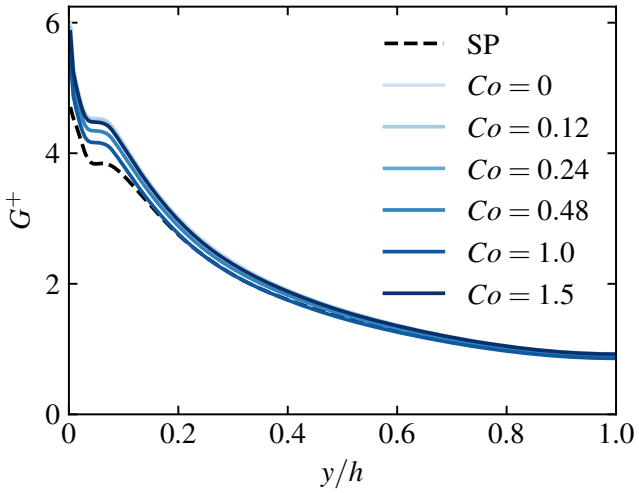


Figure 5.6: Wall-normal profile of the Kolmogorov shear rate $G = \sqrt{\varepsilon/\nu}$ in inner units for each Co and the single phase case SP. The mean profile is computed over the equilibrium period T_{eq} defined in chapter 6 and recorded in table 3.1.

taking the slopes p_1, p_2 as the empirical shear-rate exponents, with C_1, C_2 the corresponding prefactors. The resulting p_1 and p_2 are given as a function of Co in figure 5.7, where the original scaling predicted by Winterwerp [5], $p_1 = 1$ for the aggregation term (a) and $p_2 = 1.5$ for the breakup term (b), are shown as black horizontal lines. Satisfactorily, the fitted p_1 and p_2 indeed cluster around the predicted values. The choice of aggregate size metric (D_F, D_g, or D) does not significantly alter the recovered exponents, since the underlying K_1 and K_2 differ little between metrics (c.f. figure 5.4). This agreement suggests that the aggregation and breakup mechanism in the present channel flow are mediated by the local turbulent forcing which can be resolved here by the mean wall-normal Kolmogorov shear rate. This is potentially surprising considering the large size of the primary particle relative to the Kolmogorov scale ($d/\eta \approx 6.78$ near the wall at $y = 0.06h$, decreasing to $d/\eta \approx 3.15$ at the centerline on average) while the model of Winterwerp [5] was originally formulated for sub-Kolmogorov scale aggregates. Despite this, recent work in HIT demostrated the capability of such models to predict aggregate growth rates in HIT while also demonstrating that aggregates temporarily grow larger

than η. Despite this, a broader parametric study is undoubtedly required to further develop the wall-normal dependence of such flocculation models.

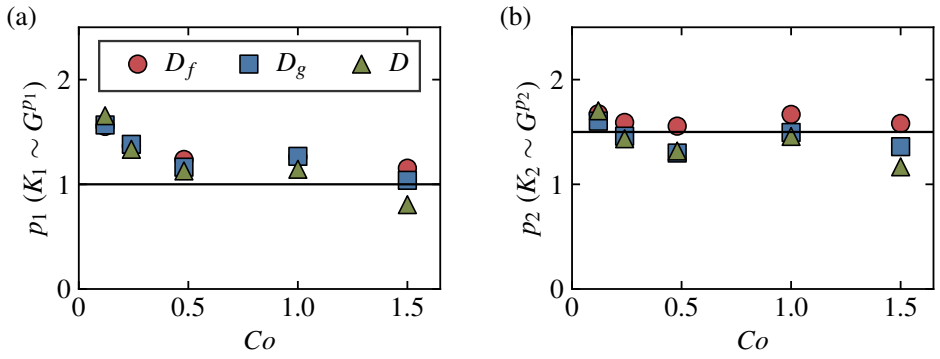


Figure 5.7: Empirically recovered shear-rate exponents p_1 (a) and p_2 (b), from regressing $K_1(y)$ and $K_2(y)$ in equation (5.8) against the local shear rate, plotted against the cohesive number Co for each aggregate size metric (D_F, D_g, D). Horizontal black lines mark the scaling predicted by Winterwerp [5]: $p_1 = 1$ for the aggregation term (a) and $p_2 = 1.5$ for the breakup term (b).

5.5 Summary

Once released, the cohesive particles coalesce, forming progressively larger aggregates. Accordingly, the total number of aggregates in the channel decreases. This relaxation is well-modeled by a first-order relaxation process, which is exploited in this work to partition the simulations into two periods: an initial aggregation-dominated transient, and a statistically stationary equilibrium in which aggregation and breakup globally balance. The single-class flocculation model of Winterwerp [5] describes the evolution of a characteristic aggregate diameter by a two-parameter model accounting for aggregation and breakup (equation 5.1). Here we define three characteristic diameters, the Feret diameter D_F, the gyration diameter D_g, and the equivalent sphere diameter D, and track their growth over time. Applying the Winterwerp model displays good agreement. Power laws for the scaling of the fit parameters K_1 and K_2 with the cohesive strength

are reported, notably only the breakup term K_2 systematically presents a scaling nearly proportional to Co. While the original Winterwerp model suggest a scaling with the yield stress of an aggregate as $K_2 \propto F_y^{-0.5}$ the present parameterization gives a scaling with the microscopic inter-particle force rather than the macroscopic bulk notion of yield stress. Finally, the channel is partitioned into bins in the wall-normal direction with an individual $K_1(y)$ and $K_2(y)$ computed for each bin. The variation of $K_1(y)$ and $K_2(y)$ with the wall-normal direction is shown to be well-captured by replacing the homogeneous isotropic Kolmogorov shear rate G in Winterwerp's model with the local shear rate $G(y)$, which varies strongly with the wall-normal direction. Ultimately, the scaling $K_1(y) \propto G(y)$ and $K_2(y) \propto G(y)^{1.5}$ matches Winterwerp's scaling with G, demonstrating the validity of similar expansions in more recently proposed flocculation models [53, 54].

Chapter 6

Equilibrium statistics[1]

Following the initial aggregation dominated transient discussed in chapter 5 aggregation and breakup balance globally and a statistically stationary equilibrium is reached. The methodology and definition for defining the onset of this stationary period was also defined in chapter 5. Here, we again present the evolution of the number of aggregates N_a over time in figure 6.1 to introduce an additional sampling period $T_{sub} = [t_{sub}, t_f]$ within which snapshots of the Lagrangian particle data are stored every $\Delta_{t_{IO,sub}} = 0.01h/U$ in order to resolve aggregation and breakup events. This occurs alongside the equilibrium period, T_{eq}, within which snapshots of the flow fields and Lagrangian particle data are stored every $\Delta_{t_{IO}} = 1.2h/U$. The starting times of the two periods t_{eq} for T_{eq} and t_{sub} for T_{sub} are demarcated as diamond and circular markers respectively in figure 6.1, where $N_a(t)$ is shown over the full run times of each Co case. The periods T_{sub} and T_{eq} are additionally annotated for the case $Co = 0.48$.

In this chapter we first evaluate the aggregate number density to build an under-

[1]This chapter contains previously published work, adapted here with minor modifications from the following references: A. D. Leonelli and Meiburg, E. (2026). *Turbulent Channel Flow with Cohesive Particles*, *Proceedings of the 14th International Symposium on Turbulence and Shear Flow Phenomena*. Heidelberg, Germany. & A. D. Leonelli, L. Widmer, and E. Meiburg, *Aggregation, breakup, and size-dependent transport in a turbulent channel flow with cohesive particles*, 2026. Under review at *J. Fluid Mech.* at the time of dissertation submission.

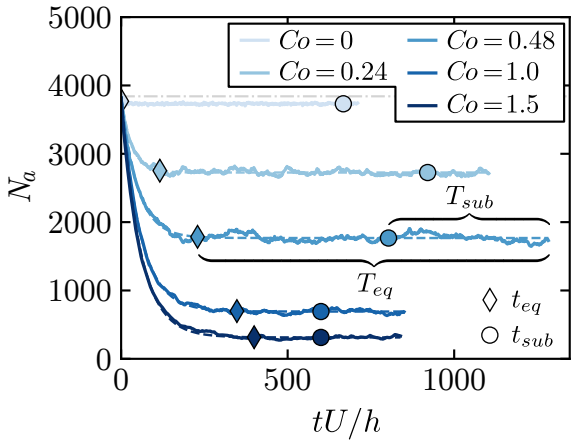


Figure 6.1: Number of aggregates N_a in the domain over time t made dimensionless with the mean streamwise velocity U and half channel height h. The full run times are displayed for each Co. The onset the equilibrium period, t_{eq} (equation 5.3), is shown with diamond markers while the beginning of the particle subsampling period is marked with circles. The two periods, T_{eq} and T_{sub}, equilibrium and subsampling respectively, are annotated for $Co = 0.48$. The exponential fits used to determine t_{eq}(equation 5.2 are shown as dashed lines while a gray dash-dotted line shows the total number of primary particles, $N = 3841$. Error bars denote a 95% confidence interval and are evaluated using the methodology described in appendix C.

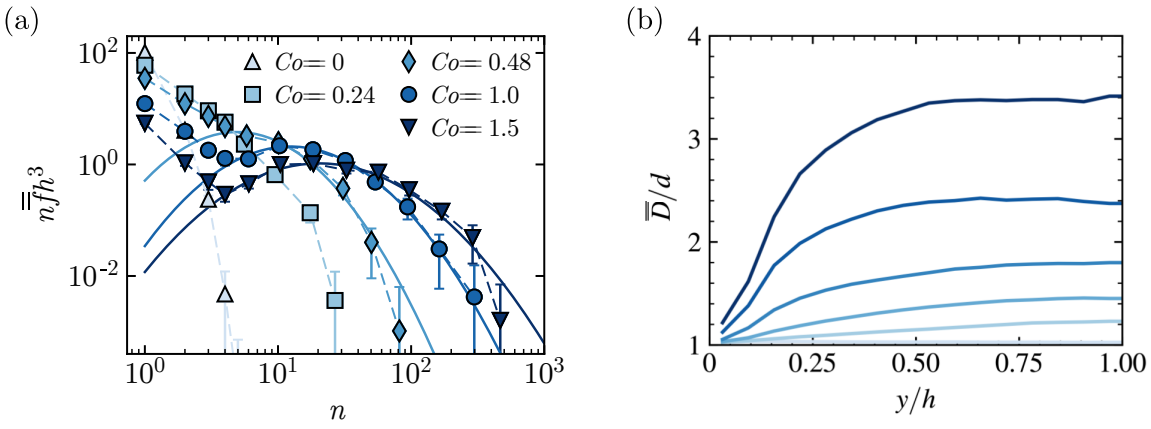


Figure 6.2: (a) Mass-weighted aggregate number density $\overline{\overline{nf}}$ as a function of size n for each cohesive strength Co (markers with dashed lines). Error bars denote 95% confidence intervals as defined in appendix C. Log-normal fits for $n > 3$ are shown as solid lines for $Co \geq 0.48$. (b) Plane-and-time averaged aggregate diameter $\overline{D}/d$ over the half channel for each Co.

standing of the spectrum of sizes that are dispersed in the flow in section 6.1. Due to their increased size, the aggregates present altered Eulerian flow statistics as reported in section 6.2. With altered size distributions and therefore dispersion, the aggregate feedback onto the flow becomes altered, though minimally as discussed in section 6.2 where the removal of a layer of particles adjacent to the wall is shown to result in a reduction of Re_τ towards the single phase value. Finally, aggregation and breakup are examined in the bulk, with their variation in the wall normal direction discussed in chapter 7.

Fluid statistics as well as the Eulerian particle flow statistics are evaluated over T_{eq} in the proceeding sections. In the final section 6.3, PBE kernels are presented which require the temporal fidelity of the subsampling period and are appropriately averaged over T_{sub}.

6.1 Aggregate number density

To build an understanding of the spectrum of sizes that are dispersed in the flow, the bulk mass-weighted aggregate number density, $\overline{\overline{nf}}$, is computed using 18 bins in

n, with four linearly spaced and the remainder logarithmically spaced to balance the discrete nature of small aggregates with sparse statistics at large n. Counts in each bin are normalized by the bin width so that $\overline{\overline{nf}}$ remains a density in n. Results are shown in figure 6.2(a).

Unsurprisingly, increasing Co yields larger aggregates. Reported functional forms for the aggregate size distribution vary with flow, material properties, and geometry. Power laws are commonly found in cohesion-dominated systems in HIT [90], with decaying exponentials also commonly reported in both HIT and startup channel flow [40, 36]. Experimental and field observations also report a spectrum of size distributions including log-normal [1]. Here, $n\overline{\overline{f}}$ is monotonically decreasing for $Co \leq 0.24$, while the distributions for $Co \geq 0.48$ develop an approximately log-normal region for $n > 3$. Log-normal fits for $Co \geq 0.48$, made neglecting sizes $n \leq 3$, are shown as solid lines in both the main figure and inset. These will be revisited in chapter 7, where the non-monotonic nature of $n\overline{\overline{f}}$ is shown to reflect the growth of an intermediate range of sizes where aggregation and breakup establish a statistical circulation of aggregate mass in size-space that excludes the smallest aggregate sizes.

The aggregate size is also distributed over the wall-normal direction. To compactly demonstrate this, the plane-and-time averaged aggregate diameter $\overline{D} = \overline{n^{1/3}d}$ is shown to vary over the wall-normal direction in figure 6.2(b). For all Co, $\overline{D}/d$ is largest at the channel center and reduces toward the walls, where turbulent stresses and mean shear are elevated. The following two chapters characterize the dynamic, non-linearly interacting mechanisms underlying the distribution and dispersion of aggregate across this joint space of size and wall-normal coordinate (n, y).

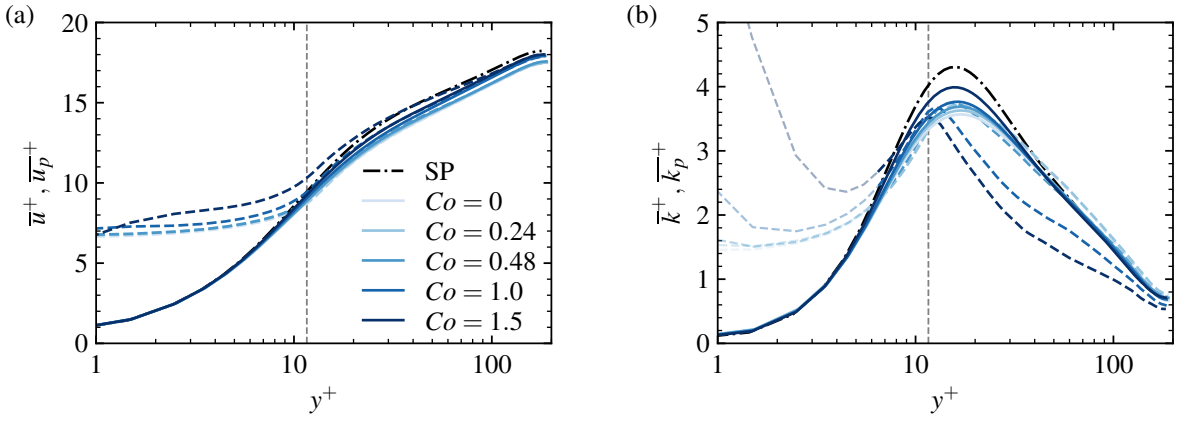


Figure 6.3: (a) Fluid $\overline{u}^+$ (solid) and particle $\overline{u_p}^+$ (dashed) mean streamwise velocity profiles in inner units for each Co. (b) Fluid $\overline{k}^+$ (solid) and particle $\overline{k_p}^+$ (dashed) turbulent kinetic energy profiles in inner units for all Co. The single-phase case is included in each panel as a black dash-dotted line while a vertical grey dashed line denotes a particle diameter d^+. Profiles for $\overline{k_p}^+$ are shown with reduced opacity for $y^+ < d^+/2$, where the near-wall singularity in volume fraction makes the plotted (higher-order) statistic increasingly sensitive to sampling noise.

6.2 Flow modulation

The mean streamwise fluid and particle velocities, $\overline{u}^+$ and $\overline{u_p}^+$, are plotted as a functions of the wall-normal distance in figure 6.3(a), where the fictitious fluid within particles is removed from the computation of fluid statistics, and the methodology detailed in chapter 4 is used to evaluate particle statistics over $N_y = L_y/\Delta x$ wall-normal subdomains. Due to the low mass loading, fluid statistics remain close to the single-phase case (SP) and vary little across Co. Particles adjacent to the wall must still travel with their center of mass velocity so, within one particle diameter of the wall, $y^+ < d^+ = 11.6$, particles maintain higher streamwise velocities than the fluid owing to their finite size [118]. This layer of particles is termed the "particle-wall layer" and is responsible for a large portion of the drag increase observed in suspensions of finite sized particles [118] which will be discussed shortly.

The turbulent kinetic energy (TKE) for both phases, $\overline{k}^+$ and $\overline{k_p}^+$, are reported in

figure 6.3(b). The fluid phase TKE is most prominently suppressed in the buffer layer, a well reported effect in similar particle-laden flows [128] which appears to reduce with increasing Co. For the particle phase TKE, the curves are given a reduced opacity for $y^+ < d^+/2$ where, because the local volume fraction must approach zero in proximity of the wall statistics conditioned on the solid phase become increasingly sensitive to sampling noise. This is especially apparent in second or higher order statistics and can not be readily ameliorated due to the singularity in ϕ at the wall. Beyond this region, $\overline{k_p}^+$ is generally observed to monotonically increase with Co, with $\overline{k_p}^+ < \overline{k}^+$ for larger $Co = \{1.0, 1.5\}$ and $\overline{k_p}^+ \approx \overline{k}^+$ for lower Co; an observation consistent with the creation of larger, more inertial aggregates. Importantly, the presence of fluctuations in the particle phase enhances collision rates and aggregate formation [85], and underpins the aggregation and breakup results presented in this work.

To investigate further into the turbulent properties of the fluid and particles the profiles of the velocity fluctuations, $\overline{u'u'}$, $\overline{v'v'}$, $\overline{w'w'}$, and Reynolds shear stress $-\overline{u'v'}$ are reported in inner units for both the fluid and particles in figure 6.4 where fluctuations of the solid phase are denoted by a subscript $_p$. The statistics for the single phase case, SP, are also included for comparison.

The formation of aggregates comprised of hundreds of primary particles has a modest but measurable effect on the carrier fluid statistics, apparent in the Reynolds stresses as an increase of peak streamwise fluctuations $\overline{u'u'}$ and a decrease in spanwise fluctuations $\overline{w'w'}$ relative to the single-phase case. Schutte et al. [39] report deviations in these two components of approximately -10% at similar volume loading, though they consider point-like primary particles that are negatively buoyant, $\rho_s \in \{1.5, 2.0\}$. Here, with finite-sized, neutrally buoyant particles, we find deviations of $\approx +13\%$ between the cohesionless and most cohesive cases for $\overline{u'u'}$ – the opposite sign of what Schutte et al. [39] report – with intermediate-Co cases falling monotonically between. For $\overline{w'w'}$, we

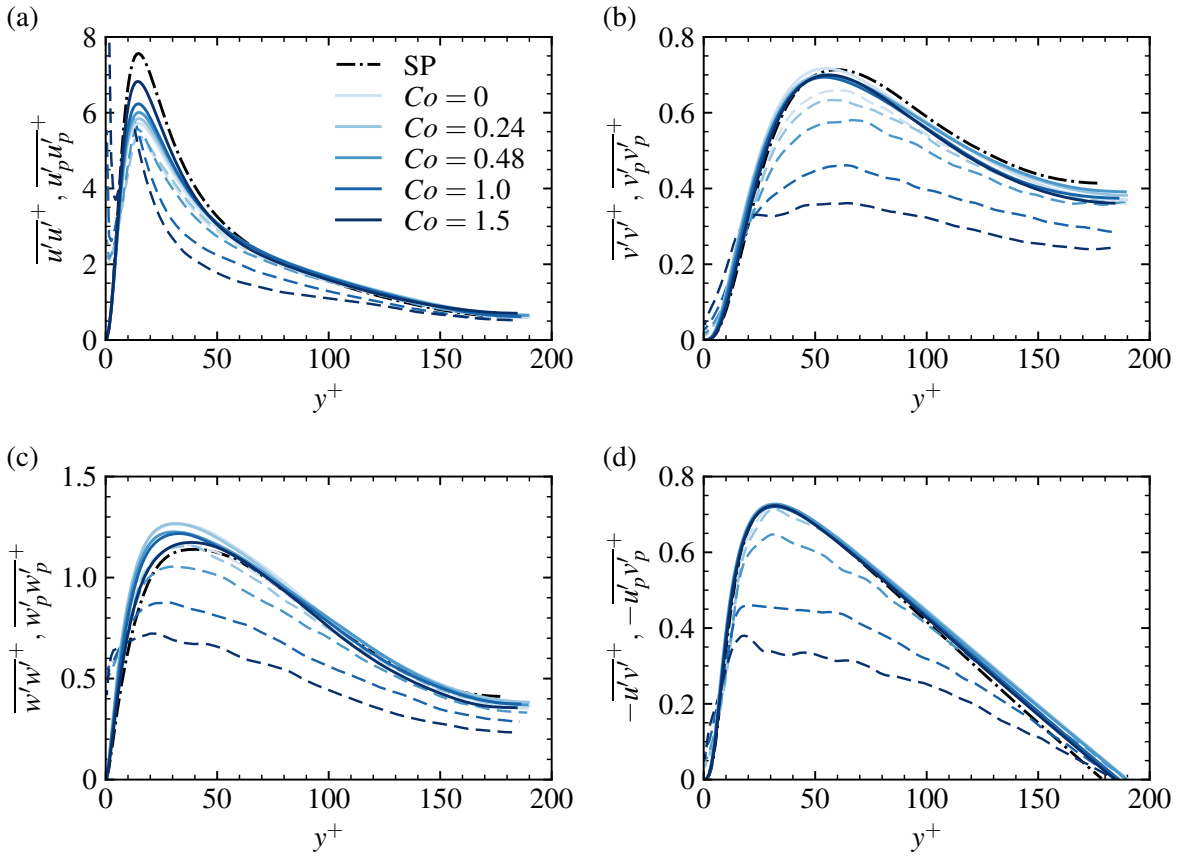


Figure 6.4: Velocity fluctuations and Reynolds shear stress profiles over the inner-scaled wall-normal distance y^+, for the fluid phase (solid) and the particles (dashed), across cohesive number Co: (a) streamwise, (b) wall-normal, and (c) spanwise velocity fluctuations and (d) Reynolds shear stress. The single phase (SP) statistics are included as a black dash-dotted line. Velocities are normalized by the friction velocity. As in figure 6.3, particle quantities are denoted by a subscript $_p$.

observe a similar-magnitude reduction of -15% between the cohesionless and most cohesive cases, consistent with their findings, again with intermediate-Co cases filling the range monotonically. The common trend in both deviations is that increasing Co pushes the fluctuations toward the single-phase values: the single-phase case exhibits higher streamwise and lower spanwise fluctuations than the channel laden with cohesionless particles.

More striking are the profiles of the particle fluctuations are shown with dashed lines and are significantly suppressed with increasing Co. Indeed, at first glance, the increasingly large aggregates with Co have significantly fluctuations in all directions. Indeed the most cohesive case $Co = 1.5$ maintains particle fluctuations nearly half that of the non-cohesive case across a wide range of y for every term of the Reynolds stress tensor examined here. Adjacent to the wall the fluctuations increase due to the finite size of the particles. Note that $\overline{u_p' u_p'}$ displays the near-wall divergence already discussed in the context of the TKE.

The reduction of fluctuations with increasing aggregate size is consistent with the established behavior of finite-size particles in turbulence, which are known to spatially and temporally filter the surrounding flow field on account of their larger spatial scale and correspondingly longer response time. The work of Sanness Salmon et al. [129] provides an intriguing framework to further investigate this through the autocorrelation of the Lagrangian velocity signal of tracked aggregates. Naively implementing such a statistic yields results confounded by the spatial variation of aggregate size in the wall-normal direction: larger aggregates reside preferentially toward the channel center and, as a result, experience less intense forcing than the smaller aggregates found closer to the wall, where the local turbulence intensity is higher. Accounting for this requires binning the statistics sufficiently finely in the wall-normal direction, which significantly diminishes the quantity of data available in each bin. A full characterization therefore requires more

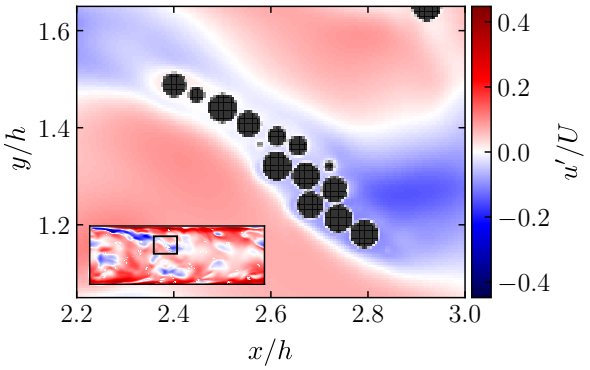


Figure 6.5: Slice of the instantaneous streamwise velocity fluctuation field taken on the xy-plane. The snapshot is focused on an elongated aggregate which is made black using the fluid indicator function for that slice. The aggregate resides within a region of low-speed flow ($u' < 0$), which it appears to perturb, as evidenced by the red outline ($u' > 0$) directly adjacent to the particles.

statistics than are presently available, and this discussion is left open for future work. Figure 6.5 motivates this discussion, presenting the instantaneous streamwise fluctuation field within which an elongated aggregate appears to perturb its local surrounding fluid.

Interestingly, the culmination of these disturbances to the carrier fluid results in a 3% reduction of drag relative to the single-phase case, as shown in figure 6.6. Here, the friction Reynolds number Re_τ, constructed from the wall shear stress, is shown as a function of Co, with the single-phase value $Re_\tau = 179.8$ indicated by a horizontal black dashed line. As previously mentioned, particle-laden flows typically exhibit increased drag relative to the single-phase case, driven primarily by the particle wall layer [116, 118]. Here, however, the wall-normal volume fraction profile shows that this layer is depleted as Co increases. Consistent with the aggregate number density and mean diameter profiles discussed above, the small aggregates that would otherwise populate the wall layer are instead incorporated into larger aggregates residing in the channel center. The near-wall fluid is therefore no longer energized by high-slip-velocity particles, which reduces the near-wall velocity gradient and, correspondingly, the wall shear stress.

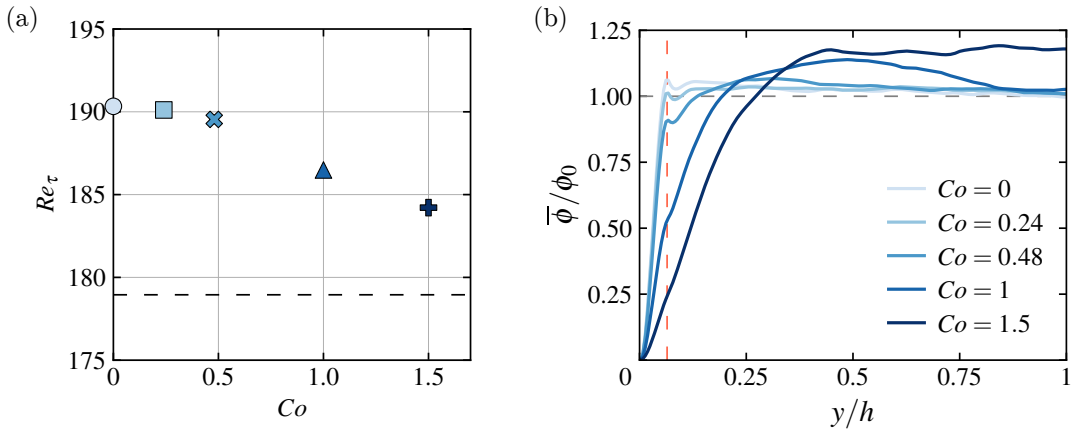


Figure 6.6: (a) Measured friction Reynolds number Re_τ over the cohesive number Co. (b) Wall-normal profile of the volume fraction $\overline{\phi}$ relative to the bulk volume fraction $\phi_0 = 0.015$ for each Co case. A gray dashed horizontal line denotes ϕ_0 while a vertical red dashed line shows $y = d$. The wall-normal coordinate y is made dimensionless using the half channel height h.

6.2.1 Total stress balance

The wall shear stress gives the total momentum exchange between the suspension and walls. The momentum exchange between the particles and fluid can also be interrogated by computing the streamwise momentum balance. Following the framework developed by Zhang & Prosperetti [130] and Marchioro et al. [131] and refined for PR-DNS by Picano et al. [116], the total plane-and-time averaged stress balance can be written as,

$$\overline{\tau} = \overline{\tau_\nu} + \overline{\tau_T} + \overline{\tau_P}, \tag{6.1}$$

where $\overline{\tau} = u_\tau^2(1-y)$ is the total stress, $\overline{\tau_\nu} = \nu\overline{(1-\phi)\frac{\mathrm{d}u}{\mathrm{d}y}}$ is the viscous stress, $\overline{\tau_T} = -\overline{u_c' v_c'}$ is the Reynolds shear stress of the combined phase, with $\overline{u_c' v_c'} = \overline{\phi u_p' v_p'} + \overline{(1-\phi)u'v'}$ equal to the sum of the particle ($\overline{\phi u_p' v_p'}$)and fluid Reynolds stresses, and $\overline{\tau_P} = \overline{\phi\sigma_{p,xy}}/\rho_f$ the particle induced stress. The particle stress tensor σ_p, of which the xy component, $\sigma_{p,xy}$ is included in $\overline{\tau_P}$, is the local stress tensor that reproduces, via its surface integral, the net force and torque acting on each particle, including lubrication and contact forces.

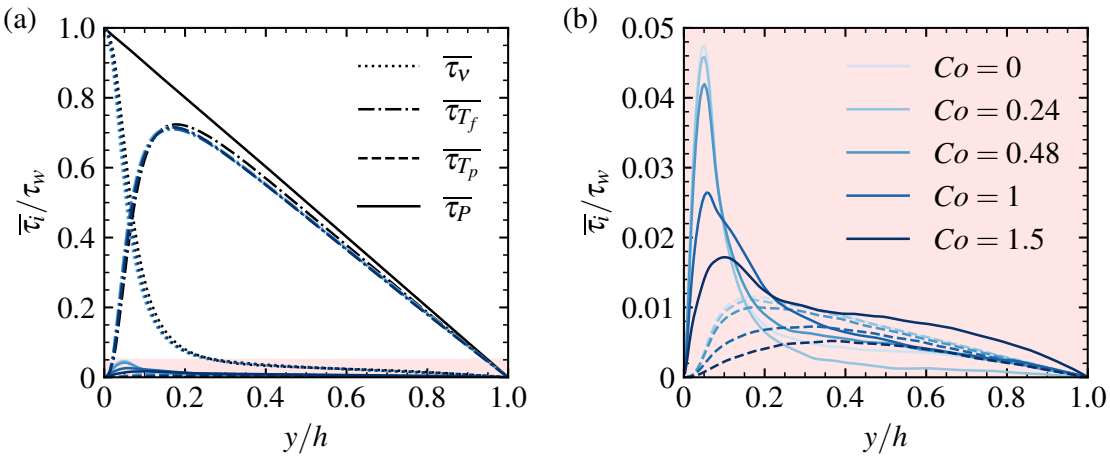


Figure 6.7: Shear stress balance for the cohesive particle laden cases, $Co = [0, 1.5]$, showing wall-normal profiles of the viscous stress (τ_ν), Reynolds shear stress τ_{T_f}, particle Reynolds shear stress τ_{T_P}, and particle induced stress τ_P. The main plot shows the range $\tau = [0, 0.05]$, where τ_P and τ_{T_P} are shown on a red background. The red background highlights the same region in the inset, which shows the full range of total stress $\tau = \tau_w(1 - y/h)$ and includes τ_ν and τ_T.

In practice, $\overline{\tau_P}$ is obtained as the residual required to close the stress balance, equation (6.1), once $\overline{\tau_\nu}$ and $\overline{\tau_T}$ are computed [116].

The shear stress profiles are shown normalized by the case-respective wall-shear stress τ_w in figure 6.7(a), where each stress is given a distinct line style. $\overline{\tau_{T_P}}$ and $\overline{\tau_P}$ are examined more closely in figure 6.7(b), where a red background corresponds to the similarly highlighted region at the bottom of figure 6.7(a). The particle-laden cases are shown in blue tones, while the single-phase case is shown in black. Note that equation 6.1 reduces to the single-phase stress balance as $\phi \to 0$, with $\overline{\tau_{T_P}} \to 0$ and $\overline{\tau_P} \to 0$. These terms are correspondingly absent for the single-phase case in figures 6.7(a) and (b). As required, the viscous stress, $\overline{\tau_\nu}$, equals the wall shear stress τ_w at the wall and decays to zero in the channel center. The momentum transport by fluid turbulent activity, τ_{T_f}, is the primary mechanism responsible for wall-normal momentum transport beyond the buffer layer, $y \approx 0.1$. Due to the mass and volume fraction loading, little momentum is transported

by the solid phase, with the small percentage that is ($\approx$ 1-5% depending on Co) examined more closely in figure 6.7(a) as mentioned above. Here, the removal of the particle wall layer is evident in the reduction of peak particle-induced stress directly adjacent to the wall, $y \approx 0.05$. For low Co, τ_P peaks approximately 5% of the shear stress, with this peak progressively diminishing with increasing Co. An important point of context is that this local particle stress is quite high given the volume loading, and again demonstrates the dramatic effect of the particle wall layer, which is progressively disrupted with increasing Co. For a suspension of bulk volume fraction $\phi_0 = 0.015$, the Einsetin viscosity law [132, 133] predicts a bulk increase in stress of only $2.5\phi_0 = 3.75\%$, notably smaller than the local near-wall peak observed here. This redistribution is consistent with the volume fraction profiles shown in figure 6.6(b). As will be shown in chapter 7, with increasing Co aggregates become stronger, and fewer small fragments are left in the near-wall region. With this breakup-driven deposition suppressed, particles remain concentrated in larger aggregates further from the wall, broadening the wall-normal extent over which $\overline{\tau_P}$ and accounting for both the reduction in its near-wall peak and its frowth toward the channel center at higher Co. Finally, corroborating the findings of suppressed solid-phase turbulent activity in the fluctuation profiles at higher Co (figure 6.4), the particle turbulent stress, $\overline{\tau_{T_P}}$ reduces with Co.

6.3 PBE kernels

Accurate parameterization of the aggregation and breakup kernels is essential for the performance of PBE based sediment transport models. Exploiting the detailed statistics on aggregation and breakup provided by simulation allows for explicit measurement of, for example the breakup rate, g_b, and fragment size distribution q_b. The bulk breakup rate estimator, equation (4.19), $\overline{\overset{\circ}{g_b}}$, computed over the sampling interval, is shown in

figure 6.8(a), where error bars denote a 95% confidence interval in this and proceeding figures. Intuitively, $\overset{\circ}{\overline{\overline{g_b}}}$ decreases with increasing cohesive strength Co, reflecting the enhanced stability of aggregates held together by stronger bonds. Notably, the breakup rate exhibits a scaling with effective aggregate surface area, $\propto D^2$. Power-law fits of the form $y = Ax^2$ are shown for each case in figure 6.8(a). Rescaling by cohesive strength collapses the data, with $\overline{g_b}Co \propto D^2$, as shown in figure 6.8(b) where it is accompanied by a power-law fit of the collapsed data and suggests that simplified models for $\overline{\overline{g_b}}$ require only a single functional form, independent of Co. The scaling with aggregate surface area holds primarily at large D/d, where the notion of an effective diameter remains meaningful. The compensated breakup rate, $\overline{\overline{g_b}}D^{-2}Co$, is shown in figure 6.8(c) to highlight this convergence.

To further characterize the breakup process, we examine the bulk parent-child fragment distribution across breakup events. The probability density function (PDF) of fragment sizes, computed from $q_b(D_p, D_c)$, is expressed in terms of the child-parent volume ratio $D_c^3/D_p^3 \in (0, 1)$ and shown across 9 bins in figure 6.9. To suppress the highly discrete contributions of small aggregate breakup, we only consider events with $D_p/d > 3$. By mass conservation, the distribution is symmetric about $D_c^3/D_p^3 = 0.5$.

An analogous distribution can be constructed for aggregation events. Here we define

$$\Psi = \frac{D_1^3}{D_1^3 + D_2^3}, \tag{6.2}$$

where D_1 and D_2 denote the diameters of the two coalescing aggregates. The PDF of Ψ is shown in figure 6.9(b).

The PDF in panel (a) is strongly peaked near the extremes, indicating that breakup predominantly produces one large and one small fragment, consistent with an erosional breakup mechanism. Notably, the distribution is largely independent of Co, in agreement

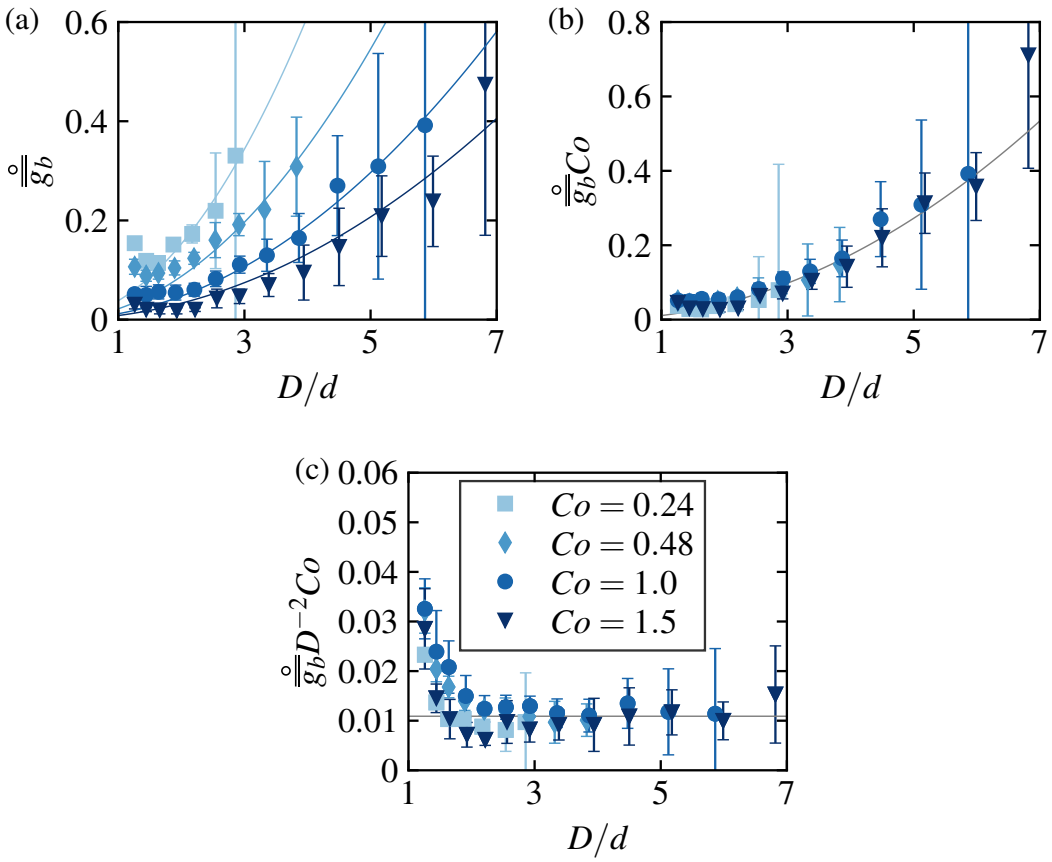


Figure 6.8: (a) Breakup rate, $\overline{\overline{g_b}}$, versus normalized aggregate size D/d. (b) Rescaled by Co to demonstrate collapse. (c) Compensated by $D^{-2}Co$ to highlight the D^2 scaling. Power law fits $y = AD^2$ are shown as solid lines in each panel. Error bars denote a 95% confidence interval (c.f. figure 6.2 caption).

with observations in 2D interfacial turbulence [134], but not previously reported for 3D wall-bounded flows. The beta distribution,

$$\overline{\overline{q_b}}(D_p, D_c) = \\ 2D_c^{3(\alpha-1)} \left(D_p^3 - D_c^3\right)^{\alpha-1} D_p^{-6(\alpha-1)-3} \,/\, B(\alpha, \alpha) \tag{6.3}$$

is commonly employed to capture such fragment distributions for flows of bubbles and droplets. Here we borrow the formulation of Chan et al. [65], in which B is the beta function and α is the single free parameter. Fitting the accumulated breakup data for all Co yields $\alpha = 0.46$, with the resulting PDF shown as a black line in figure 6.9(a). The same functional form fit to the distribution of Ψ in panel (b) yields $\alpha = 0.36$, shown as a black line in figure 6.9(b). The agreement between equation (6.3) and the data is good in both cases, demonstrating its viability as a model fragment size distribution to parameterize the breakup and aggregation kernels.

Finally, to begin to interrogate breakup as a function of aggregate size we consider the largest fragment ratio, $D_{c,L}/D_p$, defined as the size of the larger of the two fragments produced in a breakup event relative to the parent aggregate, shown as a function of parent size D_p/d in figure 6.9(c). For the smallest parents, $D_{c,L}/D_p$ is fixed at 0.5, since an aggregate of size $n = 2$ can only break into two equal fragments. The ratio grows with D_p/d, reflecting the shift toward increasingly asymmetric, erosional breakup, before plateauing at $D_{c,L}/D_p \approx 0.8$ for $D_p/d \gtrsim 2.5$.

Absent from this discussion is the aggregation rate estimator, $\overset{\circ}{\overline{\overline{\beta}}}(D_1, D_2)$. Unlike Qi et al. [134], who report an approximate collapse of the coalescence kernel with $(D_1 + D_2)^2$, albeit for a vastly different configuration, we find no such simplification in the present, more complex, wall-bounded 3D system. As a consequence, we only present the matrices of the aggregation kernel estimator $\overset{\circ}{\overline{\overline{\beta}}}$ for $Co > 0$ in figure 6.10, for completeness. In

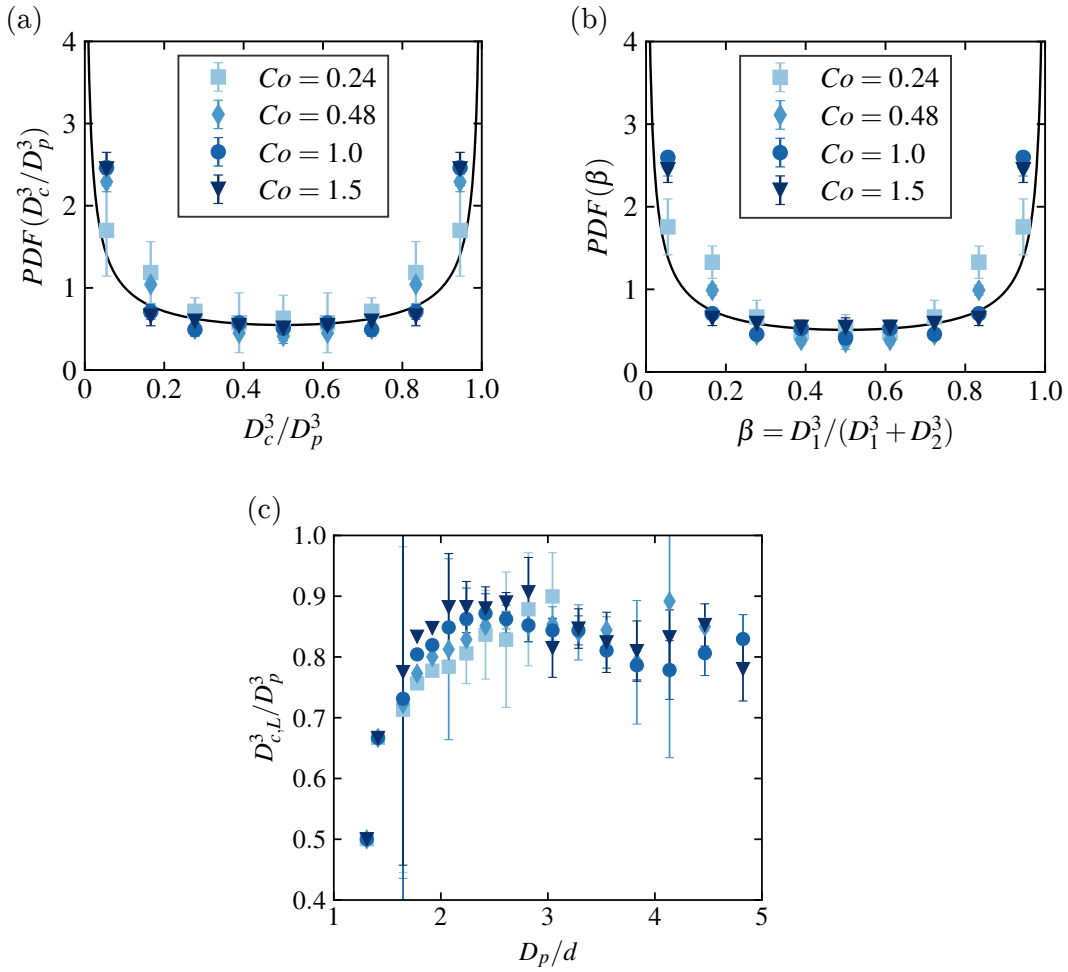


Figure 6.9: Probability density function (PDF) of (a) child-to-parent fragment volume ratios, D_c^3/D_p^3, for each $Co > 0$ for breakup and (b) the ratio of parent to child volume Ψ across for aggregation events. For breakup only events where $D_p > 3$ are considered. Similarly, for aggregation, only events where $(D_1^3 + D_2^3)^{1/3} > 3$ are considered. Equation (6.3) is fit to the data for all Co and shown as a black lines in (a) and (b). (c) Ratio of mass of largest fragment to parent aggregate mass $D_{c,L}^3/D_p^3$ for breakup events as a function of parent size D/d. Error bars denote a 95% confidence interval (c.f. figure 6.2 caption).

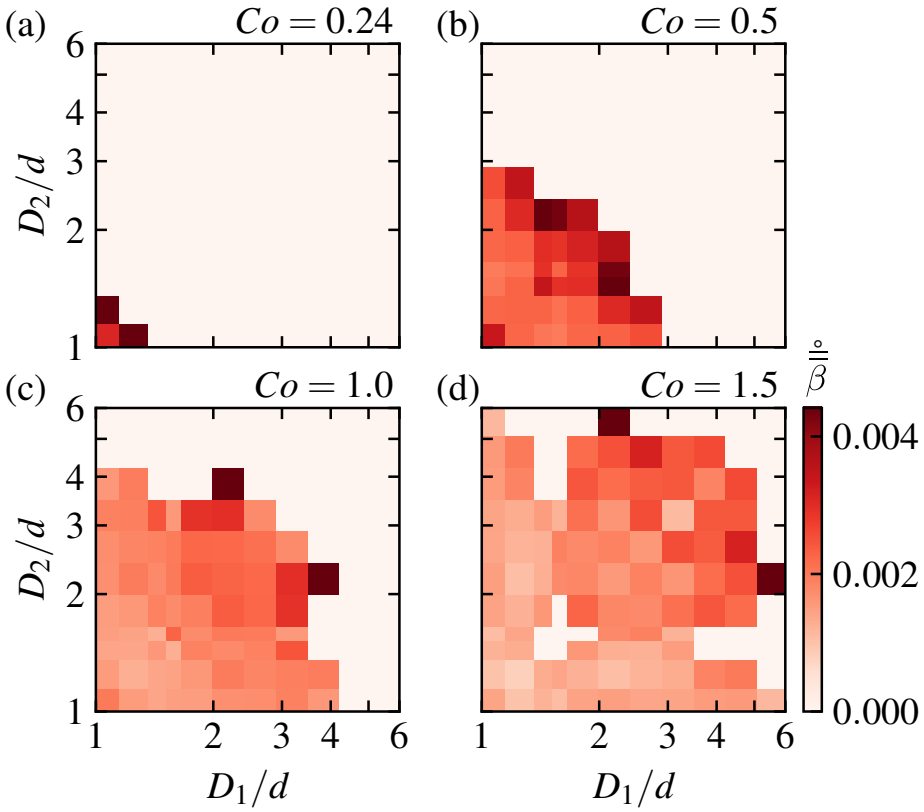


Figure 6.10: Aggregation kernel estimator $\overline{\overline{\beta}}^{\circ}$ shown as a matrix over the space of the two parent aggregate sizes D_1/d and D_2/d for (a) $Co = 0.24$(b) $Co = 0.48$, (c) $Co = 1.0$ and (d) $Co = 1.5$. Only bins with more than 10 aggregation events are considered.

constructing figure 6.10 only bins in which more that 10 aggregation events are sampled are considered.

6.4 Summary

After an initial aggregation-dominated transient, investigated in chapter 5, the aggregate population reaches a statistically stationary state wherein aggregation and breakup globally balance. During this period, the mass-weighted aggregate number density takes a log-normal form at higher Co for larger sizes. Due to the highly anisotropic and inho-

mogeneous flow field, the size distribution also varies in the wall-normal direction, with the largest aggregates present in the channel center where turbulence intensities and shear are low.

The formation of coherent particulate structures larger than the primary particle size is also found to modulate the underlying turbulence. In comparison to the cohesionless case, Reynolds stresses are shown to reapproach the single phase values as Co is increased. This results in a drag reduction relative to the cohesionless case that is shown to be caused by the removal of a highly-dissipative wall-layer of particles.

As aggregates interact with the surrounding flow field, they continuously break and reform. The population balance equation framework developed in chapter 4 allows for the direct measurement of the PBE kernels that are ultimately used as parameterizations in reduced order cohesive sediment transport models. Here we extract the breakup rate and demonstrate it's scaling with the aggregate surface area D^2. Corroborating this picture, breakup is shown to be predominantly erosional; i.e. aggregates most frequently break into large-small pairs. A similar distribution of parents and children is measured for aggregation, with both aggregation and breakup parent-child distributions well described by the beta distribution (equation 6.3), commonly employed in droplet and bubbly flows [65]. The aggregation kernel is shown to have a non-trivial dependence on the two parent sizes, which is further confounded by the cross correlations discussed in chapter 4.

Chapter 7

PBE balance[1]

7.1 Global PBE balance

When considering the full domain volume, the PBE is balanced solely by aggregation and breakup, as expressed by equation (4.24). The measured bulk source terms, $\overline{\overline{S_i}}(n)$, for the cases $Co > 0$ are shown in Figure 7.1 (a–d) across size-space. Trivially, $\overline{\overline{A_+}} = \overline{\overline{B_-}} = 0$ at $n = 1$ for all Co, since monomers cannot be produced by aggregation nor break. It follows that at $n = 1$, $\overline{\overline{B_+}} = -\overline{\overline{A_-}}$, reflecting that monomers are produced solely by breakup of larger aggregates and are removed only through aggregation.

At larger sizes, $\overline{\overline{A_+}}$ and $\overline{\overline{B_-}}$ become active as mass is transferred bidirectionally in size-space. The sum of all contributions, $\overline{\overline{Q}} = \sum \overline{\overline{S_i}}$, shown in black, is approximately zero for all cases, consistent with (4.24), and demonstrating conservation of mass across size-space.

[1]This chapter contains previously published work, adapted here with minor modifications from the following references: A. D. Leonelli and Meiburg, E. (2026). *Turbulent Channel Flow with Cohesive Particles, Proceedings of the 14th International Symposium on Turbulence and Shear Flow Phenomena.* Heidelberg, Germany. & A. D. Leonelli, L. Widmer, and E. Meiburg, *Aggregation, breakup, and size-dependent transport in a turbulent channel flow with cohesive particles*, 2026. Under review at *J. Fluid Mech.* at the time of dissertation submission.

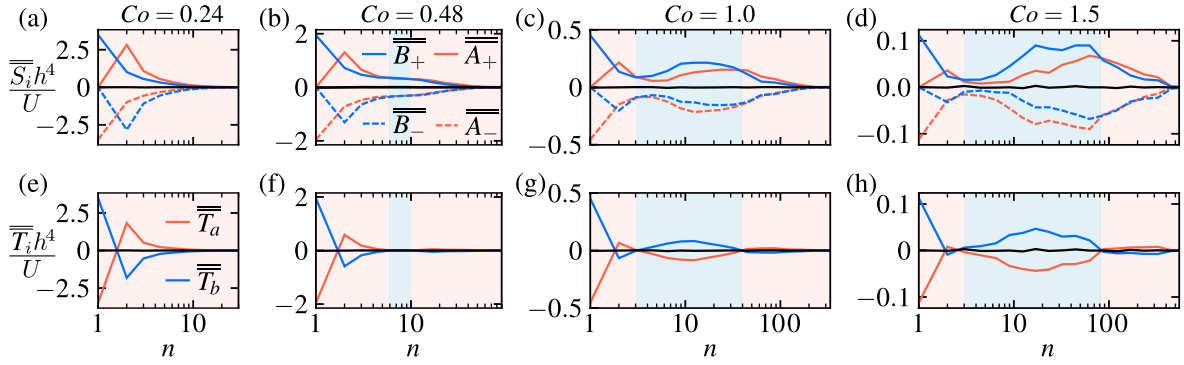


Figure 7.1: Volume- and time-averaged aggregation and breakup source terms, $\overline{\overline{S_i}}$ (a-d) and net aggregation and breakup source terms $\overline{\overline{T_a}}$ and $\overline{\overline{T_b}}$ (e-h). Each column shows data for a single, nonzero cohesive strength. The $\overline{\overline{S_i}}$ are defined in chapter 4 while $\overline{\overline{T_a}}$ and $\overline{\overline{T_b}}$ are given by equations (7.1) and (7.2) respectively. Sizes $n > 1$ where $\overline{\overline{T_a}} > \overline{\overline{T_b}}$ are highlighted with a red background whereas those with $\overline{\overline{T_b}} > \overline{\overline{T_a}}$ have blue backgrounds.

To further aid interpretation, the net aggregation and breakup fluxes,

$$\overline{\overline{T_a}} = \overline{\overline{A_+}} + \overline{\overline{A_-}}, \tag{7.1}$$

$$\overline{\overline{T_b}} = \overline{\overline{B_+}} + \overline{\overline{B_-}}, \tag{7.2}$$

are shown as red and blue curves in panels (e–h), respectively. The quantity $\overline{\overline{T_a}}$ represents the net gain or loss of size n aggregates due to aggregation alone. $\overline{\overline{T_a}}(n) > 0$ indicates that formation from smaller sizes exceeds loss to larger sizes, implying a net aggregation-driven flux of mass into n from below. Conversely, $\overline{\overline{T_a}} < 0$ implies a net transfer of mass out of n towards larger aggregates. $\overline{\overline{T_b}}$ is analogously constructed for breakup. $\overline{\overline{T_b}} > 0$ indicates a net breakup-driven flux of mass into n from above while $\overline{\overline{T_b}} < 0$ indicates a net transfer of mass from n to smaller sizes.

Taken together, $\overline{\overline{T_a}}$ and $\overline{\overline{T_b}}$ provide a compact representation of the local directional mass fluxes in size-space, isolating the competing roles of aggregation-driven mass flux to larger n and breakup-driven flux downscale. As before, the combined rate $\overline{\overline{Q}} = \overline{\overline{T_a}} + \overline{\overline{T_b}} =$

$\sum \overline{\overline{S_i}}$ is shown as a black line. Deviations from 0 should be interpreted as error since particle mass is conserved over the full domain.

With this statistical formulation in mind, we revisit panels (e-f) in figure 7.1. At the lowest nonzero cohesion, $Co = 0.24$ (panels (a,e)), $\overline{\overline{T_a}} \geq 0 \geq \overline{\overline{T_b}}$ for all $n > 1$ with $\overline{\overline{T_a}} = -\overline{\overline{T_b}}$ as required by (4.24). Thus, aggregation acts to bring mass to all $n > 1$ while breakup acts as a sink to balance. Restated, for all $n > 1$ aggregation of smaller aggregates into size n outcompetes further aggregation of size n into larger sizes, thus $\overline{\overline{T_a}} > 0$. Necessarily, $\overline{\overline{T_b}} \leq 0$ indicating that breakup of size n to smaller scales outpaces incoming fragments of size n from the breakup of larger aggregates. In contrast, the strongest cohesion, $Co = 1.5$ (panels (d,h)), displays a significant range of sizes where $\overline{\overline{T_b}} \geq 0 \geq \overline{\overline{T_a}}$ indicating that these n receive mass from larger sizes ($\overline{\overline{T_b}} \geq 0$) and, on-average, redistribute it upscale $\overline{\overline{T_a}} \leq 0$. This region is highlighted using a blue background for each panel. Inspecting panel (d) it is apparent that $\overline{\overline{B_+}}$ is balanced by $\overline{\overline{A_-}}$ in this region, revealing a statistical cycle that limits further fragmentation. Finally, a complementary range of sizes where $\overline{\overline{T_a}} \geq 0 \geq \overline{\overline{T_b}}$ is necessarily present at larger n and is highlighted by a red background.

The range of n where $\overline{\overline{T_b}} \geq 0 \geq \overline{\overline{T_a}}$ grows smaller with decreasing Co and is not present at $Co = 0.24$, where cohesion is too weak to interrupt a statistically continuous transfer of mass downscale due to breakup (i.e. breakup is a sink for all $n > 1$). This is emphasised by the phase diagram presented in figure 7.2 wherein the red and blue regions of $\overline{\overline{T}}_a > \overline{\overline{T}}_b$ and $\overline{\overline{T}}_b > \overline{\overline{T_a}}$ are shown in the space of aggregate size D/d and cohesive strength Co. The separation between these regions is drawn using a dashed line with black and white circular markers show the region boundaries measured from figure 7.1. The upper bound is set by the maximum aggregate size, denoted using black diamonds and a solid connecting line. Notably, the appearance of the region $\overline{T_b} > \overline{T_a}$ correlates with the appearance of the log-normal region in the aggregate number density

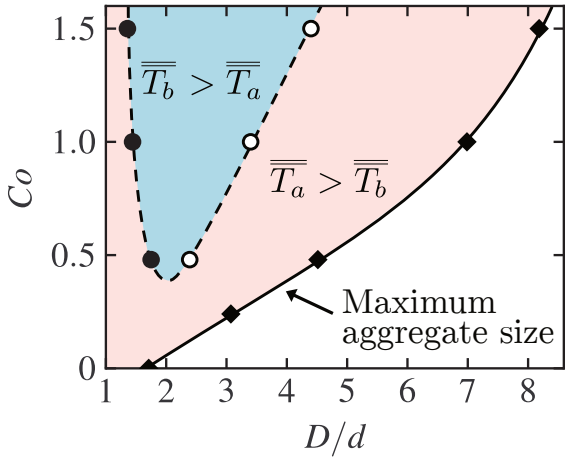


Figure 7.2: Phase diagram showing the regions in the space of cohesive strength Co and aggregate size D/d where aggregation acts as a source and breakup a sink, $\overline{\overline{T_a}} > 0 > \overline{\overline{T_b}}$, in red and regions where breakup acts as a source $\overline{\overline{T_b}} > 0 > \overline{\overline{T_a}}$ in blue. The form and separation between the regions is drawn through the region bounds measured from the data presented in figure 7.1. The upper and lower bounds of the regions from the data are also marked with black and white circular markers respectively. The maximum aggregate size, shown by black diamonds marks the edge of the regions, with a solid line drawn through the measured data.

shown in figure 6.2, though a causal relationship can not presently be established. Note the exact relationship between these regions and Co is complex and likely flow and geometry dependent.

At this point we have verified that the simulations have reached a statistically stationary state for which the global population balance satisfies $\overline{\overline{Q}}(n) = 0$ for all n, consistent with (4.24). However, it is unknown if this is the case locally in the wall-normal direction.

7.2 Local wall-normal balance

When the PBE is plane-averaged, as in (4.16), the advective term allows for transport of aggregates in the wall-normal direction, hence aggregation and breakup are not

required to locally balance in y. To assess this, we employ the methodology described in section 4.5 to partition the channel into 62 wall-normal subdomains of thickness $\Delta y = d/2$ and evaluate the net source term,

$$\overline{Q}(n,y) = \overline{T_a}(n,y) + \overline{T_b}(n,y), \tag{7.3}$$

for three size classes, $n = 1$, $n = 2, 3$, and $3 < n < 20$. These subsamples must be considered individually since aggregation and breakup conservatively redistribute mass across sizes (i.e. a breakup event at $n = 3$ will be balanced by the breakup source term at $n = 1$ and $n = 2$ in the same y bin), such that

$$\sum_{n=1}^{\infty} \overline{Q}(n,y) = \sum_{n=1}^{\infty} \overline{T_a}(n,y) = \sum_{n=1}^{\infty} \overline{T_b}(n,y) = 0. \tag{7.4}$$

Similarly, in the wall-normal direction,

$$\int_0^{L_y} \overline{Q}(n,y)\mathrm{d}y = 0, \tag{7.5}$$

which is a restatement of equation (4.24).

The resulting net source term, $\overline{Q}(n,y)$, is shown over half the channel, $y/h \in [0,1]$ (exploiting symmetry about $y = h$) in figure 7.3 for $Co = 0.48$. $\overline{Q}(n,y)$ is clearly nonzero, demonstrating that aggregation and breakup are not locally balanced in the wall-normal direction. The top row of figure 7.3 shows the full range of data, while the bottom row places focus on $\overline{Q}$ to highlight imbalance between $\overline{T_a}$ and $\overline{T_b}$. Each curve is accompanied by a shaded region showing a 95% confidence interval computed as described in appendix C.

For monomers ($n = 1$, panels (a,d)), aggregation and breakup trivially act as a sink and source respectively, thus $\overline{T_a} \leq 0$ and $\overline{T_b} \geq 0$ for all y. Near the wall breakup supplies

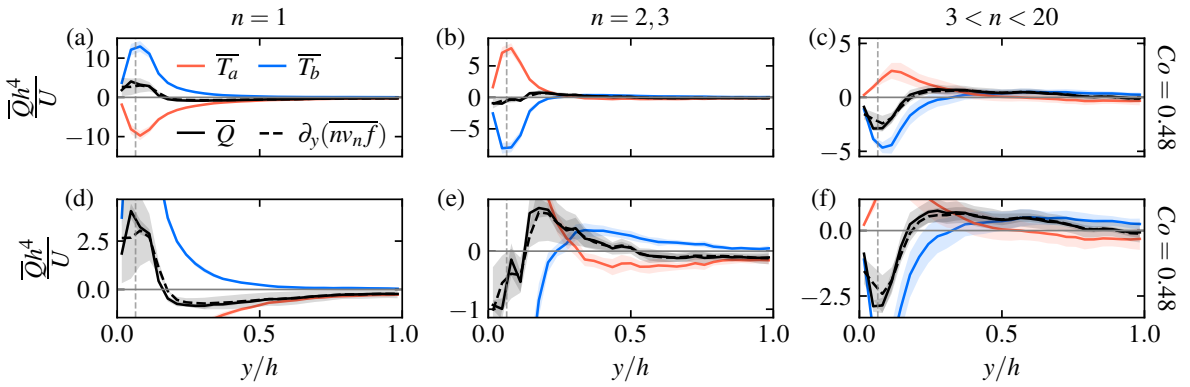


Figure 7.3: The net source due to aggregation and breakup, $\overline{Q}$, aggregation flux $\overline{T_a}$, breakup flux T_b, and advective flux $\partial_y(\overline{nv_nf})$, for three size classes: $n = 1$, $n \in \{2, 3\}$, and $3 < n < 20$ (columns) for $Co = 0.48$ plotted over the half channel height, $y/h \in [0, 1]$. The upper row (a-c) shows the full data range while the bottom row focuses on $\overline{Q}$ and $\partial_y(\overline{nv_nf})$(d-f). A 95% confidence interval is shown by the shaded region surrounding each curve. The gray vertical dashed line corresponds to $y = d$.

mass to the $n = 1$ class faster than aggregation removes it, thus, $\overline{Q} > 0$. Away from the wall, this trend is reversed ($\overline{Q} < 0$) as the removal due to aggregation dominates.

For larger sizes ($3 < n < 20$) the dynamics are equally straightforward as $\overline{T_a} \geq 0$ and $\overline{T_b} \leq 0$ for all y. The near wall region of $\overline{Q} < 0$ is therefore a consequence of breakup-driven depletion outpacing aggregation-driven supply whereas away from the wall breakup slows due to the reduced turbulence intensity and stresses while aggregation is less affected, so that there is a net mass influx to these sizes ($\overline{Q} > 0$) near the channel center.

The dynamics are more intricate for intermediate sizes ($n = 2, 3$, panels (b, e)). Near the wall, aggregation acts as a source ($\overline{T_a} > 0$), breakup as a sink ($\overline{T_b} < 0$), and the net balance is negative ($\overline{Q} < 0$), indicating that breakup-driven loss exceeds aggregation-driven gain. Moving away from the wall, $\overline{Q}$ becomes positive, implying that aggregation now dominates the balance. Interestingly, within this region, aggregation and breakup as source and sink invert as y increases. Toward the channel center, $\overline{Q} < 0$ again, but here depletion is driven by a net mass flux toward larger sizes as aggregation outpaces

the local supply from breakup.

These observed imbalances in aggregation and breakup must be sustained by the wall-normal advection of aggregates as stated in (4.16). Indeed, the resultant advective flux, shown in figure 7.3 (black dashed line), is in good agreement with $\overline{Q}$, demonstrating closure of the PBE in the wall-normal direction.

Results for all $Co > 0$ are presented in figure 7.4. Just as for $Co = 0.48$, $\overline{Q}(n, y) \neq 0$, showing that aggregation and breakup are locally imbalanced for all $Co > 0$. The same general trends for $n = 1$, $n = 2, 3$ and $3 < 20$ are present across Co. Near the wall, monomers are created in excess due to breakup while they are depleted away from the wall by aggregation. For $Co = \{0.24, 0.48\}$, large aggregates ($3 < n < 20$) are on average sourced in the channel center by aggregation and break near the wall. For higher $Co = \{1.0, 1.5\}$, this observation is reversed as aggregates sized $3 < n < 20$ are seen be sourced near the wall by breakup and depleted in the channel center by aggregation, behaving similarly to the $n = 1$ class for lower values of Co. For $Co = \{1.0, 1.5\}$ the complimentary range of sizes in which aggregation acts as a source in the channel center resides at much larger n as shown later in figure 7.5. Intermediate sizes, exhibit net production or depletion that depends on Co: at lower Co, they behave similarly to the $3 < n < 20$ class, whereas at higher Co, they resemble monomers, as they are unable to break in the channel center while continuing to be depleted by aggregation. As for $Co = 0.48$, the advective term is necessary to maintain this inhomogeneity in $\overline{Q}$ and close the PBE. Notably, [128] observed that non-cohesive particles may form aggregate-like clusters dependent on the lubrication model employed. While varying parameters and models is beyond the scope of this work it should be noted given the relative importance of the near-wall region and lubrication interactions demonstrated here.

Having identified regions of net production and depletion, and aware of the intricate interplay between aggregation, breakup, and advection, we now examine how these dy-

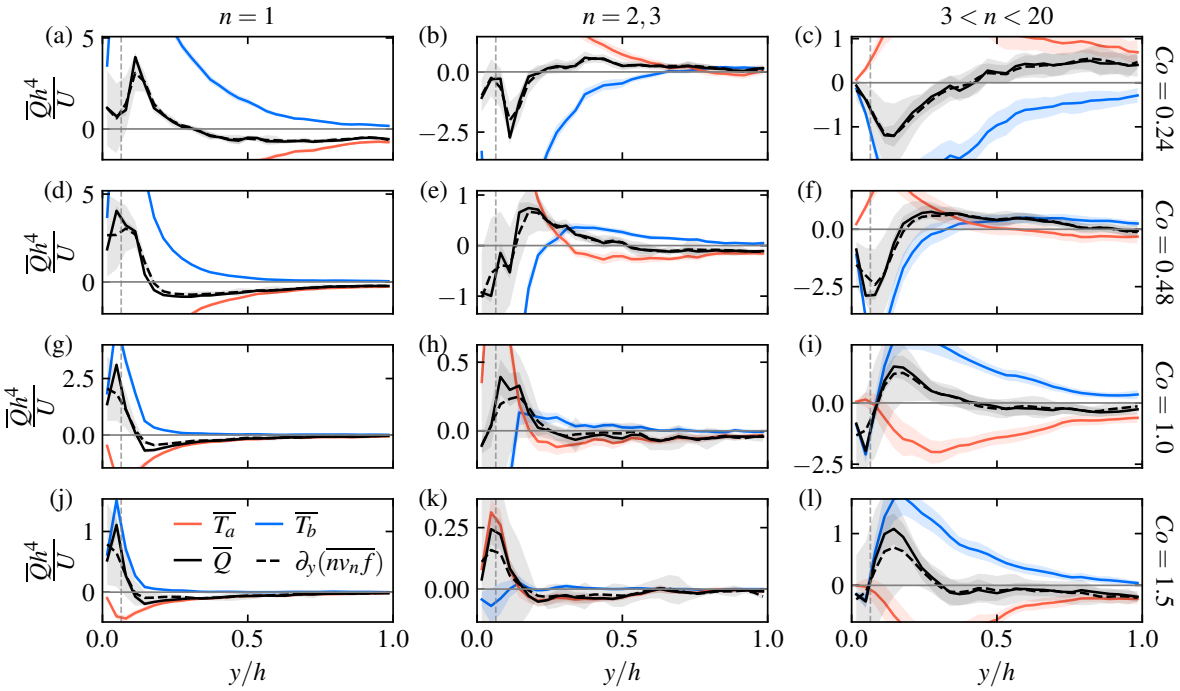


Figure 7.4: The net source due to aggregation and breakup, $\overline{Q}$, aggregation $\overline{T_a}$, breakup $\overline{T_b}$, and advective flux $\partial_y(\overline{nv_n f})$ for three size classes: $n = 1$, $n \in \{2, 3\}$, and $3 < n < 20$ (columns) for $Co > 0$ (rows) plotted over the half channel height, $y/h \in [0, 1]$. As in figure 7.3 (d-f) the axes limits are chosen to focus $\overline{Q}$; a full figure is given in appendix D. A 95% confidence interval is shown by the shaded region surrounding each curve. The gray vertical dashed line corresponds to $y = d$.

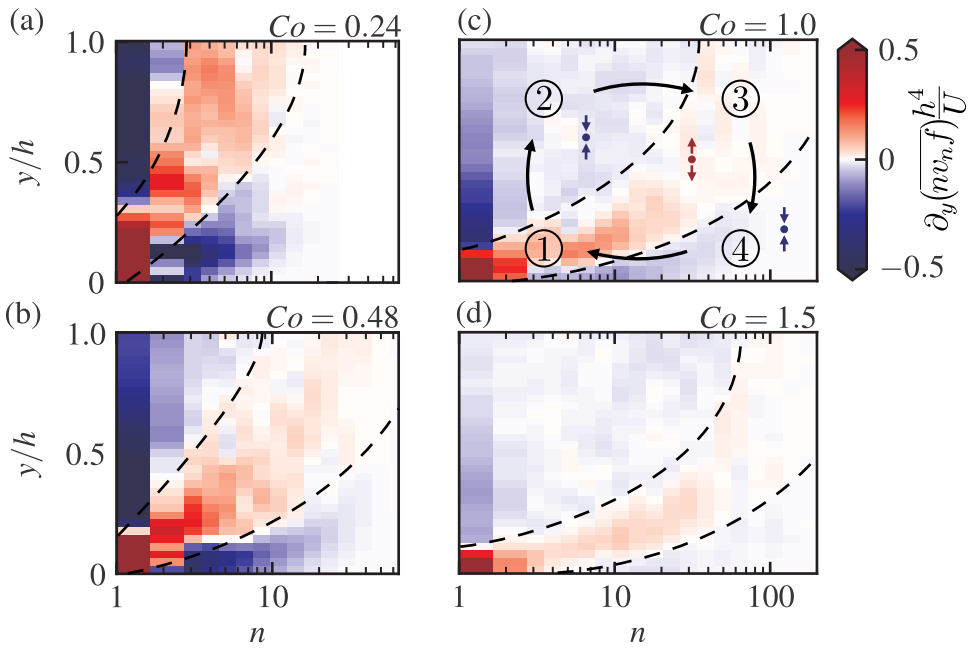


Figure 7.5: Wall-normal advective transport of aggregates, $\partial_y(\overline{nv_nf})$ in (n, y) space for each $Co > 0$ (a-d). Dashed lines are drawn onto the plot to aid in distinguishing between regions of $\partial_y(\overline{nv_nf}) > 0$ (red) and $\partial_y(\overline{nv_nf}) < 0$ (blue). Panel (c) has additional annotation that is used in the text to describe the cyclic transfer of mass through regions 1-4. Symbols with vertical arrows show the divergence of $\overline{nv_nf}$ to compliment the red and blue coloring.

namics organize in (n, y) space. Plotting the wall-normal advective flux (or $\overline{Q}$) in (n, y) space reveals a statistical circulation of aggregates across size and physical space, illustrated in figure 7.5 with four annotated regions in (c). Regions in which the advective flux serves to remove aggregates are red whereas those which accumulate mass are shown in blue. Beginning at region 1, near the wall at small n, the advective flux removes mass. Since no aggregates can be transported through the wall at $y = 0$, this net outflow must carry mass away from the wall toward the channel center, into region 2. There, the advective flux accumulates mass. This region 2 spans from its boundary with region 1 to the channel center. Because region 2 begins at $n = 1$, the advectively accumulated mass cannot be redistributed to smaller sizes and therefore must be transferred upward in size-space into region 3. Region 3 exhibits an advective outflow and spans the channel center, so mass is advected from it toward the wall, into region 4. Note that downscale transfer out of region 3 is statistically precluded, since region 2 already accumulates mass by advection. Region 4 as well accumulates mass by advection, but unlike region 2 it spans from its lower boundary with region 1 up to the maximum aggregate size. Consequently, the inflow from the channel center (region 3) must be balanced by a downscale redistribution of mass back into region 1. Together, these four regions define a closed statistical cycle: small aggregates near the wall are advected toward the channel center, where they grow by aggregation into larger sizes, before migrating back toward the wall to break up and repeat the cycle.

This cyclical structure in (n, y)-space appears at all Co in figure 7.5(a-d), with each region extending to larger n as Co increases. The y-span of region 1 decreases with increasing Co, reflecting that aggregates of a given size are more resilient and thus to break, must travel closer to the wall where stresses are highest. A final subtlety is that the dependence of these trajectories on Co indicates that they are governed by aggregation and breakup, rather than morphology-dependent transport. In other words, the net

production or depletion of aggregates of a given size within a region is controlled by population gradients and not necessarily the propensity of a particular size to migrate toward the channel center or wall.

7.3 Wall interactions and aggregate fate

The circulation identified in figure 7.5 is anchored by region-1, where near-wall breakup depletes the local population of large aggregates and seeds the advective outflow. We now ask what sets the fate of an aggregate that reaches this region, and in particular whether direct contact with the wall, the lubrication model (equation (2.10)), or general hydrodynamic stresses drive breakup near the wall.

A particle-wall collision occurs for particle-wall separations $\zeta_{iw} \leq 0$, with small negative values possible due to the soft-sphere collision model. The lubrication model, which acts in the wall-normal direction only, is active for $0 < \zeta_{iw} \leq 2\Delta x$ while outside this range, the hydrodynamics are fully resolved. To separate these, we define for each aggregate j the smallest particle–wall gap among its set of constituent particles $\mathcal{A}_j$,

$$\zeta_j^A(t) = \min_{i \in \mathcal{A}_j} \zeta_{iw}(t). \tag{7.6}$$

The lifespan of each aggregate terminates by either an aggregation or breakup event at its time of death $t_{d,j}$. For every aggregate, we find the closest approach to the wall before $t_{d,j}$ over a window t_{win},

$$\zeta_{min,j} = \min_{s \in [0,\, t_{win}]} \zeta_j^A(t_{d,j} - s). \tag{7.7}$$

Events are then assigned to one of the three mutually exclusive modes according to $\zeta_{min,j}$: "collisional" ($\zeta_{min,j} \leq 0$), "lubricated" ($0 < \zeta_{min,j} \leq 2\Delta x$), and "hydrodynamic" ($2\Delta x < \zeta_{min,j} \leq 4\Delta x$). Here we choose the "hydrodynamic" region to be of equal

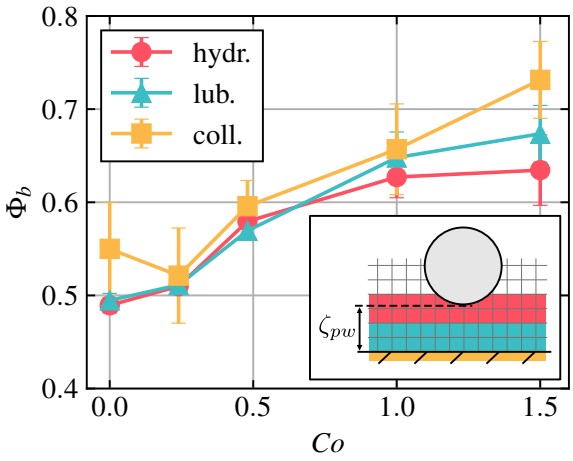


Figure 7.6: Proportion of aggregates that break over the total number of aggregation and breakup events assigned to each mechanism Φ_b plotted over cohesive strength Co; particle-wall collisions, particle-wall lubrication, and shear-induced breakup. Error bars denote a 95% confidence interval. A schematic showing the definition of the regions relative to the grid spacing is shown as an inset where ζ_{iw} is the distance between the surfaces of particle i and wall w. Note that the particle is drawn smaller relative to the grid spacing than in reality.

thickness to the lubrication layer so that the aggregate populations within each region are relatively homogeneous. We use $t_{win} = h/U$ throughout, noting that results remain relatively insensitive to this choice provided $t_{win} > 0.5h/U$ (see appendix F).

Within each region we report the breakup fraction $\Phi_b = N_{break}/(N_{break} + N_{agg})$, which gives the proportion of aggregates that break over the total number of events classified in that region. Figure 7.6 shows Φ_b for each breakup classification across all Co. This analysis applied to the $Co = 0$ case yields $\Phi_b \approx 0.5$ for all breakup categories. This is unsurprising considering that without a cohesive force, inter-particle collisions mostly begin (aggregation) and terminate (breakup) in the same region so that $N_{agg} \approx N_{break}$ locally in the wall-normal direction. With increasing Co the ratio of breakup to aggregation events increases, consistent with the conceptual picture established in section 7.2 that breakup out-competes aggregation in the near-wall region. Notably, Φ_b increases monotonically with Co independent of any region-specific mechanism (collisional, lubricated, hydrody-

namic). This follows from the aggregate size distribution itself (figure 6.2(a)) where for increasing Co a larger fraction of the population resides in large aggregates, depleting the pool of small aggregates available as aggregation partners. At intermediate cohesive strengths, $Co = \{0.24, 0.48, 1.0\}$, Φ_b appears roughly equal for all breakup categories, suggesting that no single interaction disproportionally drives breakup. Only for the most cohesive case, $Co = 1.5$, do the categories separate nearly beyond the 95% confidence interval denoted by the error bars, with $\Phi_b \approx 0.63$ for general hydrodynamic breakup, $\Phi_b \approx 0.67$ for lubrication, and $\Phi_b \approx 0.73$ for particle-wall collisions. This modest but ordered separation ($\Phi_b^{coll} > \Phi_b^{lub} > \Phi_b^{hydr}$), indicates that only at the strongest cohesive strength, $Co = 1.5$, aggregates that interact directly with the wall by either the normal lubrication model or direct contact are increasingly likely to break rather than aggregate. This effect is minimal, especially considering that hydrodynamic forces are still acting on the aggregates in the lubrication and particle-wall collision interactions. Taken together, these results suggest that the fate of an aggregate that enters close enough proximity to the wall to interact by the modeled normal lubrication force is relatively unaffected when compared to those that do not, suggesting that breakup is generally facilitated by hydrodynamic stresses.

7.4 Aggregate orientation and axial straining

To further understand how aggregate dynamics facilitate breakup, we first examine the wall-normal profiles of aggregate orientation. We then show that aggregates maintain rotation rates similar to the fluid, facilitating their alignment with the streamwise- (x) axis. Finally, we show that the rate of strain along the aggregate long axis increases near the wall, demonstrating that aggregates become progressively more extended on approach to the wall, promoting breakup.

We define the orientation of an aggregate j to be the unit principal eigenvector of its gyration tensor, $\boldsymbol{e}_j^A$, as defined in appendix E. The alignment of aggregate j with the domain coordinate triad, $\hat{\boldsymbol{e}}_i$ with $i \in \{x, y, z\}$ is then,

$$\cos\theta_{i,j} = |\boldsymbol{e}_j^A \cdot \hat{\boldsymbol{e}}_i|. \tag{7.8}$$

By construction (7.8) is agnostic to the sign of $\boldsymbol{e}_j^A$, since it is arbitrary. It follows that $|\cos\theta_i| \to 1$ indicates alignment with axis i, while $|\cos\theta_i| \to 0$ indicates misalignment. Averaging over all aggregates size $n > 2$ sampled during T_{eq} and following the binning procedures in chapter 4 for N_y subdomains gives the mean orientation, $\overline{\cos\theta_i}$. For an isotopically oriented population, $\overline{\cos\theta_i} = 0.5$ in every direction i. The wall-normal profiles of the orientation for aggregates with $n > 2$ are shown in figure 7.7(a), where small aggregates are omitted since $\boldsymbol{e}_j^A$ becomes ill-defined. One issue that arises when excluding small aggregates is that the population becomes sparse for low-Co cases, yielding noisy statistics due singularities that arise when the local volume fraction is small. To avoid this, only subdomains where $\overline{\phi}(y_j) > 10^{-3}$ are considered, which is why the data for $Co = 0.24$ is truncated.

In the channel center, aggregate alignment appears generally isotropic, $|\cos\theta_i| \approx 0.5$, with slight misalignment along the y-axis emerging at higher Co. Approaching the wall, aggregates align preferentially with the streamwise direction, with $|\cos\theta_x| \to 0.7$ for all Co, accompanied by a corresponding suppression of wall-normal alignment. Spanwise alignment remains isotropic ($\cos\theta_z \approx 0.5$) throughout.

Since aggregate alignment varies with wall-normal position, and aggregates are simultaneously transported across y, an aggregate carried through this gradient must itself rotate about the spanwise axis to track the local mean orientation, with angular velocity ω_z^A. As shown in figure 7.7(b), the aggregate rotation rate tracks the fluid rotation rate

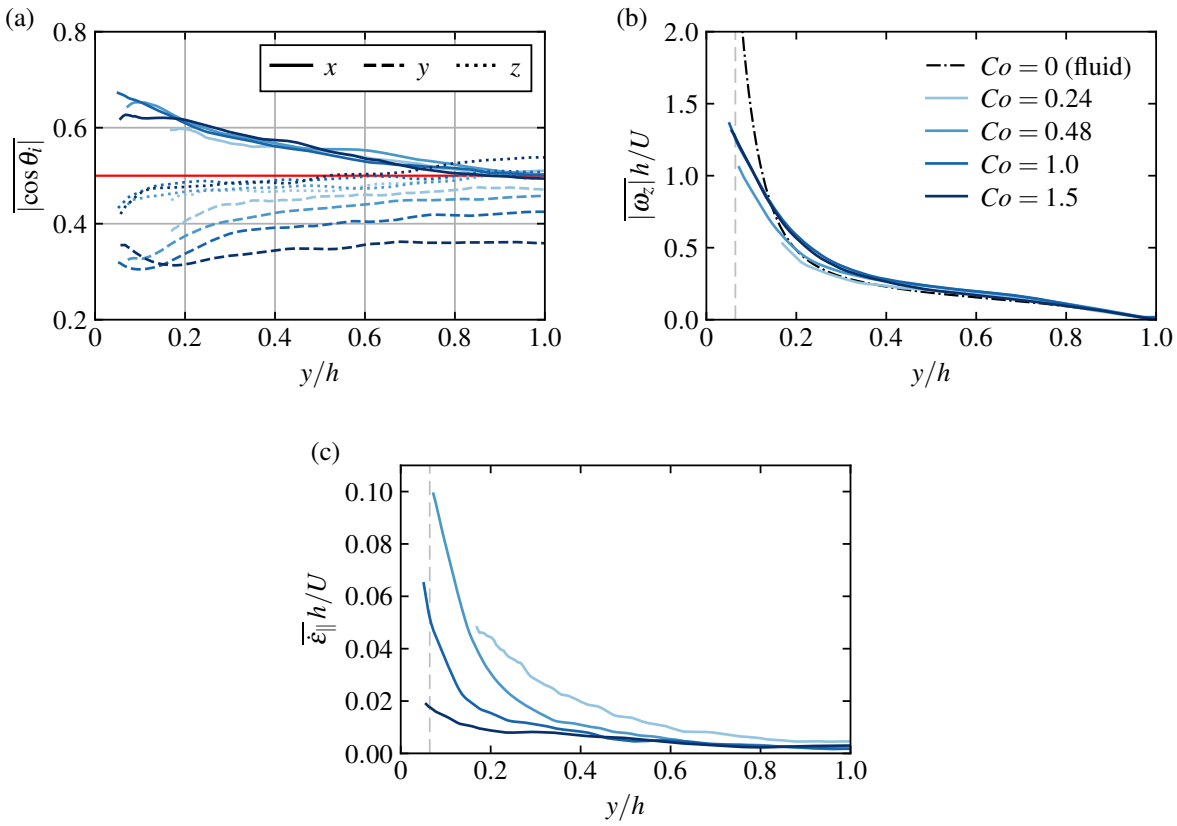


Figure 7.7: Wall-normal profiles of: (a) Orientation angle of the aggregate longest axis with respect to the domain frame of reference, equation 7.8, (b) the angular velocity of aggregates about the spanwise axis, z, (c) mean rate of strain along the aggregate long axis. Each figure only considers aggregates with $n > 2$ and wall-normal bins with $\phi > 10^{-3}$ to avoid singularities in particle phase conditioned statistics.

exceptionally well, with slip apparent only in close proximity to the wall, $y \lesssim$. No significant mean rotation is observed about the wall-normal or streamwise axes, which are not reported here since $\overline{|\omega_x^A|} \approx \overline{|\omega_y^A|} \approx 0$.

Given that aggregates rotate and become preferentially aligned with the streamwise direction near the wall, an appropriate deformation measure is the rate of strain along $\boldsymbol{e}_j^A$. Computed following the methodology in appendix E, the axial rate of strain, $\dot{\varepsilon}_\parallel$, is averaged in the same manner as the orientation and reported in figure 7.7(c). A positive $\dot{\varepsilon}_\parallel$ indicates axial extension, while negative values denote compression.

The mean profiles $\overline{\dot{\varepsilon}_\parallel}(y)$ are shown in figure 7.7(c) for each Co. Aggregates are extended near the wall at every Co, with the extensional straining increasing monotonically on approach to the wall. The apparent decrease of $\overline{\dot{\varepsilon}_\parallel}$ very close to the wall at $Co = 0.24$ reflects the scarcity of aggregates of size $n > 2$ there, rather than a change in mechanism.

The mean profiles $\overline{\dot{\varepsilon}_\parallel}(y)$ are shown in figure 7.7(c) for each Co. Aggregates are extended near the wall at every Co, with the extensional straining increasing monotonically on approach to the wall, where breakup is most prominent. Satisfactorily, the magnitude of $\overline{\dot{\varepsilon}_\parallel}$ decreases monotonically with Co at fixed y and reflects that stronger cohesion makes aggregates stiffer so that a given shear rate yields less axial stretching. This is consistent with the observations of near-wall breakup mechanisms in figure 7.6 where collision and lubrication forces were found to increasingly contribute to breakup relative to the shear at high Co.

Together, these mechanistic observations corroborate the statistical interpretation: breakup is facilitated in the near wall region, where a mixture of hydrodynamic, lubrication, and collisional forces facilitate aggregate deformation and breakup. More cohesive aggregates (higher Co) are deformed less at a given wall-normal location and therefore must travel closer to the wall before breaking, consistent with the contraction of the y-span of region 1 with increasing Co observed in figure 7.5.

This analysis is a first interrogation of the mechanisms sustaining the newly framed statistical circulation in (n, y) space. A predictive account requires the full wall-normal and size dependence of the PBE kernels themselves, together with their scaling with local flow quantities; a substantial task that is left to future work.

7.5 Summary

During statistical equilibrium, aggregation and breakup balance globally within the domain. The nature of this balance is explored by probing the net aggregation and breakup source and sinks $\overline{\overline{T}}_a$ and $\overline{\overline{T}}_b$ across sizes n. At low Co breakup behaves exclusively as a sink, and aggregation a source, for sizes $n > 1$ indicating that all aggregates favorably break. As Co is increased, an intermediate region appears in which breakup from larger sizes acts as a source and aggregation a sink. The development of this intermediate region is summarized in the phase diagram in figure 7.2 and is further shown to coincide with the development of a log-normal mass-weighted aggregate number density.

While globally balanced, aggregation and breakup need not balance locally in the wall-normal direction. Indeed, taking the plane and time averaged PBE reveals the presence of regions in (n, y)-space of net aggregate production and depletion. This imbalance is shown to be sustained by the wall-normal advection of aggregates, with smaller aggregates generally traveling to the channel center, where they aggregate, and larger aggregates traveling to the channel wall, where they break.

The near-wall breakup mechanisms that drive this circulation are directly interrogated. Perhaps surprisingly, collisions and lubrication interactions with the wall are shown to have a minimal effect. Indeed aggregates appear instead to rotate and align with the streamwise direction near the wall, where they then experience extensional straining along their long axis, leading to breakup.

Chapter 8

Concluding remarks[1]

8.1 Summary

In this work, we have brought forward eight PR-DNS simulations of a turbulent channel flow laden with finite-sized cohesive particles. The strength of the cohesive force, characterized by the cohesion number Co, is systematically varied across six of the cases, $Co = \{0, 0.12, 0.24, 0.48, 1.0, 1.5\}$.

Upon release, the initially randomly dispersed cohesive particles form aggregates, break, and redistribute, until a statistically stationary population is maintained. This initial period of aggregate growth, termed the *flocculation* period, is analyzed in chapter 5, where we demonstrate that the single-class flocculation model of Winterwerp [5] reasonably captures the evolution of the mean aggregate size over time. The model also performs well when extended across the wall-normal direction, provided the local

[1]This chapter contains previously published work, adapted here with minor modifications from the following references: A. D. Leonelli and Meiburg, E. (2026). *Turbulent Channel Flow with Cohesive Particles*, *Proceedings of the 14th International Symposium on Turbulence and Shear Flow Phenomena*. Heidelberg, Germany. & A. D. Leonelli, L. Widmer, and E. Meiburg, *Aggregation, breakup, and size-dependent transport in a turbulent channel flow with cohesive particles*, 2026. Under review at *J. Fluid Mech.* at the time of dissertation submission.

turbulent shear rate is used in place of the global shear rate.

The subsequent statistically stationary *equilibrium* period is interrogated in chapter 6. As expected, higher Co yields larger aggregates and a broader aggregate size distribution. These larger aggregates are shown to modulate the underlying turbulence, with Reynolds stresses generally trending back toward their single-phase profiles as Co increases. Consistent with this, we report a small drag reduction at higher Co relative to the cohesionless case, which is explained by the removal of a highly-dissipative wall-adjacent layer of particles at higher Co. Overall, however, flow modulation remains minimal, a consequence of the low particle volume fraction and neutral buoyancy of the particles used here. Despite this, the fluctuations of the particle phase are significantly modulated by Co, reflecting the growth of large inertial aggregates.

As summarized above, unlike sub-Kolmogorov scale particles or aggregates, the finite-size nature of the structures considered in this work present size-dependent kinematics, likely due to spatial filtering, where larger aggregates effectively filter out relatively smaller scales and kinematically respond only to similar- or larger-scale flow structures [129]. As a result, the flocculation rate may be lower due to the associated reduction in fluctuations, as reported in figure 6.3. However, the statistics measured in this work are insufficient to further investigate this, and direct evidence for size-dependent filtering is left as a subject of future work.

The coupling between the aggregates and the carrier flow also deserves closer attention than was given here, particularly in light of the preferential streamwise alignment of aggregates near the wall reported in chapter 7. Such alignment effects have been shown to have dramatic effects on turbulent statistics, including wall shear stress, for other anisotropic particles such as fibers and spheroids [135, 136]. Though not significant in the present study, such effects should become important for heavier particles or smaller primary particles, where aggregates may elongate substantially before breaking.

Particle data is stored at high frequency for a subset of five simulations with $\rho_s = 1$ and $Co = \{0, 0.24, 0.48, 1.0, 1.5\}$. This high temporal fidelity allows for a full reconstruction of the aggregate lineage across aggregation and breakup events, as described in chapter 4, which in turn permits a PBE-based analysis framework to be employed. Doing so allows the bulk aggregation and breakup rates to be reported in chapter 6, where it is shown that the breakup rate scales with the aggregate surface area D^2. While the aggregation rate is shown to nontrivial, the parent-child size distributions for both aggregation and breakup are found to be U-shaped, indicating that most events involve small-large aggregate pairs.

Near the wall, aggregates are found to align with the flow, with rotation rates closely tracking those of the fluid. They are also shown to undergo increasingly rapid extension along their long axis on approach to the wall, where breakup is prominent. Classifying breakup events by closest approach to the wall shows that, at low Co, direct contact and lubrication modeling do not alter the outcome (aggregation or breakup) of a near-wall encounter relative to hydrodynamic forces alone. For the strongest cohesion, $Co = 1.5$, however, it does, consistent with the reduced deformability of strongly cohesive aggregates. The breakup of larger aggregates in this near-wall region results in an excess supply of small aggregates that must be removed if equilibrium is to be maintained, a fate that can be tracked statistically with the PBE.

Exploiting the PBE analytically, we show that aggregation and breakup must balance globally, since together they conservatively redistribute mass across sizes. Nontrivially, however, they need not balance locally in the wall-normal direction. Equilibrium is instead maintained through spatially separated regions of net aggregate production and depletion; closure of the PBE is recovered with the inclusion of size-dependent wall-normal advective transport. Viewed in (n, y)-space, these regions organize into a closed statistical cycle: small aggregates are produced in abundance near the wall, advected to-

wards the channel center where they grow through aggregation, transported back toward the wall, and subsequently broken down, re-entering the cycle.

8.2 Outlook

8.2.1 PR-DNS and Euler-Lagrange simulations

In this work we have developed a toolbox for the analysis of cohesive particle dynamics in numerical simulations. A wide range of questions in which this framework can provide insight still remain. Importantly, this toolbox is independent of the underlying numerical approach. The PR-DNS methodology used throughout this work directly resolves the flow around each particle, making it well suited to problems where accurately capturing the near-particle hydrodynamics is essential. This fidelity comes at a significant computational cost, however, limiting the accessible range of particle number and size, domain size, and Reynolds number. Consequently, the extension of this work falls into two categories, based on methodology: problems that can continue to exploit the fidelity of PR-DNS, and those that instead require the reduced computation cost of Euler-Lagrange (EL) simulation.

The present PR-DNS approach can be exploited further in several directions. First, the present work is restricted to dilute suspensions; extending this to higher volume fractions would connect the PBE framework developed here to percolation theory and clogging, and provide insight into the transition from a cohesive suspension to a system-spanning network of aggregates. The high fidelity of PR-DNS can also be used to characterize the drag on aggregates of varying size, cohesion, and shape, informing closure models for the drag laws required in EL simulations of cohesive particles. Finally, the PBE analysis here focused on neutrally buoyant particles. Substituting for heavier par-

ticles and introducing gravity would therefore enable investigation of aggregate settling, deposition, and subsequent erosion processes central to sediment transport and biofilm removal applications.

Due to computational costs, however, PR-DNS frameworks are limited in scale, and several critical extensions of this work instead call for EL simulations. Investigations at higher Reynolds numbers, supporting a well-developed inertial range, together with smaller, sub-Kolmogorov-scale, primary particles, would yield the separation of scales required to develop application-relevant scaling laws. This separation of scales would in turn allow EL simulations to directly probe how aggregation and breakup couple to the Kolmogorov-Richardson energy cascade which would require aggregates whose size falls within the intertial subrange.

8.2.2 Beyond PBE models

Ultimately, the toolbox developed in this work serves as a foundation for broader study into the aggregation and breakup of cohesive particles. The work presented here is primarily limited by scale; with large primary particles relative to the Kolmogorov length scale, $d/\eta = 11.6$, and a low Reynolds number, $Re_\tau = 180$ yielding little separation of scales. In application the separation of scales is vast, with aggregates typically order micro-to-millimeter, Kolmogorov scales in the milli- to centimeters, and Reynolds number orders of magnitude larger.

Experiment can reach closer into these parameter ranges but are unfortunately lacking. This is true for cohesionless particles as well, where PR-DNS currently outpaces experimental work leaving validation often only against other PR-DNS. How far, if at all, such recursive validation has deviated from reality is unknown, though the deviation is likely small. Still, application of frameworks such as the one discussed here to

experimental data would be highly valuable. Some progress has been made, especially in bubbly flows [137, and references therein], and to a lesser extent in cohesive particulate systems [72, 134]. Though the area remains poor in experimental data.

Despite their emphasis in this work, population balance models are entirely computationally prohibitive at industrial and field-scale applications [57, 25]. The core difficulty is that evaluating the PBE kernels scales with the number of classes, n_c, as $\mathcal{O}(n_c^2)$. In large-scale systems targeted for modeling, aggregate size distributions can span several orders of magnitude [59], forcing resolution and predictive accuracy to be traded for tractability [62] (the same challenge is faced in droplet-laden [63] and bubbly flows [65]).

To address this, novel cohesive sediment models are required, the development of which is dependent on improving the current understanding of the fundamental mechanisms and coupling between the turbulent flow field and aggregation and breakup dynamics. Ultimately, a continuum closure model capable of accurately evolving the size distribution in Euler-Euler or Euler-Lagrange numerical frameworks such as DELFT3D [138], ROMS [60]) would be attractive.

Rather than continuing to pursue PBE closures, sediment transport models may be able to derive inspiration from fundamental theoretical contributions to bubbly and droplet laden flows. Prime for this is the work of Chan et al. [139, 65], who who formalized the Kolmogorov-Hinze (KH) breakup cascade, to describe the evolution of bubble size distributions under breaking waves, enabling LES-like closure models for the PBE. While a direct analog for cohesive materials is unlikely exploiting the PBE toolkit developed in this work for the evaluation of PBE statistics in flows with increased separation of scales would allow for proper investigation into the interactions of aggregates with the inertial range of turbulence.

Appendix A

Slip velocity

The slip velocity between particle and fluid is computed by taking the mean fluid velocity within a shell of radius $R = d/2 + 3\Delta x$ centered at particle i,

$$\boldsymbol{u}_i^F(t) = \frac{\displaystyle\int_0^R \int_0^{2\pi} \int_0^{\pi} \boldsymbol{u}(\boldsymbol{x}_i^P(t) + \boldsymbol{r}, t)\, \xi_f(\boldsymbol{x}_i^P(t) + \boldsymbol{r}, t)\, r^2 \sin\theta_s \,\mathrm{d}r \,\mathrm{d}\theta_s \,\mathrm{d}\phi_s}{\displaystyle\int_0^R \int_0^{2\pi} \int_0^{\pi} \xi_f(\boldsymbol{x}_p(t) + \boldsymbol{r}, t)\, r^2 \sin\theta_s \,\mathrm{d}r \,\mathrm{d}\theta_s \,\mathrm{d}\phi_s}, \tag{A.1}$$

where $\boldsymbol{r} = \boldsymbol{r}(r, \theta_s, \phi_s)$ denotes the position vector, in spherical coordinates, relative to $\boldsymbol{x}_i^P$. Here, the fluid indicator function ξ_f,

$$\xi_f(\boldsymbol{x}, t) = \begin{cases} 0 & \text{if inside a particle,} \\ 1 & \text{otherwise,} \end{cases} \tag{A.2}$$

ensures that no fluid from inside the fictitious domain within particles is included in the estimate for $\boldsymbol{u}_i^F$. The slip velocity for a particle i is then given by $\Delta\boldsymbol{u}_i^{PF} = \boldsymbol{u}_i^P - \boldsymbol{u}_i^F$ which is then used to estimate the particle Reynolds number, $Re_{p,i} = \Delta\boldsymbol{u}_i^{PF} d/\nu$. In figure A.1, the PDF of Re_p accumulates $Re_{p,i}$ for each case averaged over all particles and T_{eq}.

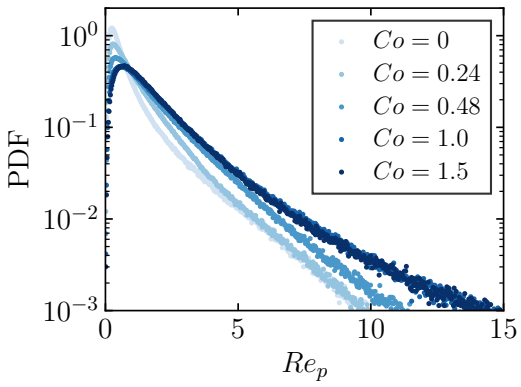


Figure A.1: Probability density distributions of particle Reynolds number Re_p measured over all aggregates in the sampling period T_{eq} for each Co.

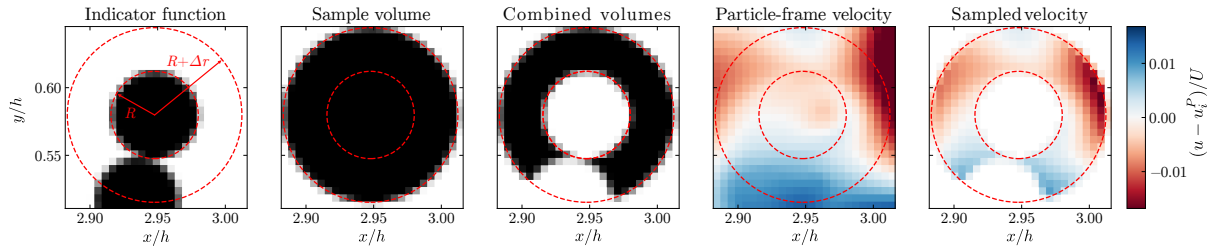


Figure A.2: Graphical summary of the procedure to compute the particle-fluid slip velocity.

Expectedly, the highest Re_p are observed for the largest Co due to the creation of larger aggregates. The maximum $Re_{p,i}$ over all cases occurs for $Co = 1.5$ and is estimated as $\max_i Re_{p,i} = 49.58$, which is the value used in section 3.1 to estimate the minimum particle boundary layer thickness. The above steps are summarized visually in figure A.2.

Appendix B

Family tree

Aggregates are independently identified at every stored snapshot. A family tree is then generated by matching the constituent primary particles between snapshots according to the rules presented in chapter 4. Due to the ability to fully resolve the constituent particle kinematics, we only consider binary aggregation and breakup events in this work, and consider all other events as "missed" binary events. The identification rate of each type of event is reported in Table B.1 where is is shown that less than 1% of events are missed over all cases.

Case	Resolved agg.	Resolved break.	Missed agg.	Missed break.	% missed agg.	% missed break.
$Co = 0$	3431	3426	7	11	0.20	0.32
$Co = 0.24$	14713	14727	68	82	0.46	0.56
$Co = 0.48$	26767	26641	161	247	0.60	0.93
$Co = 1.0$	4746	4707	21	30	0.44	0.64
$Co = 1.5$	1610	1621	9	11	0.56	0.68

Table B.1: Aggregation and breakup event detections. Missed events are either non-binary or complex as defined in section B.

Appendix C

Correlation time and error estimation

Statistical uncertainty is reported in the main text using a 95% confidence interval. To compute these intervals the number of independent snapshots, N_{eff}, taken over the sampling period for each Co case is first estimated, then used to compute the standard error.

The statistical interpretation of turbulence is strictly based on ensemble averages, where each snapshot is independent. This is impractical in many turbulent flows as lead time can be costly. Instead, Taylor's hypothesis is invoked and sample independence is justified using the correlation times of fluid properties such as the streamwise velocity fluctuations. In this work, we must additionally quantify timescales related to the rearrangement of aggregate populations so that the number of independent samples of the aggregate number density and related quantities can be estimated. To do so, we evaluate the autocorrelation of the fluctuations of the global mass-weighted aggregate number

density $\widetilde{\widetilde{nf}}(n,t)$. The fluctuations are then,

$$\widetilde{\widetilde{nf}}'(n,t) = \widetilde{\widetilde{nf}}(n,t) - \overline{\overline{nf}}(n). \tag{C.1}$$

C.1 Global autocorrelation and correlation time

We are interested in the fluctuations of the distribution as a whole and therefore define the global autocorrelation as,

$$C(s) = \frac{\sum_n \left\langle \widetilde{\widetilde{nf}}'(n,t)\widetilde{\widetilde{nf}}'(n,t+s) \right\rangle}{\sum_n \left\langle \widetilde{\widetilde{nf}}'(n,t)\widetilde{\widetilde{nf}}'(n,t) \right\rangle}. \tag{C.2}$$

Due to their abundance, this formulation is dominated by the statistics for $n = 1$ aggregates. However, the $n = 1$ population is generally observed to have the longest correlation times and so we take this as a suitable conservative estimate. The resulting $C(s)$ are plotted for every case in figure C.1. The correlation time,

$$t_{int} = \int_0^{t_0} C(s)\,\mathrm{d}s, \tag{C.3}$$

quantifies the rate of relaxation of $C(s)$ and is shown as a vertical dashed line for each case. Here, t_0 is the first zero crossing of $C(s)$, which is taken as the upper limit of integration to avoid integration of random noise at large s.

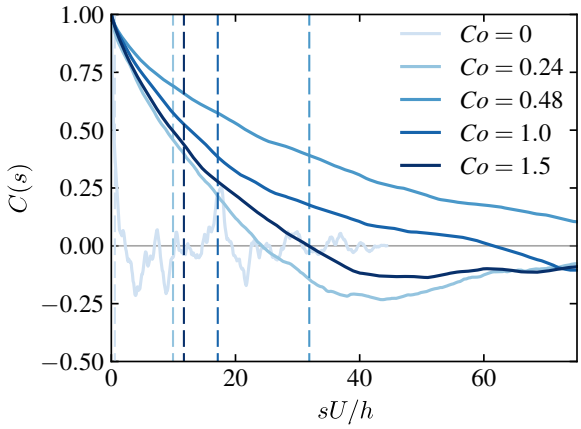


Figure C.1: Global autocorrelation as defined by equation (C.2) for all Co. The correlation time, t_{int}, is plotted as a vertical dashed line of matching color for each case.

C.2 Number of samples and error estimation

The number of independent samples is estimated by dividing the total sampling period for each case T by $2t_{int}$,

$$N_{eff} = \frac{T}{2t_{int}}, \tag{C.4}$$

where the factor of 2 follows from the standard relationship between the integral autocorrelation time and the effective number of statistically independent samples in a stationary process. The number of independent samples is reported in table C.1 alongside the correlation times and sampling periods.

To estimate the uncertainty on a measurement such as the aggregate number density $\overline{\overline{nf}}(n)$ we quantify the variance $\mathrm{Var}[nf(n,t)]$ and compute a standard error,

$$SE = c_{95}\sqrt{\frac{\mathrm{Var}[nf(n,t)]}{N_{eff}}}, \tag{C.5}$$

where c_{95} is the prefactor for a 95% confidence interval. Given by the two-tailed critical value of the Student's t-distribution with $N_{eff} - 1$ degrees of freedom, $c_{95} = t_{0.975,\,N_{eff}-1}$.

Co	T_{eq}	T_{sub}	t_{int}	$N_{eff,eq}$	$N_{eff,sub}$	$c_{95,sample}$	$c_{95,sub}$
0	708.43	44.37	0.57	618	39	1.96	2.02
0.24	987.83	183.78	9.94	50	10	2.01	2.26
0.48	1053.34	480.68	31.88	17	8	2.12	2.36
1.0	501.94	249.60	17.14	15	8	2.14	2.36
1.5	439.40	238.82	11.69	19	11	2.10	2.23

Table C.1: Timing statistics results and error prefactors.

This choice accounts for the fact that N_{eff} is small for several cases (as low as 8), where the Gaussian approximation $c_{95} \approx 1.96$ underestimates the true interval width.

Appendix D

PBE fluxes, expanded

Figure 7.4 in chapter 7 presents the wall-normal profile of the net source due to aggregation and breakup $\overline{Q}(y)$ with the data for the individual net source and sink terms due to aggregation and breakup $\overline{T_a}$ and $\overline{T}_b$ cut from view due to the section's focus on $\overline{Q}$. Here, we show the full range of data in figure D.1.

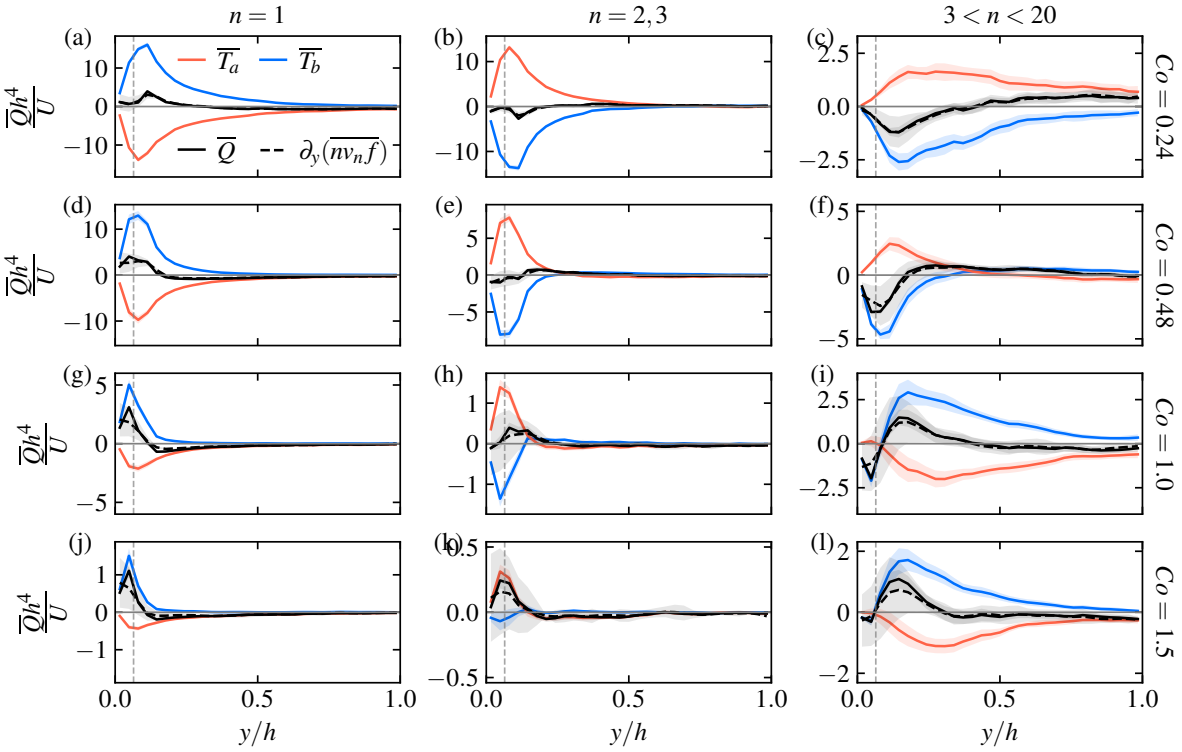


Figure D.1: The net source due to aggregation and breakup, $\overline{Q}$, aggregation $\overline{T_a}$, breakup $\overline{T_b}$, and advective flux $\partial_y(\overline{nv_n f})$ for three size classes: $n = 1$, $n \in \{2, 3\}$, and $3 < n < 20$ (columns) for $Co > 0$ (rows) plotted over the half channel height, $y/h \in [0, 1]$. A 95% confidence interval is shown by the shaded region surrounding each curve. The gray vertical dashed line corresponds to $y = d$.

Appendix E

Aggregate orientation

We take the long axis of an aggregate j, $\boldsymbol{e}_j^A$ to be the unit principal eigenvector of the gyration tensor,

$$\mathcal{G}_j = \frac{1}{n_j} \sum_{i=1}^{n_j} \boldsymbol{r}_i^{PA} \left(\boldsymbol{r}_i^{PA}\right)^T, \tag{E.1}$$

where $\boldsymbol{r}_i^{PA} = \boldsymbol{x}_i^P - \boldsymbol{x}_j^A$ is the position of particle i relative to the center of mass of its host aggregate j, $\boldsymbol{x}_j^A$. Since the sign of an eigenvector is arbitrary, the orientation is calculated using

$$\cos\theta_{i,j} = \left|\hat{\boldsymbol{e}}_i \cdot \boldsymbol{e}_j^A\right|, \qquad i \in \{x, y, z\}, \tag{E.2}$$

To then compute the rate of strain along $\boldsymbol{e}_j^A$, first, the position and velocity of each constituent particle is projected onto the axis, $r_{\parallel,ij} = \boldsymbol{r}_i^{PA} \cdot \boldsymbol{e}_j^A$ and $u_{\parallel,ij} = \boldsymbol{u}_i^P \cdot \boldsymbol{e}_j^A$. We next define the least-squares estimate of the axial velocity gradient across the aggregate,

$$\dot{\varepsilon}_{\parallel,j} = \frac{\sum_i u_{\parallel,ij} r_{\parallel,ij}}{\sum_i r_{\parallel,ij}^2} \tag{E.3}$$

for $i \in \mathcal{A}_j$ where $\mathcal{A}_j$ is the subset of particles in aggregate j. Here, positive $\dot{\varepsilon}_\parallel$ indicates axial extension and negative values axial compression.

Appendix F

Breakup mechanism windowing sensitivity

The cause of breakup in section 7.3 is determined based on an aggregate's closest approach to the wall in a window t_{win} before its time of death, $t_{d,j}$. In the main text $t_{win} = h/U$. Here we plot the breakup ratio Φ_b as defined in section 7.3 for each mechanism (collision, lubrication, hydrodynamic) as a function of t_{win} in figures F.1(a-c). Over all Co it is clear that Φ_b is relatively insensitive to t_{win} so long as $t_{win} \gtrsim 0.5h/U$. The selected value of $t_{win} = h/U$ is shown as a vertical red line in figures F.1(a-c).

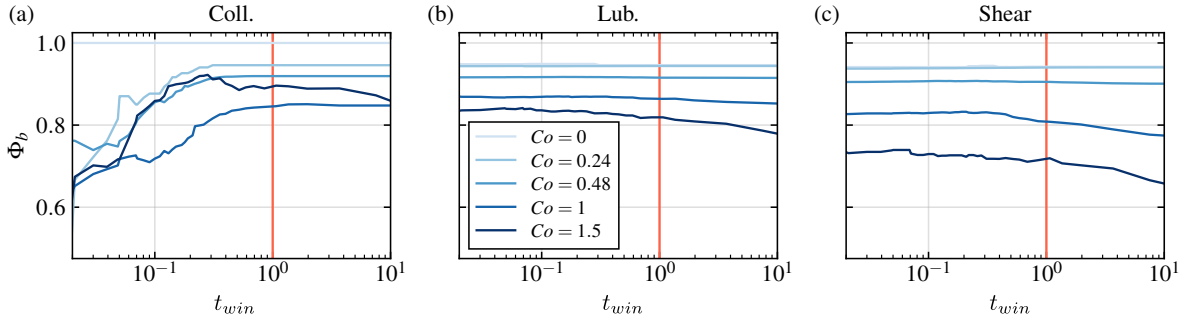


Figure F.1: Breakup fraction Φ_b as a function of cutoff time t_{win}. The selected $t_{win} = h/U$ used in section 7.3 is shown as a vertical red line.

Bibliography

[1] J. C. Winterwerp and W. van Kesteren, *Introduction to the Physics of Cohesive Sediment in the Marine Environment*, vol. 56 of *Developments in Sedimentology*. Elsevier, 2004.

[2] M. V. Smoluchowski, *Drei Vortrage uber Diffusion, Brownsche Bewegung und Koagulation von Kolloidteilchen*, *Phys. Z.* **17** (1916) 557–585.

[3] M. V. Smoluchowski, *Versuch einer mathematischen theorie der koagulationskinetik kolloider lösungen.*, *Z. Phys. Chem.* **92** (1918) 129–168.

[4] M. Lee and R. D. Moser, *Direct numerical simulation of turbulent channel flow up to $Re_\tau \approx 5200$*, *J. Fluid Mech.* **774** (2015) 395–415.

[5] J. C. Winterwerp, *A simple model for turbulence induced flocculation of cohesive sediment*, *J. Hydraul. Res.* **36** (1998), no. 3 309–326.

[6] J. Gregory and C. R. O'Melia, *Fundamentals of flocculation*, *Crit. Rev. Environ. Control* **19** (1989), no. 3 185–230.

[7] A. J. Mehta, *An introduction to hydraulics of fine sediment transport (Second edition)*. Developments in Sedimentology. World Scientific Publishing Co. Pte. Ltd., 2023.

[8] A. L. Alldredge and M. W. Silver, *Characteristics, dynamics and significance of marine snow*, *Prog. Oceanogr.* **20** (1988), no. 1 41–82.

[9] J. C. Winterwerp, *On the flocculation and settling velocity of estuarine mud*, *Cont. Shelf Res.* **22** (2002), no. 9 1339–1360.

[10] B. Vowinckel, J. Withers, P. Luzzatto-Fegiz, and E. Meiburg, *Settling of cohesive sediment: particle-resolved simulations*, *J. Fluid Mech.* **858** (2019) 5–44.

[11] E. D. Ongley, B. G. Krishnappan, I. G. Droppo, S. S. Rao, and R. J. Maguire, *Cohesive sediment transport: emerging issues for toxic chemical management*, *Hydrobiologia* **235** (1992), no. 1 177–187.

[12] Z. Deng, Q. He, Z. Safar, and C. Chassagne, *The role of algae in fine sediment flocculation: In-situ and laboratory measurements*, *Mar. Geol.* **413** (2019) 71–84.

[13] N. Wu, S. W. D. Grieve, A. J. Manning, and K. L. Spencer, *Flocs as vectors for microplastics in the aquatic environment*, *Nat. Water* **2** (2024), no. 11 1082–1090.

[14] H. G. Smith, G. J. Sheridan, P. N. J. Lane, P. Nyman, and S. Haydon, *Wildfire effects on water quality in forest catchments: A review with implications for water supply*, *J. Hydrol.* **396** (2011), no. 1-2 170–192.

[15] T. Leiknes, *The effect of coupling coagulation and flocculation with membrane filtration in water treatment: A review*, *J. Environ. Sci.* **21** (2009), no. 1 8–12.

[16] A. K. Verma, R. R. Dash, and P. Bhunia, *A review on chemical coagulation/flocculation technologies for removal of colour from textile wastewaters*, *J. Environ. Manage.* **93** (2012), no. 1 154–168.

[17] G. Grant and W. Tabakoff, *Erosion prediction in turbomachinery resulting from environmental solid particles*, *J. Aircraft* **12** (1975), no. 5 471–478.

[18] A. B. D. Nandiyanto and K. Okuyama, *Progress in developing spray-drying methods for the production of controlled morphology particles: From the nanometer to submicrometer size ranges*, *Adv. Powder Technol.* **22** (2011), no. 1 1–19.

[19] A. Sosnik and K. P. Seremeta, *Advantages and challenges of the spray-drying technology for the production of pure drug particles and drug-loaded polymeric carriers*, *Adv. Colloid Interface Sci.* **223** (2015) 40–54.

[20] J. Yang, C.-Y. Wi, and M. Adams, *Dem analysis of particle adhesion during powder mixing for dry powder inhaler formulation development*, *Granul. Matter* **15** (2013), no. 4 417–426.

[21] J. Yang, C.-Y. Wi, and M. Adams, *Numerical modelling of agglomeration and deagglomeration in dry powder inhalers: a review*, *Curr. Pharm. Des.* **21** (2015), no. 40 5915—5922.

[22] Z. Tong, B. Zheng, R. Yang, A. Yu, and H.-K. Chan, *Cfd-dem investigation of the dispersion mechanisms in commercial dry powder inhalers*, *Powder Technol.* **240** (2013) 19–24.

[23] Z. Tong, W. Zhong, A. Yu, H.-K. Chan, and R. Yang, *Cfd–dem investigation of the effect of agglomerate–agglomerate collision on dry powder aerosolisation*, *J. Aerosol Sci.* **92** (2016) 109–121.

[24] M. Hoppentocht, P. Hagedoorn, H. W. Frijlink, and A. H. de Boer, *Technological and practical challenges of dry powder inhalers and formulations*, *Adv. Drug Deliv. Rev.* **75** (2014) 18–31.

[25] X. Yu, S. Balachandar, J. Smith, and A. J. Manning, *Flocculation Dynamics of Cohesive Sediment in Turbulent Flows Using CFD-DEM Approach*, in *Sediment Transport Research - Further Recent Advances*. IntechOpen, Apr., 2024.

[26] H. C. Hamaker, *The london–van der waals attraction between spherical particles*, *Physica* **4** (1937), no. 10 1058–1072.

[27] J. N. Israelachvili, *Intermolecular and Surface Forces*. Academic Press, Burlington, MA, 3 ed., 2011.

[28] L. Bocquet, E. Charlaix, S. Ciliberto, and J. Crassous, *Moisture-induced ageing in granular media and the kinetics of capillary condensation*, *Nature* **396** (1998), no. 6713 735–737.

[29] T. C. Halsey and A. J. Levine, *How sandcastles fall*, *Phys. Rev. Lett.* **80** (1998), no. 14 3141.

[30] H.-C. Flemming and J. Wingender, *The biofilm matrix*, *Nat. Rev. Microbiol.* **8** (2010), no. 9 623–633.

[31] N. Gravish, S. V. Franklin, D. L. Hu, and D. I. Goldman, *Entangled granular media*, *Phys. Rev. Lett.* **108** (May, 2012) 208001.

[32] S. V. Franklin, *Geometric cohesion in granular materials*, *Physics Today* **65** (2012), no. 9 70–71.

[33] R. J. Brown, C. Bonadonna, and A. J. Durant, *A review of volcanic ash aggregation*, *Physics and Chemistry of the Earth, Parts A/B/C* **45-46** (2012) 65–78.

[34] A. J. Manning and K. R. Dyer, *Mass settling flux of fine sediments in northern european estuaries: Measurements and predictions*, *Mar. Geol.* **245** (2007), no. 1 107–122.

[35] M. Afkhami, A. Hassanpour, M. Fairweather, and D. Njobuenwu, *Fully coupled LES-DEM of particle interaction and agglomeration in a turbulent channel flow*, *Comput. Chem. Eng.* **78** (2015) 24–38.

[36] N. Almohammed and M. Breuer, *Modeling and simulation of agglomeration in turbulent particle-laden flows: A comparison between energy-based and momentum-based agglomeration models*, *Powder Technol.* **294** (2016) 373–402.

[37] J. Hærvig, K. Sørensen, and T. Condra, *Early stages of agglomeration of adhesive particles in fully-developed turbulent pipe flows*, *Int. J. Multiph. Flow* **106** (2018) 254–267.

[38] D. O. Njobuenwu and M. Fairweather, *Large eddy simulation of particle agglomeration with shear breakup in turbulent channel flow*, *Phys. Fluids* **30** (2018), no. 6 063303.

[39] K. C. J. Schutte, L. M. Portela, A. Twerda, and R. A. W. M. Henkes, *Formation and break-up of rigid agglomerates in turbulent channel and pipe flows*, *J. Fluid Mech.* **857** (2018) 539–561.

[40] K. Zhao, F. Pomes, B. Vowinckel, T.-J. Hsu, B. Bai, and E. Meiburg, *Flocculation of suspended cohesive particles in homogeneous isotropic turbulence*, *J. Fluid Mech.* **921** (2021) A17.

[41] A. Leonelli and E. Meiburg, *On the effects of anisotropy on the flocculation of cohesive particles in turbulence*, *Acta Mech.* **237** (2026), no. 4 1699–1713.

[42] A. D. Leonelli, L. Widmer, and E. Meiburg, *Aggregation, breakup, and size-dependent transport in a turbulent channel flow with cohesive particles*, 2026. Under review at J. Fluid Mech.

[43] K. J. Ives and A. G. Bhole, *Theory of flocculation for continuous flow system*, *J. Environ. Eng. Div., Am. Soc. Civ. Eng.* **99** (1973), no. 1.

[44] F. Maggi, F. Mietta, and J. C. Winterwerp, *Effect of variable fractal dimension on the floc size distribution of suspended cohesive sediment*, *J. Hydrol.* **343** (2007), no. 1-2 43–55.

[45] F. Xu, D.-P. Wang, and N. Riemer, *Modeling flocculation processes of fine-grained particles using a size-resolved method: Comparison with published laboratory experiments*, *Cont. Shelf Res.* **28** (2008), no. 19 2668–2677.

[46] M. Son and T.-J. Hsu, *The effects of flocculation and bed erodibility on modeling cohesive sediment resuspension*, *J. Geophys. Res.* **116** (2011), no. C3 C03021.

[47] Z. Yang, H. Yang, Z. Jiang, X. Huang, H. Li, A. Li, and R. Cheng, *A new method for calculation of flocculation kinetics combining Smoluchowski model with fractal theory*, *Colloids Surf. A Physicochem. Eng. Asp.* **423** (2013) 11–19.

[48] H. Shin, M. Son, and G. Lee, *Stochastic Flocculation Model for Cohesive Sediment Suspended in Water*, *Water* **7** (2015), no. 5.

[49] H. Lai, H. Fang, L. Huang, G. He, and D. Reible, *A review on sediment bioflocculation: Dynamics, influencing factors and modeling*, *Sci. Total Environ.* **642** (2018) 1184–1200.

[50] X. Shen, B. J. Lee, M. Fettweis, and E. A. Toorman, *A tri-modal flocculation model coupled with telemac for estuarine muds both in the laboratory and in the field*, *Water Res.* **145** (2018) 473–486.

[51] Y. Chou, K. S. Nelson, R. C. Holleman, O. B. Fringer, M. T. Stacey, J. R. Lacy, S. G. Monismith, and J. R. Koseff, *Three-Dimensional Modeling of Fine Sediment Transport by Waves and Currents in a Shallow Estuary*, *J. Geophys. Res. Oceans* **123** (2018), no. 6 4177–4199.

[52] L. Ye, M. Huang, H. Liu, J. Gu, and J. Wu, *Flocculation under combined effects of hydrodynamic and subaqueous biomass in the bottom boundary layer (BBL) of a microtidal estuary*, *Sci. Total Environ.* **913** (2024) 169660.

[53] J. A. Penaloza-Giraldo, L. Yue, T.-J. Hsu, B. Vowinckel, A. Manning, and E. Meiburg, *A Modeling framework for flocculated cohesive sediment transport in the current bottom boundary layer*, *Adv. Water Resour.* **195** (2025) 104857.

[54] J. A. Penaloza-Giraldo, L. Yue, T.-J. Hsu, B. Vowinckel, A. Manning, and E. Meiburg, *A numerical modeling framework for flocculation and cohesive sediment transport in the wave bottom boundary layer*, *J. Geophys. Res. Oceans* **130** (2025), no. 11 e2025JC022373.

[55] R. Hogg, *Flocculation and dewatering*, *Int. J. Miner. Process.* **58** (2000), no. 1-4 223–236.

[56] A. Khelifa and P. S. Hill, *Models for effective density and settling velocity of flocs*, *J. Hydraul. Res.* **44** (2006) 390–401.

[57] C. Chassagne and Z. Safar, *Modelling flocculation: Towards an integration in large-scale sediment transport models*, *Mar. Geol.* **430** (2020) 106361.

[58] V. G. Levich, *Physicochemical hydrodynamics*. Prentice Hall, Inc., 1962.

[59] M. Takeuchi, M. J. Doubell, G. A. Jackson, M. Yukawa, Y. Sagara, and H. Yamazaki, *Turbulence mediates marine aggregate formation and destruction in the upper ocean*, *Sci. Rep.* **9** (2019) 16280.

[60] C. R. Sherwood, A. L. Aretxabaleta, C. K. Harris, J. P. Rinehimer, R. Verney, and B. Ferré, *Cohesive and mixed sediment in the regional ocean modeling system (roms v3.6) implemented in the coupled ocean–atmosphere–wave–sediment transport modeling system (coawst r1234)*, *Geosci. Model Dev.* **11** (2018), no. 5 1849–1871.

[61] J. Liu, J.-H. Liang, K. Xu, Q. Chen, and C. E. Ozdemir, *Modeling sediment flocculation in langmuir turbulence*, *J. Geophys. Res. Oceans* **124** (2019), no. 11 7883–7907.

[62] J. A. Penaloza-Giraldo, T.-J. Hsu, A. J. Manning, L. Ye, B. Vowinckel, and E. Meiburg, *On the importance of temporal floc size statistics and yield strength for population balance equation flocculation model*, *Water Res.* **233** (2023) 119780.

[63] R. A. Shaw, *Particle-turbulence interactions in atmospheric clouds*, *Annu. Rev. Fluid Mech.* **35** (2003), no. 1 183–227.

[64] W. H. R. Chan, P. L. Johnson, and P. Moin, *The turbulent bubble break-up cascade. Part 1. Theoretical developments*, *J. Fluid Mech.* **912** (2021) A42.

[65] W. H. R. Chan, P. L. Johnson, P. Moin, and J. Urzay, *The turbulent bubble break-up cascade. Part 2. Numerical simulations of breaking waves*, *J. Fluid Mech.* **912** (2021) A43.

[66] C. Biggs, *Activated sludge flocculation: on-line determination of floc size and the effect of shear*, *Water Res.* **34** (2000), no. 9 2542–2550.

[67] D. Bouyer, A. Liné, and Z. Do-Quang, *Experimental analysis of floc size distribution under different hydrodynamics in a mixing tank*, *AIChE J.* **50** (2004), no. 9 2064–2081.

[68] W. He, J. Nan, H. Li, and S. Li, *Characteristic analysis on temporal evolution of floc size and structure in low-shear flow*, *Water Res.* **46** (2012), no. 2 509–520.

[69] L. Guérin, C. Coufort-Saudejaud, A. Liné, and C. Frances, *Dynamics of aggregate size and shape properties under sequenced flocculation in a turbulent Taylor-Couette reactor*, *J. Colloid Interface Sci.* **491** (2017) 167–178.

[70] R. Kuprenas, D. Tran, and K. Strom, *A Shear-Limited Flocculation Model for Dynamically Predicting Average Floc Size*, *J. Geophys. Res. Oceans* **123** (2018), no. 9 6736–6752.

[71] D. Saha, M. U. Babler, M. Holzner, M. Soos, B. Lüthi, A. Liberzon, and W. Kinzelbach, *Breakup of Finite-Size Colloidal Aggregates in Turbulent Flow Investigated by Three-Dimensional (3D) Particle Tracking Velocimetry*, *Langmuir* **32** (2016), no. 1 55–65.

[72] D. W. Hoffman and J. K. Eaton, *Experimental investigation of particle aggregation in a humid and turbulent environment*, *Int. J. Multiph. Flow* **163** (2023) 104423.

[73] D. Blaser, *Flocs in Shear and Strain Flows*, *J. Colloid Interface Sci.* **225** (2000), no. 2 273–284.

[74] M. Soos, A. S. Moussa, L. Ehrl, J. Sefcik, H. Wu, and M. Morbidelli, *Effect of shear rate on aggregate size and morphology investigated under turbulent conditions in stirred tank*, *J. Colloid Interface Sci.* **319** (2008), no. 2 577–589.

[75] M. L. Eggersdorfer, D. Kadau, H. J. Herrmann, and S. E. Pratsinis, *Fragmentation and restructuring of soft-agglomerates under shear*, *J. Colloid Interface Sci.* **342** (2010), no. 2 261–268.

[76] Y. M. Harshe, M. Lattuada, and M. Soos, *Experimental and modeling study of breakage and restructuring of open and dense colloidal aggregates*, *Langmuir* **27** (2011), no. 10 5739–5752.

[77] F. F. Dizaji, J. S. Marshall, and J. R. Grant, *Collision and breakup of fractal particle agglomerates in a shear flow*, *J. Fluid Mech.* **862** (2019) 592–623.

[78] F. Kleischmann, B. Vowinckel, E. Meiburg, and P. Luzzatto-Fegiz, *Long-term microgravity experiments reveal a new mechanism for particle aggregation in suspension*, *npj Microgravity* **11** (2025) 63.

[79] A. Gans, O. Pouliquen, and M. Nicolas, *Cohesion-controlled granular material*, *Phys. Rev. E* **101** (2020), no. 3.

[80] M. R. Maxey and J. J. Riley, *Equation of motion for a small rigid sphere in a nonuniform flow*, *Phys. Fluids* **26** (1983), no. 4 883–889.

[81] M. Maxey, *Simulation Methods for Particulate Flows and Concentrated Suspensions*, *Annu. Rev. Fluid Mech.* **49** (2017), no. 1 171–193.

[82] S. Balachandar and J. K. Eaton, *Turbulent Dispersed Multiphase Flow*, *Annu. Rev. Fluid Mech.* **42** (2010), no. 1 111–133.

[83] L. Brandt and F. Coletti, *Particle-Laden Turbulence: Progress and Perspectives*, *Annu. Rev. Fluid Mech.* **54** (2022), no. 1 159–189.

[84] Y. Yao and J. Capecelatro, *Deagglomeration of cohesive particles by turbulence*, *J. Fluid Mech.* **911** (2021) A10.

[85] M. Afkhami, A. Hassanpour, and M. Fairweather, *Effect of Reynolds number on particle interaction and agglomeration in turbulent channel flow*, *Powder Technol.* **343** (2019) 908–920.

[86] L. F. Mortimer, D. O. Njobuenwu, and M. Fairweather, *Agglomeration dynamics in liquid–solid particle-laden turbulent channel flows using an energy-based deterministic approach*, *Phys. Fluids* **32** (2020), no. 4 043301.

[87] M. U. Babler, L. Biferale, L. Brandt, U. Feudel, K. Guseva, A. S. Lanotte, C. Marchioli, F. Picano, G. Sardina, A. Soldati, and F. Toschi, *Numerical simulations of aggregate breakup in bounded and unbounded turbulent flows*, *J. Fluid Mech.* **766** (2015) 104–128.

[88] C. Marchioli and A. Soldati, *Turbulent breakage of ductile aggregates*, *Phys. Rev. E* **91** (2015), no. 5 053003.

[89] M. Breuer and N. Almohammed, *Modeling and simulation of particle agglomeration in turbulent flows using a hard-sphere model with deterministic collision detection and enhanced structure models*, *Int. J. Multiph. Flow* **73** (2015) 171–206.

[90] M. Yu, X. Yu, A. J. Mehta, A. J. Manning, F. Khan, and S. Balachandar, *Persistent reshaping of cohesive sediment towards stable flocs by turbulence*, *Sci. Rep.* **13** (2023), no. 1 1760.

[91] A. Leonelli and E. Meiburg, *Turbulent channel flow with cohesive particles*, in *Proceedings of the 14th International Symposium on Turbulence and Shear Flow Phenomena (TSFP14)*, (Heidelberg, Germany), pp. 1–10, TSFP, 2026.

[92] E. Biegert, B. Vowinckel, and E. Meiburg, *A collision model for grain-resolving simulations of flows over dense, mobile, polydisperse granular sediment beds*, *J. Comput. Phys.* **340** (2017) 105–127.

[93] E. K. Biegert, *Eroding Uncertainty: Towards Understanding Flows Interacting with Mobile Sediment Beds Using Grain-Resolving Simulations*. Phd dissertation, University of California, Santa Barbara, Mar., 2018.

[94] M. Uhlmann, *An immersed boundary method with direct forcing for the simulation of particulate flows*, *J. Comput. Phys.* **209** (2005), no. 2 448–476.

[95] N. Hori, M. E. Rosti, and S. Takagi, *An Eulerian-based immersed boundary method for particle suspensions with implicit lubrication model*, *Comput. Fluids* **236** (2022) 105278.

[96] M. M. Rai and P. Moin, *Direct simulations of turbulent flow using finite-difference schemes*, *J. Comput. Phys.* **96** (1991), no. 1 15–53.

[97] C. R. and B. H., *The slow motion of a sphere through a viscous fluid towards a plane surface—ii small gap widths, including inertial effects*, *Chem. Eng. Sci.* **22** (1967), no. 12 1753–1777.

[98] W.-P. Breugem, *A Combined Soft-Sphere Collision/Immersed Boundary Method for Resolved Simulations of Particulate Flows*, in *ASME 2010 3rd Joint US-European Fluids Engineering Summer Meeting: Volume 1, Symposia – Parts A, B, and C*, (Montreal, Quebec, Canada), pp. 2381–2392, ASMEDC, 2010.

[99] A. Khodabakhshi, S. Konidena, F. Tapia, A. Leonelli, and B. Vowinckel, *Transition between the viscous and the inertial regime in sheared dense suspensions: the effect of wall boundaries*, *Acta Mech.* (2026).

[100] F. Tapia, M. Ichihara, O. Pouliquen, and E. Guazzelli, *Viscous to Inertial Transition in Dense Granular Suspension*, *Phys. Rev. Let.* **129** (2022), no. 7 078001.

[101] R. A. Bagnold, *Experiments on a gravity-free dispersion of large solid spheres in a Newtonian fluid under shear*, *Proc. R. Soc. A* **225** (1954) 49.

[102] F. Tapia, C.-W. Hong, P. Aussillous, and E. Guazzelli, *Rheology of suspensions of non-brownian soft spheres across the jamming and viscous-to-inertial transitions*, *Phys. Rev. Lett.* **133** (2024) 088201.

[103] T. Kempe and J. Fröhlich, *An improved immersed boundary method with direct forcing for the simulation of particle laden flows*, *J. Comput. Phys.* **231** (2012), no. 9 3663–3684.

[104] P. Gondret, M. Lance, and L. Petit, *Bouncing motion of spherical particles in fluids*, *Phys. Fluids* **14** (2002), no. 2 643–652.

[105] T. Kempe and J. Fröhlich, *Collision modelling for the interface-resolved simulation of spherical particles in viscous fluids*, *J. Fluid Mech.* **709** (2012).

[106] C. Ness and E. J. Sun, *Flow regime transitions in dense non-Brownian suspensions: Rheology, microstructural characterization, and constitutive modeling*, *Phys. Rev. E* **91** (2015) 012201.

[107] J. Kim, P. Moin, and R. Moser, *Turbulence statistics in fully developed channel flow at low Reynolds number*, *J. Fluid Mech.* **177** (1987) 133–166.

[108] P. Costa, L. Brandt, and F. Picano, *Interface-resolved simulations of small inertial particles in turbulent channel flow*, *J. Fluid Mech.* **883** (Jan., 2020) A54.

[109] Z. Maches, M. Houssais, A. Sauret, and E. Meiburg, *Settling of two rigidly connected spheres*, *J. Fluid Mech.* **995** (2024) A15.

[110] J. N. Israelachvili, *Adhesion forces between surfaces in liquids and condensable vapours*, *Surf. Sci. Rep.* **14** (1992), no. 3 109–159.

[111] L. Bergström, *Hamaker constants of inorganic materials*, *Adv. Colloid Interface Sci.* **70** (1997) 125–169.

[112] J. S. Marshall and S. Li, *Adhesive Particle Flow: A Discrete-Element Approach.* Cambridge University Press, 2014.

[113] S. B. Pope, *Turbulent Flows.* Cambridge University Press, Cambridge, UK, 2000.

[114] A. Lozano-Durán and J. Jiménez, *Effect of the computational domain on direct simulations of turbulent channels up to $Re_\tau = 4200$*, *Phys. Fluids* **26** (2014), no. 1 011702.

[115] G. Wang, H. J. Park, and D. H. Richter, *Effect of computational domain size on inertial particle one-point statistics in open channel flow*, *Int. J. Multiph. Flow* **125** (2020) 103195.

[116] F. Picano, W.-P. Breugem, and L. Brandt, *Turbulent channel flow of dense suspensions of neutrally buoyant spheres*, *J. Fluid Mech.* **764** (2015) 463–487.

[117] P. Mirbod, S. Abtahi, A. Moradi Bilondi, M. E. Rosti, and L. Brandt, *Turbulent channel flow of suspensions of neutrally buoyant particles over porous media*, *J. Fluid Mech.* **954** (2023) A8.

[118] P. Costa, F. Picano, L. Brandt, and W.-P. Breugem, *Universal Scaling Laws for Dense Particle Suspensions in Turbulent Wall-Bounded Flows*, *Phys. Rev. Lett.* **117** (2016), no. 13 134501.

[119] J. L. Bentley, *Multidimensional binary search trees used for associative searching*, *Communications of the ACM* **18** (1975), no. 9 509–517.

[120] P. Virtanen, R. Gommers, T. E. Oliphant, M. Haberland, T. Reddy, D. Cournapeau, E. Burovski, P. Peterson, W. Weckesser, J. Bright, S. J. van der Walt, M. Brett, J. Wilson, K. J. Millman, N. Mayorov, A. R. J. Nelson, E. Jones, R. Kern, E. Larson, C. J. Carey, I. Polat, Y. Feng, E. W. Moore, J. VanderPlas, D. Laxalde, J. Perktold, R. Cimrman, I. Henriksen, E. A. Quintero, C. R. Harris, A. M. Archibald, A. H. Ribeiro, F. Pedregosa, P. van Mulbregt, and SciPy 1.0 Contributors, *SciPy 1.0: Fundamental algorithms for scientific computing in python*, *Nat. Methods* **17** (2020) 261–272.

[121] M. Son and T.-J. Hsu, *flocculation model of cohesive sediment using variable fractal dimension*, *Env. Fluid Mech.* **8** (2008), no. 1 55–71.

[122] M. Son and T.-J. Hsu, *The effect of variable yield strength and variable fractal dimension on flocculation of cohesive sediment*, *Water Res.* **43** (2009), no. 14 3582–3592.

[123] B. J. Lee, E. Toorman, F. J. Molz, and J. Wang, *A two-class population balance equation yielding bimodal flocculation of marine or estuarine sediments*, *Water Res.* **45** (2011), no. 5 2131–2145.

[124] K. Zhao, B. Vowinckel, T.-J. Hsu, T. Köllner, B. Bai, and E. Meiburg, *An efficient cellular flow model for cohesive particle flocculation in turbulence*, *J. Fluid Mech.* **889** (2020) R3.

[125] K. Zhao, B. Vowinckel, T.-J. Hsu, B. Bai, and E. Meiburg, *Cohesive sediment: intermediate shear produces maximum aggregate size*, *J. Fluid Mech.* **965** (2023) A5.

[126] K. Zhao, S. Zhao, H. Huang, R. Zhang, E. Meiburg, and B. Bai, *Flocculation rate of locally densely distributed cohesive particles in Taylor–Green vortex flow*, *Phys. Fluids* **36** (2024), no. 4 043326.

[127] R. S. Sharma and A. Sauret, *Experimental models for cohesive granular materials: a review*, *Soft Matter* **21** (2025), no. 12 2193–2208.

[128] C. Peng, O. M. Ayala, and L.-P. Wang, *A direct numerical investigation of two-way interactions in a particle-laden turbulent channel flow*, *J. Fluid Mech.* **875** (2019) 1096–1144.

[129] H. R. Sanness Salmon, K. Chang, C. Mucignat, and F. Coletti, *Behaviour of finite-size floating particles in free-surface turbulence*, *J. Fluid Mech.* **1019** (2025) A61.

[130] Q. Zhang and A. Prosperetti, *Physics-based analysis of the hydrodynamic stress in a fluid-particle system*, *Phys. Fluids* **22** (2010), no. 3 033306.

[131] M. Marchioro, M. Tankslay, and A. Prosperetti, *Mixture pressure and stress in disperse two-phase flow*, *Int. J. Multiphase Flow* **25** (1999) 1395–1429.

[132] A. Einstein, *Eine neue bestimmung der moleküldimensionen*, *Annalen der Physik* **324** (1906), no. 2 289–306.

[133] A. Einstein, *Berichtigung zu meiner arbeit: Eine neue bestimmung der moleküldimensionen*, *Annalen der Physik* **339** (1911), no. 3 591–592.

[134] Y. Qi, S. Shin, and F. Coletti, *Breakup and coalescence of particle aggregates at the interface of turbulent liquids*, *J. Fluid Mech.* **1021** (2025) A49.

[135] G. Voth and A. Soldati, *Anisotropic Particles in Turbulence*, *Annu. Rev. Fluid Mech.* **49** (2017), no. 1 249–276.

[136] C. Marchioli, M. Bourgoin, F. Coletti, R. Fox, J. Magnaudet, M. Reeks, O. Simonin, M. Sommerfeld, F. Toschi, L.-P. Wang, and S. Balachandar, *Particle-laden flows*, *Int. J. Multiph. Flow* **191** (2025) 105291.

[137] R. Ni, *Deformation and breakup of bubbles and drops in turbulence*, *Annu. Rev. Fluid Mech.* **56** (2024) 319–347.

[138] G. Lesser, J. A. Roelvink, J. A. T. M. van Kester, and G. S. Stelling, *Development and validation of a three-dimensional morphological model*, *Coast. Eng.* **51** (2004), no. 8 883–915.

[139] W. H. R. Chan, M. S. Dodd, P. L. Johnson, J. Urzay, and P. Moin, *Formation and dynamics of bubbles in breaking waves: Part II. The evolution of the bubble size distribution and breakup/coalescence statistics*, in *Center for Turbulence Research Annual Research Briefs*, pp. 21–34. Stanford University, 2018.